

UNIVERSITY OF KWAZULU-NATAL

Studying the Evolution of Cold Gas in Galaxies: Large Absorption Line Survey with MeerKAT

by

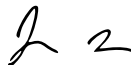
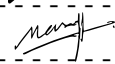
Ayanda Romanis Zungu

Submitted in fulfilment of the academic requirements for the degree of
Master of Science,
in the
School of Chemistry and Physics,
College of Agriculture, Engineering and Science
University of KwaZulu-Natal

Durban

February 2016

As the candidate's supervisor I have approved this thesis for submission.

Signed: 	Name: Jonathan Sievers	Date: 17 June 2016
Signed: 	Name: Neeraj Gupta	Date: 2016-June-15

I dedicate this dissertation to my wonderful family. Particularly to my late grandmother, who passed away while I was far away from her busy with this work, may God bless her soul. I also dedicate it to the memory of my father, who would have been happy to see me studying further to become a scientist.

Abstract

The diffuse interstellar medium (ISM) exhibits a wide range of physical conditions that are influenced by in-situ star-formation, cosmic ray energy density, photoelectric heating by dust as well as mechanical energy input from both impulsive disturbances such as supernova explosions and steady injection of energy in the form of stellar winds. This exchange of gas, metals and energy between the ISM and stars is a fundamental process through which galaxies evolve. Since star formation is intimately related to the amount and physical properties of cold atomic and molecular gas phases, understanding the properties of cold ISM in galaxies is important to reveal the process of star formation and galaxy evolution. Despite large efforts from the astronomy community over last three decades, the evolution of cold atomic and molecular gas in galaxies is still poorly constrained. The MeerKAT Absorption Line Survey (MALS) will use blind search of H I 21-cm absorption lines, which is an excellent tracer of cold atomic gas, to trace the evolution of cold gas in galaxies at $z < 2$.

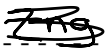
In this project, we use quasars with sight lines passing through the discs/halos of nearby galaxies to search for H I 21-cm absorption and understand the properties of cold atomic gas. In addition, we also search for hydroxyl (OH) molecular absorption lines in these environments. The study is based on sight lines selected from the Sloan Digital Sky Survey (SDSS), and are observed with the Giant Metrewave Radio Telescope (GMRT) and the Very Large Array (VLA). A lot of emphasis is put on learning and describing the fundamentals of radio interferometry, radio data analysis using the Common Astronomy Software Applications package (CASA) and physical processes in the ISM of galaxies. In addition, we also present results from a pilot project using the Southern African Large Telescope (SALT) to discover high- z quasars selected in a dust-unbiased way. This will provide ideal targets for MALS to build a comprehensive picture of the ISM and resolve several fundamental issues related to active galactic nucleus (AGNs).

Key words: quasars: absorption lines – galaxies: evolution – galaxies: ISM – galaxies: star formation

Preface and Declaration

The work described in this thesis was carried out from February 2014 to February 2016. This work was carried out at the University of KwaZulu-Natal (South Africa) and Inter-University Centre for Astronomy and Astrophysics (India). The data analysis and understanding of the results are my original work and were carried out under the guidance of Professor Jonathan Sievers (supervisor) and Professor Neeraj Gupta (co-supervisor).

This study represents my original work and has not been submitted in any form to another University. Where use was made of the work of others, it has been duly acknowledged in the text. This dissertation does not contain text, graphics or tables copied and pasted from the internet, unless specifically acknowledged and the source being detailed in the dissertation and in the reference section.

Signed:  ----- Name: ----- Ayanda Zungu ----- Date: ----- 15 June 2016 -----

Acknowledgements

I would like to thank sincerely and acknowledge gratefully the following for their generous co-operation in contributing to the success of this M.S.c thesis:

- I would like to thank God for guiding me throughout this project.
- I would also like to express my gratitude to my supervisor Professor Jonathan Sievers and my co-supervisor Professor Neeraj Gupta for believing in my ability to finish this project. They both taught me how to think like a scientist. Their guidance has been of great assistance to me.
- I am also grateful to Professor Kavilan Moodley for all the support and guidance.
- I would also like to thank Dr Matt Hilton for all the guidance he provided with the analysis and understanding of SALT observations and data analysis.
- My colleagues in the School of Chemistry and Physics for their support and assistance.
- I am also grateful to Dr Caroline Zunckel for introducing me to the field of Astrophysics.
- The University of KwaZulu-Natal for granting me the opportunity to take on and complete this study.
- I would also like to thank Ms Lindile Danisa (UKZN) and Mr Senith Samuel (IUCAA, India) for helping me with admin related issues.
- I acknowledge the funding from IUCAA during my visit to India (2014 & 2015).
- The South African Square Kilometre Array Project (SA SKA) for financial assistance through the award of SKA M.Sc. scholarship.

Thank you!

Contents

Abstract	i
Preface and declaration	ii
Acknowledgments	iii
Contents	iv
List of Figures	viii
1 Introduction	1
1.1 The Interstellar Medium	1
1.1.1 The 21-cm Line of Neutral Atomic Hydrogen (H I)	2
1.1.2 Molecular Gas	3
1.2 Radiative Transfer	4
1.2.1 Emission and Absorption of Photons	4
1.2.2 Two Level System: Einstein A and B Coefficients	6
1.2.3 Equation of Radiative Transfer	8
1.2.4 Emission and Absorption Coefficients in Terms of Einstein Coefficients	9
1.2.5 Integration of the Equation of Radiative Transfer	10
1.3 Spectral Lines: Broadening Mechanism	14
1.3.1 Spontaneous Emission and the Natural Line Width	14
1.3.2 Thermal Broadening	15
1.3.3 Collisional Broadening	16
1.3.4 The Voigt Profile	18

2	Radio Interferometry	22
2.1	Radio Interferometry Techniques	22
2.1.1	Van Cittert-Zernike Theorem	23
2.1.2	Two Element Interferometry	24
2.1.3	Aperture Synthesis	27
2.1.4	Interpretation of Aperture Synthesis	28
2.2	Editing and Calibration of the Visibility	28
2.2.1	Antenna-based Calibration	29
2.2.2	Amplitude and Phase Calibration	30
2.3	Bandwidth Smearing	31
2.4	Deconvolution	32
2.4.1	The Högbom Algorithm	32
2.5	Data Reduction and Spectral Line Analysis	33
2.5.1	Bandpass Calibration	33
2.5.2	Self-Calibration	33
2.5.3	Continuum Subtraction	35
2.5.4	Velocity Reference Frames and CVEL	35
3	GMRT Search for H I 21-cm Absorption Towards SDSS J1443+0214	37
3.1	Description of GMRT Observations	38
3.2	Data Analysis	39
3.3	Results	51
4	GMRT and VLA Search hydroxyl (OH) Absorption	55
4.1	GMRT Search for OH Absorption Towards SDSS J1443+0214	56
4.1.1	Description of GMRT Observations	56
4.1.2	Data Analysis	57
4.1.3	Results	67
4.2	VLA Search for OH Absorption Towards SDSS J0849+5108	68
4.2.1	Description of VLA Observations	68
4.2.2	Data Analysis	70
4.2.3	Results	76
4.3	Conclusion	77
5	Building a Dust-unbiased Sample of Radio Loud Quasars	79
5.1	Target Selection for the Pilot Project with SALT	81
5.2	Description of SALT Observations	82

5.3	Spectroscopic Data Reduction	85
5.4	Quasar Redshift Measurements	86
6	Future Prospects	92
	Bibliography	92

List of Tables

3.1	Results of self-calibration.	50
3.2	Two component Gaussian fits to the 21-cm absorption profile.	53
4.1	Results of self-calibration.	66
4.2	OH column density limits (3σ) for the H I 21-cm absorption components presented in the previous chapter. The rms ($\sigma_{rms} = 0.7$) used here was obtained from the spectrum of H I 21-cm absorption smoothed to ~ 15 km/s (corresponding to the average FWHM of two H I 21-cm absorption components). This was done using the task <code>specsmooth</code>	68
4.3	Frequency set-up used for VLA observations. The last column has fluxes determined by <code>setjy</code> for J0542+4951.	72
4.4	Results of self-calibration for IF 11.	75
4.5	Results of self-calibration for IF 14.	76
4.6	OH column density limits (3σ) for the H I 21-cm absorption components presented in Gupta et al. (2013). The rms used here for IF 11 and IF 14 (smoothed to 10 km/s) is $\sigma_{rms} = 1.2$ mJy/beam/channel and $\sigma_{rms} = 1.4$ mJy/beam/channel, respectively (Fig. 4.21).	77
5.1	Spectroscopic observations summary for Galaxies-possible quasar discussed in this work. The SALT RSS-pg0900 grating with pc03850 order-blocking filter was used for all observations. Slitlets in all masks were $8'$ long and $2''$ wide.	85
5.2	Spectroscopic redshifts of quasars measured using SALT RSS. Q is the redshift quality flag.	87

List of Figures

1.1	Schematic of H I 21-cm ground state hyperfine splitting, showing the electron and proton spins. This radiation is produced whenever an electron reverses its spin, changing its energy very slightly in the process Ianjamasimanana (2014).	3
1.2	Three basic processes in which light interacts with the atoms: (a) absorption, (b) stimulated emission, and (c) spontaneous emission Griffiths (1995).	5
1.3	The three radiative processes connecting two levels, 2 and 1.	6
1.4	Radiative transfer geometry showing the path-length and the optical depth.	9
1.5	Comparison between Gauss and Lorentz line profiles. The Gaussian dominates the line core while the Lorentzian drops off much slowly. The two curves have the same equivalent width, the same area, and the same width.	18
1.6	Normalized intensity vs velocity for Lyman- α profile, $b = 10$ km/s, with a range of $N_{\text{H I}}$ values: 10^{11} , 10^{14} , 10^{17} , cm^{-2} (where $N_{\text{H I}} = 10^{11} \text{ cm}^{-2}$ correspond to a smaller curve).	20
2.1	Diagrammatic representation of a two-element interferometer Taylor et al. (1999).	25
3.1	The Sloan Digital Sky Survey (SDSS) Data Release 12 image of the quasar J144304.53+021419.3.	38
3.2	The figure shows all the 30 antennas of the GMRT with 14 of them clustered in the Central square and the rest along the Eastern, Southern and Western arms.	39
3.3	The <code>listobs</code> output showing the scan summary, source coordinates and frequency set-up for the observations. The target SDSS J1443+0214 is referred to as Field ID 2.	40
3.4	Amplitude and Phase vs uv-distance for 3C286.	41
3.5	Amplitude and Phase vs uv-distance for 3C286, after initial inspection and flagging of the data.	42
3.6	Amplitude and Phase vs uv-distance for 3C286, after flagging and calibration.	43
3.7	RFI inspection for 3C286 calibrated visibilities. (a) Unflagged RFI appear as a bright horizontal line, (b) Flagged data is marked in blue.	44

3.8	Bandpass solution for nine GMRT antennas. The different colours represent different polarizations.	45
3.9	Amplitude and Phase vs uv-distance for phase calibrator, after flagging and calibration.	46
3.10	Single channel maps, of (a) 3C286 and (b) J1445+099. The contour levels start at 3σ	47
3.11	(a) Single channel map of SDSS J1443+0214. (b) Channel averaged map of SDSS J1443+0214. The contour levels start at 3σ	48
3.12	Continuum image of SDSS J1443+0214 after phase-only (panels a, b and c) and amplitude calibration (panel d). The contour levels start at 3σ	49
3.13	The GMRT spectrum showing H I 21-cm absorption detected towards SDSS J1443+0214 . The zero velocity axis corresponds to the 1035.63 MHz. The fitted parameters are given in Table. 3.2. The red lines are the Gaussian fits to the absorption spectrum. Residuals are plotted in dashed line and they are arbitrarily shifted for clarity.	53
4.1	The 18-cm ground state transitions of the OH molecule. These transitions are due to hyperfine interactions with the nuclear spin, and each doublet state is further split into 2 levels, corresponding to $F = J + I$, where I is the nuclear spin, equal to $\pm 1/2$. Transitions between these 4 independent energy states result in the 18-cm ground state spectral line at $\sim 1612, 1665, 1667$, and 1720 MHz.	56
4.2	The <code>listobs</code> output showing the scan summary, source coordinates and frequency set-up for OH observations. The target SDSS J1443+0214 is referred to as Field ID 2.	57
4.3	Amplitude and Phase vs uv-distance for 3C286.	58
4.4	Amplitude and Phase vs uv-distance for 3C286, after initial inspection and flagging of the data.	59
4.5	Amplitude and Phase vs uv-distance for 3C286, after flagging and calibration.	60
4.6	RFI inspection for 3C286 calibrated visibilities. (a) Unflagged RFI appear as a black horizontal stripe, (b) Flagged data is marked in blue.	60
4.7	Bandpass solution for seven GMRT antennas. The different colours represent different polarizations. Antenna C06 and C09 were affected by RFI and were removed.	61
4.8	Amplitude and Phase vs uv-distance for phase calibrator, after flagging and calibration.	62
4.9	RFI inspection for J1445+099 calibrated visibilities. (a) In baseline C00 - E04 and (c) C08 - E04 , the unflagged RFI appear as darker stripes. In (b) and (d) flagged data are marked in blue.	63
4.10	RFI inspection for SDSS J1443+0214 calibrated visibilities. Here we only show one baseline C08 - E04.	64
4.11	CLEAN maps of (a) 3C286 and (b) J1445+099. The contour levels start at 3σ	65
4.12	(a) Channel averaged map of SDSS J1443+0214. Continuum image of SDSS J1443+0214 after phase-only (panels b and c) and amplitude calibration (panel d). The contour levels start at 3σ	66

4.13	GMRT spectrum towards SDSS J1443+0214 showing OH non-detection. The vertical lines at frequency 1214.2922 MHz and 1215.7193 MHz represents the expected locations of OH main lines corresponding to $z_{abs} = 0.3715$ for the H I 21-cm absorption towards SDSS J1443+0214.	68
4.14	Figure showing all the 27 VLA antennas. Photo reference: http://images.nrao.edu/images/VLASouth_med.jpg	69
4.15	The Sloan Digital Sky Survey (SDSS) Data Release 12 image of the quasar J084957.97+510829.0. The galaxy responsible for H I 21-cm, Ca II and Na I absorption at $z_g = 0.3120$ is represented by ‘G1’.	70
4.16	The <code>listobs</code> output showing the scan summary, source coordinates and frequency set-up for the observations. The target SDSS J0849+5108 is referred to as Field ID 3. Note that this is not the complete <code>listobs</code> output. For frequency set-up see Table 4.3.	71
4.17	Amplitude and Phase vs uv-distance for J0542+4951 (IF 11), after flagging and calibration.	72
4.18	Bandpass solution for eight VLA antennas. The different colours represent different polarizations. These Bandpass solutions are for spectral window 11. Antenna 9 was affected by RFI and removed.	73
4.19	(a) Channel averaged map of SDSS J0849+5108 for IF 11. Continuum image of SDSS J0849+5108 after phase-only (panels b and c) and amplitude calibration (panel d). The contour levels start at 3σ .	74
4.20	(a) Channel averaged map of SDSS J0849+5108 for IF 14. Continuum image of SDSS J0849+5108 after phase-only (panels b and c) and amplitude calibration (panel d). The contour levels start at 3σ .	75
4.21	GMRT spectra towards SDSS J0849+5108 showing OH non-detection for two main lines, (a) and (b). The vertical dashed lines at (a) 1269.3612 MHz and (b) 1270.8530 MHz, represent the expected locations of OH main lines corresponding to $z_g = 0.3120$ from the H I 21-cm absorption towards SDSS J0849+5108.	76
5.1	WISE colour-colour plot for radio sources ($\delta < +20^\circ$, >200 mJy) with WISE counterparts (Cyan). Radio galaxies and quasars are shown as black and coloured circles respectively.	82
5.2	Visibility annulus of objects observable with SALT as a function of declination and hour angle, and the hashed area shows the range of motion for the tracker at two different declinations. Photo reference: http://www.sal.wisc.edu/PFIS/docs/rss-vis/ebb/pfis/observer/intro.html#SALT	83
5.3	The 2D spectrum taken with SALT. The horizontal axis is the dispersion direction with wavelength getting redder towards the right. The coloured bar at the bottom is the intensity scale of the image. The three CCD chips comprising the RSS detector can also be seen, with gaps between them. The red vertical line show the bending of the sky lines.	84

5.4	(a) The $z_{em} = 1.138$ quasar J040015-142328, showing C II and Mg II emission lines. (b) The $z_{em} = 2.390$ quasar J095231-245351, showing Si II, Si IV, C IV and C III emission lines. . . .	87
5.5	(a) The $z_{em} = 2.969$ quasar J101313-254654, showing Lyman- α , O I and C IV broad emission lines. (b) The $z_{em} = 2.132$ quasar J111820-305458, showing Si IV, C IV and C III emission lines.	88
5.6	(a) The $z_{em} = 2.698$ quasar J115222-270126, showing Lyman- α , N V, Si II, O IV, C IV and C III emission lines. (b) The $z_{em} = 0.896$ quasar J115450-281251, showing Mg II and O II emission lines.	88
5.7	(a) The $z_{em} = 1.045$ quasar J124553-161645, showing Mg II emission line. (b) The $z_{em} = 1.939$ quasar J125215-310351, showing C IV, C II and C III emission lines.	89
5.8	(a) The $z_{em} = 1.267$ quasar J131736-134532, showing a broad C III and Mg II emission lines. (b) The $z_{em} = 2.553$ quasar J141327-342235, showing Lyman- α , O I, Si IV and C IV emission lines.	89
5.9	(a) The $z_{em} = 2.111$ quasar J143708-294718, showing Si IV, C IV and C III emission lines. (b) The $z_{em} = 2.777$ quasar J125443-383357, showing Lyman- α , C II, Si IV, C IV and C III emission lines.	90
5.10	(a) On the left panel, the target object is undetectable due to bright nearby star. The sky emission and the reference star have completely overwhelm the spectrum of the object of interest. (b) On the right panel, we show an example of long-slit 2D spectra of a faint QSO. Here, we notice that there is a faint horizontal white line corresponding to the target source (see text for details).	90

This chapter presents the main theoretical aspects relevant to the thesis, regarding the interstellar medium, radiative processes and spectral line broadening. This discussion draws heavily from basic textbooks such as Draine (2010); Pradhan & Nahar (2011); Rybicki & Lightman (2008) and Shu (1991).

Information of astrophysical objects is obtained through observations of electromagnetic radiation. Gas and dust interact with radiation in several ways. To be able to interpret the observations correctly, it is important to understand these processes.

1.1 The Interstellar Medium

The material between the stars that is composed of gas, dust and charged particles (protons, nuclei and electrons) called cosmic rays, distributed throughout our galaxy and others is called the interstellar medium (ISM) (Draine, 2010). Approximately 99% of the mass of the ISM is in the form of gas, and the remaining 1% is (sub)micron size silicate and carbonaceous dust grains. The ISM is warmed up by incoming radiation, cosmic rays, and collisions between dust and gas particles, and is cooled down when the gas and dust emit radiation.

The evolution of a galaxy depends critically on the structure of the ISM and the interactions taking place in it. The structure of the ISM is shaped by the life cycle of stars, from a star formation which extracts gas from the ISM, to supernova explosions which returns gas back into it. This cyclic process, does not only enhance this medium with heavy elements but also releases great amounts of energy to shape it. Thus, the study of the cold atomic and molecular gas plays a major role in understanding the formation and subsequent evolution of galaxies.

The gas exists in four phases in the ISM; (i) the hot ionized medium, which is found in hot, low density cavities of the supernova remnants, (ii) the warm ionized medium, which consist of partially ionized gas, (iii)

the warm neutral medium, which consist of warm neutral gas, and (iv) the cold neutral medium which is found in cold cloud cores (Draine, 2010).

Molecular clouds contain internal structures, elongated filaments and dense condensations of matter. In these dense and cold regions, star formation takes place. However, in the simplest reasonable model, the cloud of gas will collapse when the inward pressure is greater then the outward pressure. The physical conditions for collapse can be approximated by the Virial Theorem, a theorem which states that a gravitational system is stable as long as $2K + U = 0$, where K and U are the system kinetic and potential energy. If at some point the magnitude of internal kinetic energy is less than half the magnitude of the potential energy, i.e. $2K + U < 0$, then the system will be unstable and collapse to form first a protostar and eventually an actual star where fusion reactions form heavier elements. Cooling is a crucial ingredient for star formation. Depending on temperature and density, a variety of cooling processes can affect the gas. For densities (n) below the critical density, cooling rate per cm^3 is proportional to n^2 .

Massive stars form most of the heavy elements and, at the end of their relatively short lifespan, they explode as supernovae spreading new elements to the ISM. The main interacting forces in the star formation process are gravitation, turbulence, magnetic pressure, rotation, and gas pressure.

1.1.1 The 21-cm Line of Neutral Atomic Hydrogen (H I)

The neutral atomic gas is traced through the H I 21-cm line, and is found in warm neutral medium (WNM) and cold neutral medium (CNM) (Draine, 2010). The proton and electron have an intrinsic angular momentum spin $s = \pm 1/2$ and therefore, have a magnetic dipole moment. Due to the presence of magnetic fields created by the motion of these charged particles, the electron and the proton can only spin in a direction parallel or anti-parallel to their magnetic dipole moments (see Fig. 1.1).

The total angular momentum spin has two possible values, $F = 0$ or $F = 1$ and therefore has two eigenstates. These two states are known as triplet and singlet. However, this comes from the Pauli's exclusion principle, "which requires a total wave function of two electrons (including spin) to be antisymmetric under the exchange, $1 \rightleftharpoons 2$ " (Draine, 2010). For example, an antisymmetric spatial wave function requires a symmetric spin function, which means that the total spin, $S = 1$, with three possible projections $S_z = 1$, $S_z = 0$, and $S_z = -1$. For obvious reasons, "the $S_z = 1$ configuration is called the triplet state, while $S_z = 0$ is called the singlet state" (Draine, 2010). In the triplet state, the electron and proton magnetic moments are pointing in the same direction (parallel) and corresponds to a higher energy level.

The singlet state, corresponds to a lower energy level, and the magnetic moments of the two particles are anti-parallel. When an atomic hydrogen is excited into the triplet state (e.g. due to collisions), it will eventually go back to its lowest possible energy level (the singlet state).

Between the two states, the energy difference is $\Delta E = 5.9 \times 10^{-6}$ eV, which corresponds to a frequency $\nu = 1420.4$ MHz ($\lambda = 21$ cm). So the transition from $F = 1$ to $F = 0$ state will result in an emission of a photon

at $\lambda = 21$ cm. This so-called spin-flip or hyperfine transition is a magnetic dipole transition (forbidden line) and has an extremely long lifetime. The hydrogen atom can stay in the triplet state for ~ 11 million years. Although the transition is rare, hydrogen atoms are very abundant in the Universe, which makes the H I 21-cm line easily detectable. A schematic representation of the hyperfine transition of H I 21-cm is shown below.

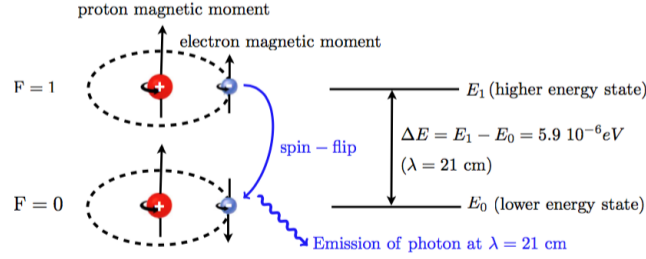


Figure 1.1: Schematic of H I 21-cm ground state hyperfine splitting, showing the electron and proton spins. This radiation is produced whenever an electron reverses its spin, changing its energy very slightly in the process Ianjamasimanana (2014).

Neutral atomic hydrogen H I 21-cm line can be observed through emission or absorption. The H I 21-cm line has successfully been used as a mapping tool for the distribution and kinematics of the atomic hydrogen. It has also been used to infer the matter distribution in galaxies. H I 21-cm has been mapped through surveys of a pre-selected galaxy sample (targeted survey) or by means of observations of a large volume of space in the sky (blind survey).

The limited sensitivity of current radio telescopes makes it difficult to detect H I 21-cm emission in individual objects past $z = 0.1$. According to Gupta et al. (2010), “the detectability of H I 21-cm absorption is independent of redshift, since it depends only on the strength of the background radio sources and H I 21-cm absorption cross-section of the galaxies”.

Hence, H I 21-cm absorption allows us to study neutral gas systems at high redshift, where the systems are thought to be precursors to present day galaxies (Curran & Webb, 2006). However, very few H I 21-cm absorption systems are known to date, leaving many gaps in understanding the role these absorption systems may play in the galactic evolution.

1.1.2 Molecular Gas

The connection between the phases of the ISM and star formation has been the subject of a number of investigations. However, star formation is found to be more closely linked to the molecular phase of the ISM. The molecular gas represents the densest component of the ISM and is localized in discrete giant molecular clouds, which tend to be irregularly shaped with a density distribution far from homogeneous. Molecular clouds contain embedded cores in which new stars form.

Molecular clouds are formed primarily from hydrogen arranged molecules, which consist of two atoms,

e.g. H_2 . In the visible portion of the electromagnetic spectrum H_2 does not interact with light i.e. H_2 is invisible to optical telescopes. However, when studying the molecular clouds, there are several kinds of tracers that can be used, such as dust or molecules, which live deep within the molecular clouds, e.g. OH and CO.

Hydroxyl radical (OH) is an example of a molecule with the ground electronic state having non zero electronic orbital angular momentum, with seven electrons. A brief description of OH is discussed in the later chapters. However, CO molecule forms by a series of gas phase chemical reactions that are important when most hydrogen is in molecular form. Direct formation from atoms, $\text{C} + \text{O} \rightarrow \text{CO}$, is possible but unlikely due to the small cross-sections of the atoms (Osterbrock & Ferland, 2006).

OH and CO are the most abundant molecules that can be searched using radio telescopes since these are tracers of the molecular interstellar matter. Unlike molecular hydrogen, in the mm-region of the spectrum, CO is particularly active since it absorbs and emits electromagnetic radiation efficiently. According to Draine (2010), most molecules “exist only deep inside dense clouds of hydrogen, protected by the outer layers of gas and dust”, because they can be quickly broken apart when exposed to ultraviolet radiation in space. Also, dust blocks the starlight coming to the cores, thus reducing the external heating. Both the diffuse H I clouds and the molecular clouds are quite cold, with temperature below 100 K i.e. associated with star formation.

The primary focus of this research project is to study the properties of cold gas in the ISM of nearby galaxies, through H I 21-cm and OH 18-cm absorption lines.

1.2 Radiative Transfer

Electromagnetic radiation provides most of the information we have on the astrophysical Universe. Electromagnetic waves emitted by cosmic sources travel through vast distances before being detected by our instruments. The space they cross is not empty, but it is filled with mixture of ions, atoms, molecules and large dust grains.

The propagation of electromagnetic radiation through a medium is affected by absorption, emission and scattering processes. In this section, we describe these processes in detail. However, we are going to exclude scattering process. For this work, we follow Rybicki & Lightman (2008), the radiative transfer chapter, which describes these interactions mathematically. According to Rybicki & Lightman (2008), “if a ray passes through matter, energy may be added or subtracted from it by emission or absorption, and can be used to understand the properties of the intervening medium as well as the source from where the radiation originated”.

1.2.1 Emission and Absorption of Photons

If a 2-state system is in the ground state, denoted by X_1 , it can transition into its excited state X_2 by absorbing a photon with energy $E_2 - E_1$. Absorption is described by,

$$X_1 + h\nu \rightarrow X_2. \quad (1.1)$$

Bohr's frequency condition described in eqn. (1.2), gives the frequency at which the spectral line occurs, where h denotes Planck's constant,

$$h\nu = E_2 - E_1. \quad (1.2)$$

Let us suppose that we have number density n_1 of absorbers X in level 1. The rate per unit volume at which the absorbers absorb photons will be proportional to both the density of photons of the appropriate energy and number density n_1 , so we can represent the rate of change of n_1 due to photo-absorption by level 1 (Draine, 2010),

$$\left(\frac{dn_2}{dt}\right)_{1 \rightarrow 2} = -\left(\frac{dn_1}{dt}\right)_{1 \rightarrow 2} = n_1 B_{12} u_\nu, \quad \nu = \frac{E_2 - E_1}{h}, \quad (1.3)$$

where u_ν is the radiation energy density per unit frequency, and the proportionality constant B_{12} is the Einstein B coefficient for the transition $1 \rightarrow 2$. A neutral atom in the gaseous state can absorb radiation and transfer an electron to an excited state. However, an absorber X in an excited level 2 can decay to a lower level with emission of a photon. Below we illustrate the two ways this can happen (see Fig. 1.2):

$$\text{Spontaneous emission:} \quad X_2 \rightarrow X_1 + h\nu, \quad (1.4)$$

$$\text{Stimulated emission:} \quad X_2 + h\nu \rightarrow X_1 + 2h\nu. \quad (1.5)$$

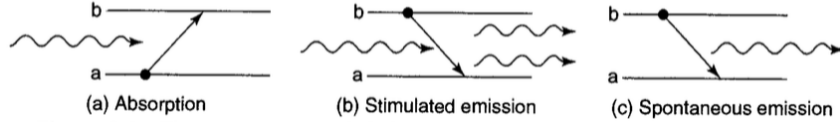


Figure 1.2: Three basic processes in which light interacts with the atoms: (a) absorption, (b) stimulated emission, and (c) spontaneous emission Griffiths (1995).

Spontaneous emission is a random process. It is independent of the presence of radiation field, with a probability per unit time, A_{21} , Einstein A coefficient. As described in eqn. (1.4), “an emission line is formed when an atom or molecule makes a transition from a quantized energy level E_2 of an atom, to a lower energy level E_1 , emitting a photon of a particular energy and wavelength” (Draine, 2010). According to Draine (2010), “a spectrum of such photons will show up as an emission spike at the frequency associated with these photons”. However, absorption occurs when an atom or molecule absorbs a photon and then make a transition from a lower discrete energy state, E_1 , to a higher discrete energy state, E_2 , i.e. as described in eqn. (1.1).

Generally, these absorbed photons come from the background continuum radiation (e.g. a typical radio loud quasar or a radio galaxy) and a spectrum will show a drop in the continuum radiation at the frequency associated with the absorbed photons. In the case of neutral atomic hydrogen, absorption occurs when a frequency matching condition, $\nu = 1420.4$ MHz or $\lambda = 21$ cm is satisfied. If we receive light with precisely this wavelength λ missing, we assume, that somewhere on the sight-line to the source there must be H I. These

transitions are transparent to dust, allowing for detection of any absorption system towards even the dustiest line of sight.

1.2.2 Two Level System: Einstein A and B Coefficients

In 1917, Einstein provided a simple interpretation of the Planck spectrum for blackbody¹ radiation based on matter radiation interactions. In particular he showed that the analytic form of the Planck function implies the existence of spontaneous emission (which was not known at the time), beyond stimulated emission and absorption. He also derived two equations linking the rates of these three phenomena so that if one knows one of them, it is easy to derive the remaining two. The arguments developed are as follows.

Let us consider transitions involving two atomic levels such that the energies are $E_2 > E_1$. For this case, the transition is given by a discrete quantum of energy shown in eqn. (1.2). In accordance with the old quantum theory, which entails Planck's definition of light quanta (Pradhan & Nahar, 2011). "Einstein postulated three distinct radiative processes that connect the two levels" shown in Fig. 1.3 (Pradhan & Nahar, 2011).

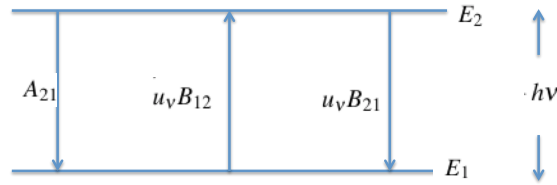


Figure 1.3: The three radiative processes connecting two levels, 2 and 1.

The interaction between the atoms and the photons are described by the intrinsic probability coefficients (photon emission rate, s^{-1}) as follow: (i) Atoms with energy, E_1 can absorb a photon in a radiation field of density u_v and make a transition to the excited state with energy E_2 with a probability coefficient B_{12} , (ii) Atoms in an excited state with energy E_2 can make a transition to the lower energy state via stimulated emission of a photon, with probability coefficient B_{21} , resulting in a transition from level 2 to level 1 induced by some other photon, and (iii) However, atoms in an excited state with energy E_2 can also fall back into the lower energy state via spontaneous emission, with probability coefficient A_{21} .

Stimulated emission occurs if photons of identical frequency, polarization and direction of propagation are already present, and the rate of stimulated emission is proportional to the density of these photons. Thus the total rate of depopulation of level 2 due to emission of photons can be described by,

$$\left(\frac{dn_1}{dt} \right)_{2 \rightarrow 1} = - \left(\frac{dn_2}{dt} \right)_{2 \rightarrow 1} = n_2 (A_{21} + u_v B_{21}), \quad (1.6)$$

where the coefficient B_{21} is the Einstein B coefficient for the transition from $2 \rightarrow 1$ as shown in Fig. 1.3. Thus now we have three coefficients postulated by Einstein characterizing radiative transitions between levels, 2 and 1: A_{21} , B_{21} and B_{12} .

¹A blackbody is an ideal construction referring to an object that absorbs all the electromagnetic radiation impinging onto it.

We will now show that these coefficients are not independent of one another. According to Rybicki & Lightman (2008), “the radiation field becomes the blackbody radiation field in Local Thermodynamic Equilibrium (LTE)”.

The correct analytical form of the blackbody spectrum has been derived by Planck in 1900 and is known as the Planck function. His model required that the energy of radiation in the cavity had to be quantised in small packets each of energy $h\nu$. “Einstein built upon this idea and proposed the quantisation of electromagnetic radiation itself in 1905 to explain Photoelectric effect” (Rybicki & Lightman, 2008). In LTE the intensity is given everywhere by the blackbody spectrum,

$$B_\nu(T) = \frac{2h\nu^3}{c^2} \frac{1}{e^{\frac{h\nu}{k_B T}} - 1}, \quad (1.7)$$

with specific energy density (k_B is define as Boltzmann constant),

$$(u_\nu)_{LTE} = \frac{4\pi}{c} B_\nu(T) = \frac{8\pi h\nu^3}{c^3} \frac{1}{e^{\frac{h\nu}{k_B T}} - 1}, \quad (1.8)$$

this distribution have units of energy per volume per spectral unit (Pradhan & Nahar, 2011). If we place absorber X into a blackbody radiation field, then the rate of change of level 2 is,

$$\begin{aligned} \frac{dn_2}{dt} &= \left(\frac{dn_2}{dt} \right)_{1 \rightarrow 2} + \left(\frac{dn_2}{dt} \right)_{2 \rightarrow 1} \\ &= n_1 B_{12} (u_\nu)_{LTE} - n_2 (A_{21} + B_{21} (u_\nu)_{LTE}) \\ &= n_1 B_{12} \frac{8\pi h\nu^3}{c^3} \frac{1}{e^{\frac{h\nu}{k_B T}} - 1} - n_2 \left(A_{21} + B_{21} \frac{8\pi h\nu^3}{c^3} \frac{1}{e^{\frac{h\nu}{k_B T}} - 1} \right). \end{aligned} \quad (1.9)$$

If the absorbers are allowed to come to equilibrium with the radiation field, we have the ratio of n_2 to n_1 fixed by the Boltzmann equation,

$$\frac{n_2}{n_1} = \frac{g_2}{g_1} e^{\frac{E_1 - E_2}{k_B T}}, \quad (1.10)$$

where the g 's are the statistical weights of the lower and upper levels, for H I 21-cm, $g_1 = 1$ and $g_2 = 3$ and $E_1 - E_2 = 5.9 \times 10^{-6}$ eV is the energy splitting, see Fig. 1.1. In thermal equilibrium $dn_2/dt = 0$, therefore, eqn. (1.9) becomes,

$$n_1 B_{12} (u_\nu)_{LTE} = n_2 A_{21} + n_2 B_{21} (u_\nu)_{LTE}. \quad (1.11)$$

Now solving for u_ν from eqn. (1.11),

$$(u_\nu)_{LTE} = \frac{A_{21}/B_{21}}{(n_1/n_2)(B_{12}/B_{21}) - 1}. \quad (1.12)$$

The condition for LTE to be satisfied, eqn. (1.8) must hold. For the expression in eqn. (1.12) to be equal to eqn. (1.8) “for all temperatures, T , we must have the following Einstein relations” (Rybicki & Lightman, 2008),

$$B_{21} = \frac{c^3}{8\pi h\nu^3} A_{21}, \quad (1.13)$$

and,

$$g_1 B_{12} = g_2 B_{21}, \quad (1.14)$$

or,

$$B_{12} = \frac{g_2}{g_1} B_{21} = \frac{g_2}{g_1} \frac{c^3}{8\pi h \nu^3} A_{21}. \quad (1.15)$$

Hence, the stimulated emission B_{21} and absorption B_{12} terms are both determined by A_{21} and the ratio g_2/g_1 i.e. we only require one of these A_{21} , B_{12} , B_{21} to get the other two.

Equation (1.13) and (1.14) connects any microscopic process and its inverse process (i.e. they are generally known as detailed balance relations), here absorption and emission (Rybicki & Lightman, 2008). “Einstein was led to include the process of stimulated emission by the fact that without it he would not get Planck’s law, but only Wien’s law, which was known to be incorrect” (Rybicki & Lightman, 2008).

According to Rybicki & Lightman (2008), “one will obtain Wien’s law when stimulated emission is neglected, because Wien’s law is the expression of the Planck spectrum when $h\nu \gg k_B T$. But when $h\nu \gg k_B T$, level 2 is very sparsely populated relative to level 1, $n_2 \ll n_1$ ”.

1.2.3 Equation of Radiative Transfer

Let us consider a beam of radiation with intensity I_ν entering a slab of material. Let s measure the path-length along the direction of propagation. In order to define the equation of radiative transfer we neglect scattering and assume that the only processes affecting the intensity are absorption and emission (Rybicki & Lightman, 2008). As radiation propagates through the medium, the intensity evolves according to the equation of radiative transfer,

$$dI_\nu = -\alpha_\nu I_\nu ds + j_\nu ds. \quad (1.16)$$

Eqn. (1.16) gives the radiative transfer equation in differential form. The term “ $-\alpha_\nu I_\nu$ is the net change in I_ν due to absorption and stimulated emission (both process are linear in I_ν) and $j_\nu ds$ is the change in I_ν due to spontaneous emission by the material in the path of the beam” (Rybicki & Lightman, 2008). The absorption coefficient α_ν at frequency ν , with dimensions of 1/length is normally positive. Emission coefficient j_ν at frequency ν , “has dimensions of power per unit volume per unit frequency per unit solid angle” (Rybicki & Lightman, 2008).

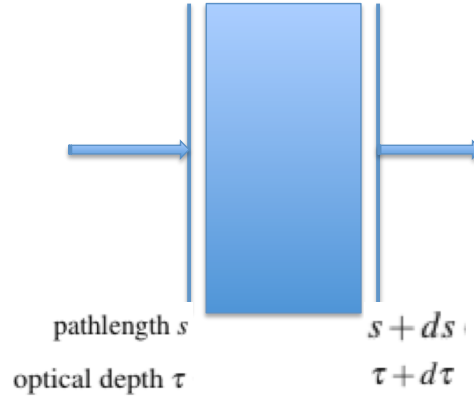


Figure 1.4: Radiative transfer geometry showing the path-length and the optical depth.

1.2.4 Emission and Absorption Coefficients in Terms of Einstein Coefficients

Absorption and emission can be due to atoms, ions or molecules etc. Atoms, ions or molecules with discrete energy levels contribute to the absorption and emission coefficient. In this section, we want to write the absorption and emission coefficient in terms of Einstein coefficients.

Let us start with the emission coefficient j_ν . Each atom which undergoes the transitions $2 \rightarrow 1$, emits the energy $h\nu$ in a random direction. Therefore, “the amount of energy emitted per unit volume, per unit solid angle, per unit time, per unit frequency is” (Rybicki & Lightman, 2008),

$$j_\nu = \frac{h\nu}{4\pi} n_2 A_{21} \phi_\nu, \quad (1.17)$$

where A_{21} is the transition probability coefficient per unit time and we have that $\phi_\nu d\nu$ is the probability that the emitted photon will have frequency in $(\nu, \nu + d\nu)$. Similarly, the probability per unit time for absorption is,

$$\alpha'_\nu = \frac{h\nu}{4\pi} \phi_\nu n_1 B_{12}. \quad (1.18)$$

Eqn. (1.18) gives the absorption coefficient uncorrected for stimulated emission, and α'_ν is strictly a positive coefficient. The absorption coefficient α_ν is proportional to the net absorption i.e. true absorption minus stimulated emission (negative absorption), is described by,

$$\alpha_\nu = \frac{h\nu}{4\pi} \phi_\nu (n_1 B_{12} - n_2 B_{21}), \quad (1.19)$$

or re-writing eqn. (1.19) using the Einstein relation,

$$\begin{aligned} \alpha_\nu &= \frac{h\nu}{4\pi} \phi_\nu n_1 B_{12} \left(1 - \frac{g_1 n_2}{g_2 n_1} \right) \\ &= \frac{h\nu}{4\pi} \phi_\nu n_1 B_{12} \left(1 - e^{-\frac{h\nu}{k_B T_*}} \right), \end{aligned} \quad (1.20)$$

where T_* , is the excitation temperature of level 2 relative to level 1 is defined by,

$$\frac{n_2}{n_1} = \frac{g_2}{g_1} e^{-\frac{E_{21}}{k_B T_*}}, \quad (1.21)$$

where n_2, n_1 are the populations of the upper and lower levels. The radiative transfer equation can be expressed in terms of Einstein coefficients as follows,

$$\begin{aligned} \frac{dI_\nu}{ds} &= -\alpha I_\nu + j_\nu \\ &= -\frac{h\nu}{4\pi} (n_1 B_{12} - n_2 B_{21}) I_\nu \phi_\nu + \frac{h\nu}{4\pi} n_2 A_{21} \phi_\nu. \end{aligned} \quad (1.22)$$

1.2.5 Integration of the Equation of Radiative Transfer

We can now change the independent variables from path-length s to optical depth τ_ν defined by,

$$d\tau_\nu = \alpha_\nu ds. \quad (1.23)$$

The optical depth is a measure of the decreased photon intensity relative to the assumed continuum, where τ_ν can be expressed as,

$$\tau_\nu(s) = \int_{s_0}^s \alpha_\nu(s') ds'. \quad (1.24)$$

According to Rybicki & Lightman (2008), “a medium is optically thick or opaque when, τ_ν , integrated along typical path through the medium satisfies $\tau_\nu \gg 1$ ”. However, when $\tau_\nu \ll 1$, the medium is said to be optically thin or transparent. In the optically thin medium, any emitted photon is very likely to escape the cloud of gas without being absorbed by another atom, the optical depth of the cloud is small, $\tau_\nu \ll 1$. In an optically thick medium the “average photon of frequency ν cannot traverse the entire medium without being absorbed” (Rybicki & Lightman, 2008). For $h\nu \ll k_B T_*$ eqn. (1.20) reduces to,

$$\alpha_\nu \approx \frac{h\nu}{4\pi} \phi_\nu n_1 B_{12} \left(\frac{h\nu}{k_B T_*} \right). \quad (1.25)$$

If T_* is independent of the path-length s , then τ_ν can be expressed as follows,

$$\tau_\nu = \frac{(h\nu)^2}{4\pi} \phi_\nu B_{12} \frac{1}{k_B} \int \frac{n_1}{T_*} ds'. \quad (1.26)$$

We now define the number of atoms per unit area i.e. the density integrated along the line of sight through the absorbing material is called the column density,

$$N = \int n ds, \quad (1.27)$$

in units (atoms/cm²). The density of atoms which are in the proper state to absorb the photon of interest. Eqn. (1.26) can be expressed as,

$$\tau_\nu = \frac{(h\nu)^2}{4\pi} \phi_\nu B_{12} \frac{N_l}{k_B}. \quad (1.28)$$

Now we express the radiative transfer equation as,

$$dI_\nu = -I_\nu d\tau_\nu + S_\nu d\tau_\nu, \quad (1.29)$$

or,

$$\begin{aligned} \frac{dI_\nu}{d\tau_\nu} &= -I_\nu + \frac{j_\nu}{\alpha_\nu} \\ &= -I_\nu + S_\nu, \end{aligned} \quad (1.30)$$

where S_ν is referred to as source function defined as the “ratio of the emission and the absorption coefficients” (Rybicki & Lightman, 2008),

$$S_\nu = \frac{j_\nu}{\alpha_\nu}, \quad (1.31)$$

or, in terms of Einstein coefficients,

$$\begin{aligned} S_\nu &= \frac{n_2 A_{21}}{n_1 B_{12} - n_2 B_{21}} \\ &= \frac{8\pi h \nu^3}{c^3} \left(\frac{n_1 g_2}{n_2 g_1} - 1 \right)^{-1}. \end{aligned} \quad (1.32)$$

It is important to remember that eqn. (1.29) does not include scattering process, such as scattering by dust grains or by electrons. Radiation in thermal equilibrium with a blackbody enclosure of temperature T have special properties. Thermodynamics can be used to show that the specific intensity of radiation in a blackbody cavity is a universal function of temperature and frequency, $I_\nu = B_\nu(T)$.

Based on similar reasoning(s), one can also show that for any material in thermal equilibrium, $S_\nu = B_\nu(T)$ (Kirchoff’s Law). Within a region that is in thermal equilibrium, the specific intensity of radiation field is given everywhere by the Planck function, $j_\nu = \alpha_\nu B_\nu$, since $S_\nu = B_\nu$. This is not the same as saying $I_\nu = B_\nu$, which is only true for very thick medium, $\tau_\nu \rightarrow \infty$. According to Rybicki & Lightman (2008), “thermal radiation becomes a blackbody radiation for optically thick medium, $\tau_\nu \gg 1$ ”. The equation of radiative transfer for thermal radiation is,

$$\frac{dI_\nu}{d\tau_\nu} = -I_\nu + B_\nu, \quad (1.33)$$

since $S_\nu = B_\nu$ through a blackbody enclosure. In radio frequency regions $h\nu \ll k_B T$ (Reyleigh-Jeans limit), therefore the Planck function becomes,

$$I_\nu = B_\nu(T) \approx \frac{2\nu^2}{c^2} k_B T, \quad (1.34)$$

which is proportional to T . It is conventional in radio astronomy to measure intensity in terms of brightness temperature defined by,

$$T_b = \frac{c^2}{2\nu^2 k_B} I_\nu. \quad (1.35)$$

The source function can be defined by,

$$S_v = \frac{2\nu^2 k_B}{c^2} T_s, \quad (1.36)$$

where T_s is the spin temperature. According to Field (1958), “the spin temperature is defined through a ratio between the number densities n_i of hydrogen atoms in the two hyperfine levels (which we labelled with a subscript 1 and 2 for singlet and triplet levels, respectively) of the electronic ground state”. It is defined via $(n_2/n_1) = (g_2/g_1)e^{-(E_{21}/k_B T_s)}$, where $(g_2/g_1) = 3$ is the ratio of the spin degeneracy factors and the excitation temperature is $T_* \equiv E_{21}/k_B = 0.068$ K (very low), is the temperature corresponding to the difference between the levels.

H I 21-cm is primarily collisionally excited in cold neutral medium (CNM) but in warm neutral medium (WNM) Lyman- α radiation plays a role (Field, 1958). We also note that $T_s \approx T_*$ for spin flip transitions or forbidden transition, which have a very low spontaneous emission rate, $A_{21} = 2.896 \times 10^{-15}$ (very small). H I 21-cm is a forbidden transition, and this often happens in the ISM where the density is very low. This transition is different from permitted transition, transitions which occur relatively quickly i.e. having high rate of spontaneous emission.

We can now formally integrate eqn. (1.29) by moving $I_v d\tau_v$ to the left hand side and multiplying by the integrating factor e^{τ_v} ,

$$\begin{aligned} dI_v + I_v d\tau_v &= S_v d\tau_v \\ e^{\tau_v} (dI_v + I_v d\tau_v) &= e^{\tau_v} S_v d\tau_v \\ d(e^{\tau_v} I_v) &= e^{\tau_v} S_v d\tau_v. \end{aligned} \quad (1.37)$$

We now integrate this from some initial point, which we define to be $\tau_v = 0$, with initial value $I_v(0)$;

$$e^{\tau_v} I_v(\tau_v) - I_v(0) = \int_0^{\tau_v} e^{\tau'_v} S_v(\tau'_v) d\tau'. \quad (1.38)$$

Now multiplying by $e^{-\tau_v}$ to obtain the equation of radiative transfer in integral form,

$$I_v(\tau_v) = I_v(0)e^{-\tau_v} + \int_0^{\tau_v} e^{-(\tau_v - \tau'_v)} S_v(\tau'_v) d\tau'. \quad (1.39)$$

Since S_v is proportional to T_s , let suppose S_v is independent of τ'_v , if we have a cloud with uniform temperature, we can remove the source function from the integral to obtain,

$$\begin{aligned} I_v(\tau_v) &= I_v(0)e^{-\tau_v} + \int_0^{\tau_v} e^{-(\tau_v - \tau'_v)} S_v(\tau'_v) d\tau' \\ &= I_v(0)e^{-\tau_v} + S_v [1 - e^{-\tau}]. \end{aligned} \quad (1.40)$$

If we have an optically thick cloud, $\tau_v \gg 1$, $I_v \rightarrow S_v$ i.e. the radiation field loses memory of its initial intensity and becomes more and more determined by the properties of the surrounding medium, note that if $I_v > S_v$ then $dI_v/d\tau_v < 0$ and I_v decreases along the ray (net absorption). On the other hand, if $I_v < S_v$ then $dI_v/d\tau_v > 0$ and I_v increases along the ray (net emission).

Therefore, “the source function is the quantity that the specific intensity relaxes to”, if given a sufficient optical depth (Rybicki & Lightman, 2008). If we have an optically thin cloud, $\tau_\nu \ll 1$, $I_\nu \rightarrow \tau_\nu S_\nu + (1 - \tau_\nu)I_\nu(0)$. An astrophysical important case is to suppose there is some source of continuous radiation (e.g. Quasar), with brightness temperature T_{bg} behind the cloud with temperature T_s , where $T_{bg} \gg T_s$. This radiation will be absorbed in passing through the cloud. In this general case the total brightness temperature T_b the observer sees is,

$$T_b = T_s [1 - e^{-\tau_\nu}] + e^{-\tau_\nu} T_{bg}. \quad (1.41)$$

For optically thin cloud eqn. (1.41) is defined by,

$$T_b = \tau_\nu T_s + [1 - \tau_\nu] T_{bg}. \quad (1.42)$$

However, for optically thick cloud, $\tau_\nu \gg 1$, eqn. (1.41) becomes,

$$T_b = T_s. \quad (1.43)$$

If the medium is optically thick at all frequencies, it becomes a blackbody. The optical depth is a product of the absorption cross-section and column density of the absorber. If we integrate over the line of sight L , we obtain,

$$\tau_\lambda = \int_0^L \alpha(\lambda) ds = \int_0^L n_{abs} \sigma(\lambda) ds = \sigma(\lambda) \int_0^L n_{abs} ds = N \sigma(\lambda). \quad (1.44)$$

In eqn. (1.44), $\sigma(\lambda)$ represents the absorption cross-section and has units of $\text{cm}^2/\text{absorber}$. Eqn. (1.44) assumes that everything is constant with optical depth. The observed intensity can be described by,

$$I_\lambda = I_{\lambda,0} e^{-N \sigma(\lambda)}, \quad (1.45)$$

so if $\sigma(\lambda)$ is known and $I_\lambda/I_{\lambda,0}$ measured, the column density can be determined by,

$$\tau_\lambda = -\ln \left(\frac{I_\lambda}{I_{\lambda,0}} \right) = N \sigma(\lambda), \quad (1.46)$$

solving for N ,

$$N = \frac{1}{\sigma(\lambda)} \ln \left(\frac{I_{\lambda,0}}{I_\lambda} \right). \quad (1.47)$$

In practice this is not how N is solved because lots of physics that requires modelling or fitting goes into $\sigma(\lambda)$. The actual line shape is determined by the distribution of material as a function of velocity and the temperature distribution along the line of sight. The radiative transfer gives the overall profile. This calculation of N depends sensitively on getting all the physics governing $\sigma(\lambda)$ as correct as possible. The final total cross-section, $\sigma(\lambda)$, for the transition is then the convolution of broadening mechanism which are briefly discussed in the next section.

1.3 Spectral Lines: Broadening Mechanism

All spectral lines have a finite width and a particular line profile. According to Shu (1991), “the shape of the line is directly dependent on the atomic transitions”. However, there are several mechanisms accountable for the broadening of the line. To begin with, due to the uncertainty principle, there is the fundamental or natural breadth of a line. “The line width must reflect this uncertainty by way of broadening, as well as other radiative and collisional effects” (Pradhan & Nahar, 2011).

When a system makes a transition between two discrete energy levels E_2 and E_1 emitting a single photon, the frequency of the photon should be equal to $\omega = (E_2 - E_1)/\hbar$. The nature of the width of the spectral line contains important information about the state of the physical system, so it is very important to understand the mechanisms that cause broadening. The finite width of the spectral line can arise because of several reasons among which three particular processes are of important in astrophysics, “namely; thermal broadening, natural broadening and collisional broadening” (Pradhan & Nahar, 2011).

1.3.1 Spontaneous Emission and the Natural Line Width

Natural broadening is the spectral width exhibited by the molecule in the absence of interactions with other atoms. This is a result of the Heisenberg uncertainty principle, which states that energy and time cannot be simultaneously measured precisely. According to Griffiths (1995), “the Heisenberg uncertainty principle, $\Delta E \Delta t \geq \hbar$, as time available for an energy measurement decreases, the inherent uncertainty of the result increases, because an electron in an excited state occupies its orbital for only a brief instant, Δt ” i.e. limited lifetime in each state causes an uncertainty in energy of state.

Absorption of photons does not take place at one exact unique frequency/wavelength but over a (small) range. From Fourier transform point of view, the radiative decays with limited lifetime form a wave packet emitted at random time. This stretch in time domain essentially forms natural line broadening in wavelength domain through Fourier transform.

All real line would have a broadening by at least an amount given by the following considerations. As an atom tries to absorb a resonant line photon, it simultaneously tries to decay back spontaneously to the lower state i . “Following through the Fourier transform analysis of the decaying probability amplitude, we obtain an expression for the intensity spread in the quantum mechanical case in frequency space” (Pradhan & Nahar, 2011),

$$L(\omega) = \frac{\Gamma/2\pi}{(\omega_{fi} - \omega)^2 + (\Gamma/2)^2}. \quad (1.48)$$

Eqn. (1.48) is a Lorentzian line shape and it is fully characterized by the central frequency ω_{fi} and the full width at half maximum (Γ). This line-shape will be observed whenever the density of final states is nearly constant over the width of the line. Note that if the final level is not the ground state of the system it will decay as well further broadening the line-width. A better generalization, which takes into accounts the fact that the

upper states may be “fuzzy” because of spontaneous decays gives,

$$\mathbb{L}(\nu) = \frac{1}{\pi} \left[\frac{\Gamma_{if}/4\pi}{(\nu - \nu_{if})^2 + (\Gamma_{if}/4\pi)^2} \right], \quad (1.49)$$

with Γ_{if} , the total width of the line given by,

$$\Gamma_{if} = \sum_{n < f} A_{fn} + \sum_{n < i} A_{in}. \quad (1.50)$$

In eqn. (1.50), A_{fn} and A_{in} are the spontaneous decay rates for transition $f \rightarrow n$ and $i \rightarrow n$. The absorption coefficient for a given line is given by (Pradhan & Nahar, 2011),

$$\begin{aligned} a_\nu &= \left(\frac{\pi e^2}{m_e c} \right) f_{12} \phi(\nu) \\ &= \left(\frac{\pi e^2}{m_e c} \right) f_{12} \left[\frac{\Gamma_{21}/4\pi^2}{(\nu - \nu_{21})^2 + (\Gamma_{21}/4\pi)^2} \right]. \end{aligned} \quad (1.51)$$

Below we are going to estimate the natural atomic hydrogen line width. Let suppose a photon emitted by an atom at rest, the Heisenberg uncertainty principle $\Delta E \Delta t \geq \hbar$ can also be written as $2\pi \Delta \nu \Delta t \geq 1$. Since $\Delta t \sim$ occupation time in the excited state, we have that $\Delta t \sim 1/A_{21}$, therefore we have that for H I, $A_{21} \sim 3 \times 10^{-15} \text{ s}^{-1}$. From this, the natural line width is given by,

$$\Delta \nu = \frac{A_{21}}{2\pi} \sim 5 \times 10^{-16} \text{ Hz},$$

however, in velocity units, at $\nu_0 = 1420.4 \text{ MHz}$, this gives,

$$\Delta \nu = \Delta \nu \frac{c}{\nu_0} \sim 10^{-19} \text{ km/s}.$$

This is very small for any observed $\Delta \nu$ (natural line width) i.e. the Universe is 13 billion years old, so something moving at 10^{-19} km/s would only have moved about 40 m since the big bang. From these calculations, we notice that the natural width is unlikely to be important. Thus natural broadening is usually negligible compared to other broadening effects. In the next two sections we are going to investigate other sources of broadening.

1.3.2 Thermal Broadening

The atoms that make up the gas of the stellar atmosphere are continuously in motion. “The individual atoms will have random motions away from or towards the observer, leading to red or blue-wards frequency shifts” (Pradhan & Nahar, 2011). According to Pradhan & Nahar (2011), “these motion may only be described by the thermal motion of the gas, or it may include the larger-scale motions of turbulence or rotation”. However, the shifting of the rest wavelength by varying the amount for different populations of atoms will usually result in the observed lines being broadened by an amount significantly greater than the natural line width.

The “total absorption coefficient a_ν in a line at a given frequency ν , absorbed by an atom in its rest frame at the Doppler-shifted frequency $\nu(1 - \nu/c)$ is obtained by integrating the absorption coefficient of an atom $a_\nu[\nu(1 - \nu/c)]$ over all velocities” (Pradhan & Nahar, 2011),

$$a_\nu = \int_{-\infty}^{+\infty} a_\nu[\nu(1 - \nu/c)] f_{Max}(\nu) d\nu. \quad (1.52)$$

The Doppler shift depends on the relative movements of the object (e.g. velocity of that atom), which in turn depends on the ambient temperature. In the LTE, a Maxwellian function f_{Max} shown in eqn. (1.52) is a good approximation for velocity distribution of particles. The probability of atoms with a line of sight velocity ν and $(\nu + d\nu)$ is given by,

$$f_{Max}(\nu) d\nu = \left(\frac{1}{v_0 \pi^{1/2}} \right) \exp \left(-\frac{\nu^2}{v_0^2} \right) d\nu. \quad (1.53)$$

Kinetic theory (i.e. classical limit) relates the root mean square velocity to temperature by, $\frac{1}{2} m_a \langle \nu^2 \rangle = \frac{3}{2} k_B T$, and therefore we have that,

$$\langle \nu^2 \rangle = \int_{-\infty}^{+\infty} \nu^2 f_{Max}(\nu) d\nu = \frac{v_0^2}{2}, \quad (1.54)$$

where,

$$v_0 = \sqrt{\frac{2k_B T}{m_a}} = \sqrt{2} \sigma_\nu = b, \quad (1.55)$$

where b is the broadening parameter and m_a is the atomic mass. The symmetric Doppler width about the central frequency ν_{21} , note now we use ν_{21} , instead of ν . The thermal (Doppler) width is defined as,

$$\Delta \nu_D \equiv \frac{\nu_{21}}{c} v_0 = \frac{\nu_{21}}{c} b. \quad (1.56)$$

The line profile due to the thermal motion of atoms is described by the normalised Gaussian, given by,

$$a_\nu = \frac{1}{\sqrt{\pi} b} \exp \left(-\frac{\nu^2}{b^2} \right), \quad (1.57)$$

Assuming that there is no bulk flow, $\bar{\nu} = 0$. In the previous section we have shown that the natural broadening is so tiny for H I 21-cm that way we will neglect it completely from henceforth. However, like before we are going to estimate the thermal width for H I 21-cm atoms with kinetic temperature $T = 100$ K, $\nu_{21} = 1420.4$ MHz, and we get that,

$$\Delta \nu_D = \frac{\nu_{21}}{c} b \sim 6106.4 \text{ Hz},$$

or in velocity units,

$$\Delta \nu = \Delta \nu_D \frac{c}{\nu_{21}} \sim 1.3 \text{ km/s}.$$

This type of broadening is significant at very high temperatures or at low pressures.

1.3.3 Collisional Broadening

To this point, we have briefly describe the broadening mechanism(s) arising from intrinsic properties of the atom and collective effects of the motion of atoms. Collisional broadening happens in high density environments where the time between the collisions is less than the time between the start and end of an emission due

to a transition between energy levels. The collision interrupts the emission event. This introduces a broadening of the line around the line centre in a Lorentzian profile, with the same form as with natural broadening.

The magnitude of this effect depends on the frequency ν_{col} at which such collisions occur. This frequency can be estimated following Pradhan & Nahar (2011) as,

$$\nu_{col} = \nu_0 n \sigma, \quad (1.58)$$

where $\nu_0 = \sqrt{3k_B T / m_a}$ is the thermal speed of the atoms or ions, n is the density and σ is the cross-section for collisions. Collisional broadening takes into account the fact that the gas is not just filled with one atomic species that is doing the emitting and absorbing. As mentioned above, since we are looking at cool regions, therefore a higher total pressure in the system (especially from free electrons that zip around with high speeds) produces a higher rate of collisions between the emitting atoms and their neighbours.

In order for collisional broadening to dominate over thermal broadening, a very dense gas is needed. This is related to pressure, which is why “collisional broadening is sometimes called Pressure broadening” (Pradhan & Nahar, 2011). This can enhance the effective value of Γ_{if} by several orders of magnitude above the natural broadening level. However, there is a difference between collisional and pressure broadening. In pressure broadening, random fluctuating electric fields broaden the energy levels, even if the particles undergo no actual collisions.

Below we are going to estimate the collisional broadening width. The uncertainty in energy because of collision(s) ΔE can be estimated from the uncertainty principle, to be $\Delta E \Delta t \approx \hbar$, which gives us the collisional broadening width,

$$\Delta \nu_{col} \approx \frac{1}{2\pi t_{col}}. \quad (1.59)$$

According to Pradhan & Nahar (2011), “the mean free path for collisions, l is defined by, $nl\pi d^2 = 1$, where d is the effective diameter for a collision close enough to affect the radiation process”. The mean velocity as previously used, is given by $\bar{v} = \sqrt{3k_B T / m_a}$, apply to all occurrences. The mean time between successive collisions is,

$$t_{col} = \frac{l}{\bar{v}} = \frac{1}{n\pi d^2} \sqrt{m_a / 3k_B T}, \quad (1.60)$$

using the above equations we get the width to be,

$$\Gamma_{col} = \Delta \nu_{col} = \frac{1}{2\pi t_{col}} = \frac{1}{2} n d^2 \sqrt{3k_B T / m_a}. \quad (1.61)$$

Let suppose we have H I gas of density $n = 10 \text{ cm}^{-3}$, the diameter of the atom, $d = 2a_0 = 10^{-10} \text{ m}$, where, a_0 , is the Bohr radius and the temperature, $T = 100 \text{ K}$. We estimate the width of collisional broadening to be,

$$\Gamma_{col} = \frac{1}{2} n d^2 \sqrt{3k_B T / m_a} \sim 8 \times 10^{-11} \text{ Hz}, \quad (1.62)$$

this is also very small to be observable. In the next section, we are going to define the function that takes into account the convolution of broadening mechanisms discussed.

1.3.4 The Voigt Profile

This section deals with some of the physics that allows us to draw physical conclusions about the absorber from the shape of the absorption lines. While the depth of absorption line provides information about the number of the exact ion encountered in the cloud and hence about the chemical composition of the cloud, the width and more general shape of the line feature tells us the size of the entire system as well as providing hints about its internal structure.

The line shape of spectroscopic transitions depend on the broadening mechanism of the initial and final states and include natural broadening, collisional broadening and Doppler broadening, as discussed. Natural and collisional broadening are homogeneous mechanisms and produce Lorentzian line shape.

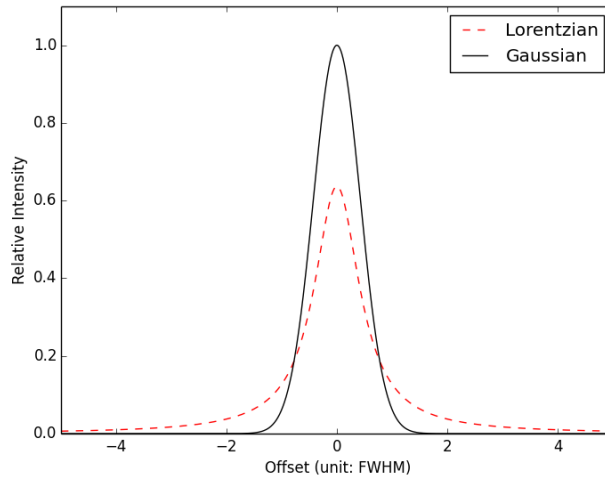


Figure 1.5: Comparison between Gauss and Lorentz line profiles. The Gaussian dominates the line core while the Lorentzian drops off much slowly. The two curves have the same equivalent width, the same area, and the same width.

However, the combination of Lorentzian and Gaussian (Fig. 1.5) line shapes can be approximated by a Voigt function, a function for which there is no closed form expression. The Voigt profile is a convolution of these two line shapes. We need a net profile, the combination of these mechanisms, because we want to extract the physical properties of the gas, such as its velocity distribution, temperature and density. Quite often one has to take simultaneously into account both line profiles i.e. Gaussian and Lorentzian. Now let suppose we have two functions, $f(v)$ and $g(v)$, the convolution of these two functions is given by the relation,

$$f(v) \star g(v) = \int_{-\infty}^{+\infty} f(v-t)g(t)dt. \quad (1.63)$$

If we take the convolution of eqn. (1.51) and (1.57), we obtain the net line profile which is given by,

$$a_v = \left(\frac{\pi e^2}{m_e c} \right) \frac{f_{12}}{\sqrt{2\pi}} \int_{-\infty}^{+\infty} \frac{(\Gamma_{21}/4\pi^2) \exp\left(-\frac{v^2}{2\sigma_v^2}\right)}{\sigma_v \left(v - v_{21} - v_{21} \frac{v}{c}\right)^2 + (\Gamma_{21}/4\pi)^2} dv. \quad (1.64)$$

Using the transformation equations,

$$y^2 = \frac{m}{2kT}v^2, \quad \sqrt{2}\sigma_v dy = dv, \quad (1.65)$$

$$a = \frac{\Gamma_{21}}{4\pi\Delta\nu_D}. \quad (1.66)$$

We defined the dimensionless frequency to be,

$$u = \frac{v - v_{21}}{v_{21}} \frac{c}{\sqrt{\frac{2kT}{m}}} = \frac{v - v_{21}}{\Delta\nu_D}. \quad (1.67)$$

Using these transformation equation, eqn. (1.64) can be expressed as,

$$\begin{aligned} a_v &= \left(\frac{\pi e^2}{m_e c} \right) f_{12} \phi_v \\ &= \left(\frac{\pi e^2}{m_e c} \right) f_{12} \frac{a}{\sqrt{\pi}\Delta\nu_D} \int_{-\infty}^{+\infty} \frac{e^{-y^2}}{(u-y)^2 + a^2} dy. \end{aligned} \quad (1.68)$$

The Voigt function is described as,

$$\phi_v = \frac{1}{\sqrt{\pi}\Delta\nu_D} H(a, u), \quad (1.69)$$

where the convolution is conveniently expressed by the Hjerting function $H(a, u)$,

$$H(a, u) = \frac{a}{\pi} \int_{-\infty}^{+\infty} \frac{e^{-y^2}}{(u-y)^2 + a^2} dy. \quad (1.70)$$

The optical depth for an absorption line is related to the column density of the gas N by,

$$\tau_\lambda = \frac{\pi e^2}{m_e c^2} f_{ij} \lambda_{ij}^2 N \phi_\lambda, \quad (1.71)$$

where λ_{ij} is the wavelength of the transition, f_{ij} is the oscillator strength and ϕ_λ is the line profile. Note that u acts as an independent variable, it is the difference between the wavelength along the profile and the line centre in units of the Doppler width.

Also, we note that a is not a function of $\Delta\nu$ and therefore does not vary with location across the absorption profile. For the given transition, a is a function of only the damping constant, the wavelength of the line centre, and the thermal width. The thermal width also appears in the normalization of the Voigt function. The width Γ of the natural line profile is much narrow than the thermal width and the net line profile is then indistinguishable from a Gaussian.

Taking the line profile into velocity space we obtain,

$$\phi_v(v) = \frac{1}{\sigma_v \sqrt{2\pi}} H(a, u), \quad (1.72)$$

$$\text{where } u = \frac{v}{\sigma_v \sqrt{2}}, \quad (1.73)$$

$$\text{and } a = \frac{\Gamma_{21} c}{4\pi v_{21} \sigma_v \sqrt{2\pi}}. \quad (1.74)$$

Finally, we evaluate the optical depth, eqn. (1.71), by replacing ϕ_λ , and inserting $f_{ij} = 0.45$, $\Gamma_{21} = 6.26 \times 10^8 \text{ s}^{-1}$ and $\lambda_{ij} = 1215.67 \text{ \AA}$ (For Lyman- α), we have:

$$\begin{aligned}\tau(\nu) &= \frac{\pi e^2}{m_e c} f_{ij} \lambda_{ij} N \phi_V(\nu) \\ &= 2.65 \times 10^{-15} f_{ij} \lambda_{ij} N \phi_V(\nu) \\ &= 1.45 \times 10^{-12} N_{\text{H I}} \phi_V(\nu),\end{aligned}\tag{1.75}$$

with λ in \AA and $\phi(\nu)$ in s/km . The plots of the intensity functions for each column density value is shown below,

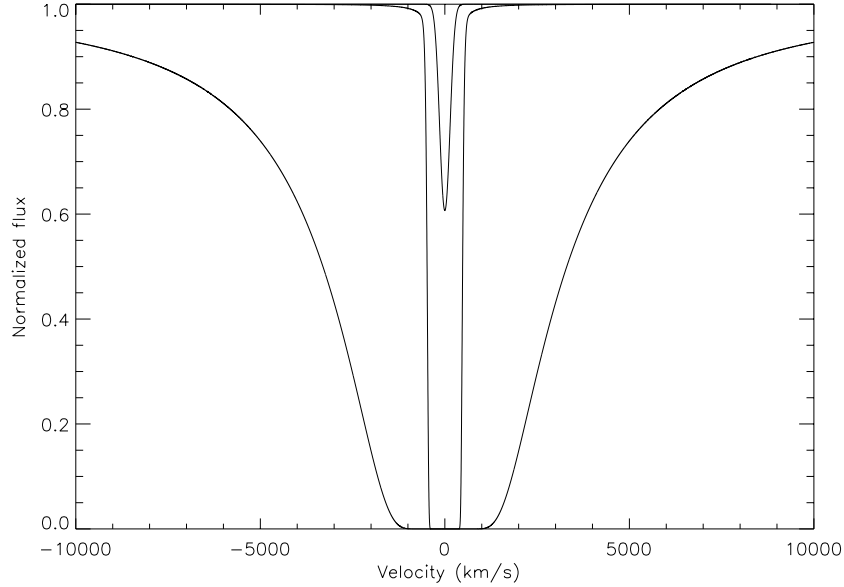


Figure 1.6: Normalized intensity vs velocity for Lyman- α profile, $b = 10 \text{ km/s}$, with a range of $N_{\text{H I}}$ values: 10^{11} , 10^{14} , 10^{17} cm^{-2} (where $N_{\text{H I}} = 10^{11} \text{ cm}^{-2}$ correspond to a smaller curve).

The differences are quite large. For low column density, we only see the effect of thermal broadening, i.e. the Lorentzian is absent. At large column density, however, the broadening is entirely due to collisional broadening (the width significantly exceeds the thermal motions).

Thermal motions are not the only way in which a velocity dispersion can arise. Bulk movements of material can also broaden spectral lines. For a line to be broadened, the emitting atoms must be moving at different speeds along the line of sight. This could occur where a gas cloud is rotating, where gas is flowing inwards or outwards from a centre, or where gas is in turbulent or chaotic motion (Jones et al., 2004). Therefore a galaxy rotating about its centre will produce a spectrum in which the lines are broadened. In fact, typical thermal velocities are $\sim \text{km/s}$, while bulk flows are $\sim 100 \text{ km/s}$.

One can distinguish thermal broadening in a spectrum from broadening due to bulk motions by noting that, thermal broadening depends on the mass of the individual emitting atom (heavy atoms move more slowly) so the lines from different elements will have different values of $\Delta\lambda/\lambda$. Broadening from bulk motion will affect

all spectral lines equally, they will have the same value of $\Delta\lambda/\lambda$, and it doesn't have to be Gaussian. However, Voigt profiles are useful approximations for the intensity distribution in spectral lines.

Radio Interferometry

2.1 Radio Interferometry Techniques

In this chapter we summarize the essentials of radio interferometry. The history of radio interferometry takes us back to the mid 1940s, when the first radio interferometric observations were performed on the Sun. For example, McCready et al. (1947) used a single antenna located on a high coastal cliff in Australia to point east as the Sun rose. A fringe pattern was recorded from the interference between the direct radiation from the Sun and that reflecting from the ocean surface below. This “sea interferometry” finds its analog at visible wavelengths in a Lloyd’s mirror.

The Lloyd’s Mirror “experiment uses wavefront division at a mirror to produce two source interference patterns”. According to Allman et al. (1993), “an interference pattern is produced between the light (i.e. light from a monochromatic slit) coming directly from a point source and indirectly from its reflection in a plane mirror” i.e. reflection at a mirror produces a phase shift. As a result, the pattern is almost similar to that produced in Young’s double slit experiment, except for a fringe displacement due to the phase shift. One obtains uniformly spaced fringes in the small angle approximation.

The paper of McCready et al. (1947) is the first to note the Fourier transform relationship between the quantity measured by an interferometer and the radio brightness distribution, a relationship which forms the basis of all modern Fourier Synthesis telescopes based on aperture synthesis.

Aperture synthesis is a type of interferometry where a number of antennas, arranged in a particular pattern, or array receives radiation from an astronomical object at the same time and the signals are combined pairwise in the correlator. The technique of signal combination in most modern interferometers is a cross-correlation (a method used to find where two signals match), but the signals can also be added. The response of each pair of antennas contains amplitude and phase, which generally are represented as a complex number. Below we

are going to explain why astronomers use radio interferometry, and then in the coming sections we will give a brief discussion on the fundamental equations used in derivation of the final map or image from the radio interferometric observations and the advantages of increasing the number of antennas.

Avison & George (2012) writes that, the maximum resolution for a conventional telescope can be approximately given by,

$$\theta = 1.22 \frac{\lambda}{D}. \quad (2.1)$$

Equation. (2.1), gives the angular resolution, θ , in radians, the wavelength, λ , and the diameter of the mirror or parabolic dish, D . “The factor 1.22 is estimated from a calculation of the position of the first dark circular ring surrounding the central Airy disk of the diffraction pattern”, a full discussion is given by Argyle & Argyle (2012). Generally, the mirrors required to produce angular resolutions of milliarcseconds (for optical wavelengths e.g. $\lambda \sim \mu\text{m}$) need to be only a few tens of meters in diameter. If we study the Universe using mm/radio wavelengths, $\lambda \sim 10^2 - 10^3 \mu\text{m}$, the telescopes would need parabolic dishes of $\sim 10^4 - 10^7 \text{ m}$.

Hence, this would be very difficult to build. Currently the largest steerable single dishes have diameters of $\sim 100 \text{ m}$. The field of radio astronomy aims to achieve resolutions comparable with optical telescopes, so they use a technique of interferometry, where the signals received by two or more antennas are combined together to approximate having a single large dish. For an interferometer, the maximum resolution is given by,

$$\theta \sim \frac{\lambda}{b_{\max}}, \quad (2.2)$$

where b_{\max} is the maximum separation (baseline) between two antennas of the interferometer. In the following sections, we will introduce the fundamental relationship between the spatial coherence function and the sky brightness. This forms the basis of synthesis imaging. We are going to show how interferometry exploits this relationship in practice. We will also discuss basics of image formation and reconstruction, calibration, self-calibration and spectral line analysis. These techniques will be used in later chapters to reduce data from the Giant Metrewave Radio Telescope (GMRT) and Very Large Array (VLA).

2.1.1 Van Cittert-Zernike Theorem

The goal of radio astronomy is to receive, process and interpret cosmic signals. Let us suppose we have an astronomical object located at a point “ \mathbf{r} ” and time “ t ”. This object causes electromagnetic waves, described by a vector field, $\mathbf{E}(\mathbf{r}, t)$, to propagate through space where it can be detected at \mathbf{R} by an astronomer. While the electric field varies rapidly and randomly, the time average of its variance as a function of frequency is well defined. For this case, we treat the electric field as scalar i.e. we ignore the polarization properties of $\mathbf{E}(\mathbf{r}, t)$. We define a signal as a response of a probe to the radiation field (Taylor et al., 1999). The signal $v(\mathbf{r}, t)$, is proportional to $\mathbf{E}(\mathbf{r}, t)$ and ignoring the constant of proportionality, the intensity of radiation $I(\mathbf{r})$ can be measured as,

$$I(\mathbf{r}) = \langle v(\mathbf{r}, t) v^*(\mathbf{r}, t) \rangle. \quad (2.3)$$

In the above equation, eqn. (2.3), the asterisk represent the complex conjugate. The coherence theory describes the phenomenon of interference as a statistical description of electromagnetic radiation (Taylor et al., 1999). Coherence is a term which refers to the degree of correlation between two measurements of the radiation field. The mutual coherence function is defined by,

$$\Gamma(\mathbf{r}_1, \mathbf{r}_2, \tau) = \langle v(\mathbf{r}_1, t) v^*(\mathbf{r}_2, t - \tau) \rangle, \quad (2.4)$$

which is nothing more than the correlation function between random signals measured at two points \mathbf{r}_1 and \mathbf{r}_2 at times differing by τ . The degree of coherence is given by,

$$\gamma(\mathbf{r}_1, \mathbf{r}_2, \tau) = \frac{\Gamma(\mathbf{r}_1, \mathbf{r}_2, \tau)}{\sqrt{\langle I(\mathbf{r}_1) I(\mathbf{r}_2) \rangle}}. \quad (2.5)$$

The radiation is said to be coherent if $|\gamma| = 1$, or incoherent if $|\gamma| = 0$, and it is defined to be partially coherent if $|\gamma|$ lies somewhere in between.

If the points \mathbf{r}_1 and \mathbf{r}_2 coincide, $\Gamma(\mathbf{r}, \mathbf{r}, \tau)$ is called the auto-correlation function. The auto-correlation function is the Fourier transform of the power spectrum of the radiation field, this theorem is known as Wiener-Khinchin Theorem (Taylor et al., 1999). If the mutual coherence function is measured with $\tau = 0$, then $\Gamma(\mathbf{r}_1, \mathbf{r}_2, 0)$ is called the spatial coherence function. The spatial coherence of two points illuminated by a quasi-monochromatic source of incoherent radiation is given by the Van Citter-Zernike Theorem. This theorem forms the basis of Fourier Synthesis imaging.

There are two assumptions required, (1) we assume that the source is far enough away that the incoming radiation is described by a plane wave (Taylor et al., 1999). (2) The emission from the source must be spatially incoherent at the source (Taylor et al., 1999).

From the Van Cittert-Zernike Theorem, the spatial coherence function is related to the sky brightness as follows,

$$\Gamma(\mathbf{r}_1, \mathbf{r}_2, 0) = \int I(\mathbf{s}) e^{-2\pi i \mathbf{s} \cdot (\mathbf{r}_1 - \mathbf{r}_2)/c} d\Omega. \quad (2.6)$$

Here \mathbf{s} is a unit vector directed towards the source, $I(\mathbf{s})$ is the intensity and $d\Omega$ is an element of the solid angle. The measurement of the spatial coherence function depends only on the relative difference between \mathbf{r}_1 and \mathbf{r}_2 .

2.1.2 Two Element Interferometry

The basic measuring device in synthesis mapping is the interferometer. A two element interferometer has two identical antennas separated by a distance \mathbf{b} . Let us suppose the two antennas are directed towards a point source of some flux density, in a direction indicated by the unit vector \mathbf{s} . Since the source is in the far field of the interferometer, the incoming wave front can be considered to be a plane wave.

The plane wave incident on the interferometer arrives at the right antenna first then at the left antenna (see Fig. 2.1). The time delay between two identical antennas with separation \mathbf{b} , is given by, $\tau_g = \mathbf{b} \cdot \mathbf{s}/c$ and is called the geometrical delay. Below we show the schematic diagram for the two element interferometer.

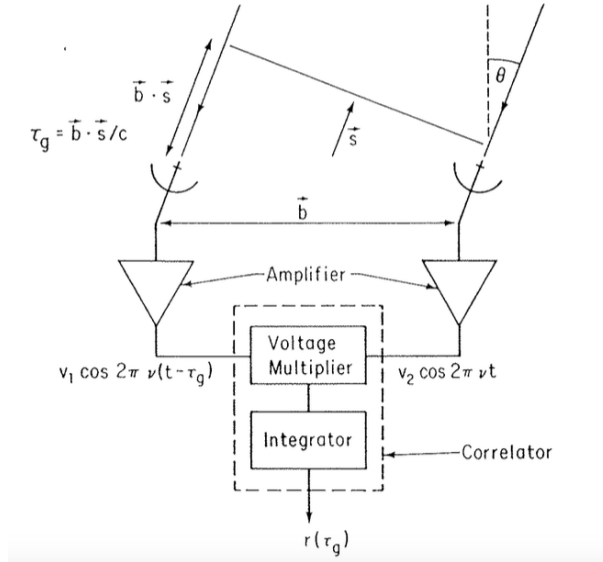


Figure 2.1: Diagrammatic representation of a two-element interferometer Taylor et al. (1999).

The signals from the antennas pass through amplifiers and filters which select the frequency of interest with bandwidth $\Delta\nu$. The voltage signal response produced at the two antennas due to the electric field from this point source, are multiplied together and time-averaged in a device called the correlator (Taylor et al., 1999). That is, for input voltages from two antennas, $V_1(t)$ and $V_2(t)$, the correlator output is proportional to $\langle V_1(t)V_2(t) \rangle$. Below we represent the two voltage signals as,

$$V_1(t) = v_1 \cos 2\pi\nu(t - \tau_g); \quad V_2(t) = v_2 \cos 2\pi\nu t,$$

the correlator output is then,

$$\begin{aligned} r(\tau_g) &= \frac{1}{T} \int_{t-T/2}^{t+T/2} v_1 v_2 \cos(2\pi\nu t) \cos(2\pi\nu(t - \tau_g)) dt \\ &= \frac{1}{2} v_1 v_2 \cos 2\pi\nu \tau_g. \end{aligned} \quad (2.7)$$

We have assumed that the averaging time T is larger compared to $1/\nu$ (Taylor et al., 1999). The result is the interferometer fringe pattern. The correlator output can be recast in terms of the radio brightness integrated over the sky. Let us suppose we have $I(s)$, representing the sky brightness in the direction s at the frequency ν . However, if $A(s)$ is the effective collecting area of an antenna in the direction s , the signal power received by each antenna over a bandwidth $\Delta\nu$ in a solid angle element $d\Omega$ is $A(s)I(s)\Delta\nu d\Omega$. So the correlator signal per solid angle element $d\Omega$ is,

$$dr = A(s)I(s)\Delta\nu d\Omega \cos 2\pi\nu \tau_g.$$

Integrating over the celestial sphere, we obtain,

$$r = \Delta\nu \int A(s)I(s) \cos 2\pi \frac{\mathbf{b} \cdot \mathbf{s}}{c} d\Omega. \quad (2.8)$$

In practice, the angular response of the antenna element falls rapidly to small values outside a narrow angular width defined by their diameter i.e. for large dishes. It is usually more convenient to refer measurements to a reference position \mathbf{s}_0 , commonly referred to as the phase tracking centre (Taylor et al., 1999). Then we have $\mathbf{s} = \mathbf{s}_0 + \boldsymbol{\sigma}$ and,

$$\begin{aligned} r = & \Delta v \cos \left(2\pi v \frac{\mathbf{b} \cdot \mathbf{s}_0}{c} \right) \int A(\boldsymbol{\sigma}) I(\boldsymbol{\sigma}) \cos \left(\frac{2\pi v \mathbf{b} \cdot \boldsymbol{\sigma}}{c} \right) d\Omega \\ & - \Delta v \sin \left(2\pi v \frac{\mathbf{b} \cdot \mathbf{s}_0}{c} \right) \int A(\boldsymbol{\sigma}) I(\boldsymbol{\sigma}) \sin \left(\frac{2\pi v \mathbf{b} \cdot \boldsymbol{\sigma}}{c} \right) d\Omega. \end{aligned} \quad (2.9)$$

The complex visibility is defined as,

$$V = |V| e^{i\phi_V} = \int A'(\boldsymbol{\sigma}) I(\boldsymbol{\sigma}) e^{-2\pi i v \mathbf{b} \cdot \boldsymbol{\sigma} / c} d\Omega, \quad (2.10)$$

In eqn. (2.10), $A'(\boldsymbol{\sigma}) \equiv A(\boldsymbol{\sigma})/A_0$ is the normalized antenna beam pattern. Using eqn. (2.10), we write eqn. (2.9) as,

$$r = A_0 \Delta v |V| \cos \left(\frac{2\pi v \mathbf{b} \cdot \mathbf{s}}{c} - \phi_V \right). \quad (2.11)$$

An interferometer is a machine for measuring the visibility, which is nothing more than the spatial coherence function with a different normalization. The amplitude and phase of the visibility (see eqn. (2.12)) is determined after application of suitable calibration.

In practice, in order to make use of eqn. (2.10), we introduce a convenient coordinate system. A commonly used system is the one where the baseline vector is specified in a coordinate system represented by (u, v, w) , where w points in the direction of interest, here w is chosen to point towards the phase tracking centre (\mathbf{s}_0). The coordinates (u, v) are components projected onto the plane perpendicular to w , where u points toward the East and v points toward the North (Taylor et al., 1999). However, for phase centres not at the zenith, they do not necessarily point to the usual North and East directions.

The coordinates (u, v, w) are measured in wavelengths. However, the positions on the sky are defined by l and m i.e. the direction cosines measured with respect to u and v axes. Thus a synthesized image in the l - m plane represents a projection of the celestial sphere onto a plane tangent to the l - m origin (Taylor et al., 1999). In these coordinates, we have,

$$\begin{aligned} \frac{v \mathbf{b} \cdot \mathbf{s}}{c} &= ul + vm + wn, & \frac{v \mathbf{b} \cdot \mathbf{s}_0}{c} &= w, \\ d\Omega &= \frac{dl dm}{n} = \frac{dl dm}{\sqrt{1 - l^2 - m^2}}, \end{aligned}$$

so that eqn. (2.10) can be written as,

$$V(u, v, w) = \int \int A'(l, m) I(l, m) e^{-2\pi i [ul + vm + w(\sqrt{1 - l^2 - m^2} - 1)]} \frac{dl dm}{\sqrt{1 - l^2 - m^2}}. \quad (2.12)$$

Two assumptions are required for eqn. (2.12) to reduce to a two dimensional Fourier transform. First when $|l|$ and $|m|$ are sufficiently small, we have,

$$w \left(\sqrt{1 - l^2 - m^2} - 1 \right) \approx -\frac{1}{2} (l^2 + m^2) w \approx 0,$$

for $|l|$, $|m|$ small, i.e. small field imaging, the dependence of the visibility upon w is very small and can be omitted (Taylor et al., 1999). Another assumption, if the baselines are coplanar, w lie in the direction of the celestial pole so, $w \approx 0$ (Taylor et al., 1999). With the above two assumptions, eqn. (2.12) can be written as,

$$V(u, v) = \int \int A'(l, m) I(l, m) e^{-2\pi i(ul+vm)} dl dm. \quad (2.13)$$

In principle in order to invert the visibilities, eqn. (2.13), we need to have measured the full uv -plane, which we never do. However, eqn. (2.13) can be inverted to give,

$$A'(l, m) I(l, m) = \int \int V(u, v) e^{2\pi i(ul+vm)} du dv. \quad (2.14)$$

$V(u, v)$ is a wave and so consist of the amplitude and phase. To summarize, an interferometer is a device for measuring the amplitude and phase of the complex visibility function. By Van Cittert-Zernike Theorem, the visibility is related to the sky brightness. If the measurement of the visibility is confined to a plane, or if only a small region of the sky is considered, $V(u, v)$ and $I(l, m)$ reduce to a Fourier transform pair. And since the Fourier theory states that any well behaved signal (including images) can be decomposed into its sinusoidal components, we use this theory to retrieve the amplitude and phase of the complex visibility function.

2.1.3 Aperture Synthesis

The fundamental result of the previous section is that, “there is a Fourier transform relationship between the sky brightness and the visibility function” (Taylor et al., 1999). In practice, antenna arrays are used to measure the visibility function on many baselines and therefore at many spatial frequencies.

Unless the telescopes are moved repeatedly to change the baseline spacing and the observations, the two element interferometer provides a very limited information about the structure of the source. As a general case, this process can be speed up by putting a number of telescopes along the baseline (the use of the interferometric arrays). If the array is constituted by N different antennas, each pair is combined as an interferometer, setting each instrumental delay to match the known geometric time delay for that plane wave (having specified a reference point), the time average of the correlation $r_{i,j}$ becomes an estimate of the visibility function $V_{i,j}$, where (i, j) refers to an antenna pair.

There are only $N(N - 1)/2$ ways of combining N antennas, which sets an upper limit on the number of possible visibilities. “Each unique baseline adds a new Fourier component (unique fringe spacing) to be imaged” (Taylor et al., 1999). Furthermore, increasing the number of telescopes, increases the sensitivity. This is known as aperture synthesis, where the signals from a number of antennas are combined to give an effective resolution of the longest baselines. This technique of aperture synthesis helps to produce high resolution images. The most suitable resolution attained with a single radio antenna has historically been of order 20 arc-seconds while that achieved with aperture synthesis can be four orders of magnitude better.

2.1.4 Interpretation of Aperture Synthesis

As a general case, we would utilize interferometric array(s) to measure visibilities for our astronomical source tightly packed over the entire uv -plane. The Fourier transform of $V(u, v)$ (densely packed visibility function) would give us an image of the astronomical source just as it had been observed with a filled aperture telescope with a diameter equal to the diameter of our telescope array:

$$I(l, m) = \int \int V(u, v) e^{2\pi i(ul+vm)} du dv, \quad (2.15)$$

Practically, interferometric arrays and observing strategies will leave gaps in the uv -plane coverage and as a result if we naively take the Fourier transform of the uv -plane sampled only at the measured visibilities we have a dirty image, given by,

$$I^D(l, m) = \int \int V(u, v) S(u, v) e^{2\pi i(ul+vm)} du dv, \quad (2.16)$$

where $S(u, v)$ is the sampling function over the uv -plane, uv -coverage traces the observed spatial Fourier components following the earth rotation. $S(u, v)$ is equal to one, “where we have a measurement and zero otherwise” (Taylor et al., 1999). Typically, our point spread function (PSF) or dirty beam will have more artefacts than would have been the case in the ideal case. Using the term of eqn. (2.16) and the convolution theorem, the dirty image can be described by the following equation,

$$I^D(l, m) = I(l, m) \otimes B(l, m). \quad (2.17)$$

Eqn. (2.17) shows the true image $I(l, m)$, convolved with the PSF or $B(l, m)$, which may depart significantly from the ideal case if $S(u, v)$ is sparse. The dirty beam is described by the following equation,

$$B(l, m) = \int \int S(u, v) e^{2\pi i(ul+vm)} du dv. \quad (2.18)$$

The uv -coverage is a set of baseline vectors. Since it difficult to do science on the dirty image, in the next section we will explain in detail the techniques used to recover the true image.

2.2 Editing and Calibration of the Visibility

In the previous section, we have explained that we are limited to a finite number of antennas and a finite amount of time over which to make the observations. Because of these limitations, there will always be gaps or holes in the measurement of the visibility function.

Measured visibilities are always corrupted by noise (e.g. thermal noise due to receivers or in the case of the Sun, due to the source itself) and instrumental imperfections. However, its not just the sun that can increase receiver noise. Particularly, “at low frequencies (e.g. < 1 GHz), the sky is very bright and often dominates the noise” (Taylor et al., 1999).

The purpose of calibration is to detect errors or to examine the effects of the instrumental and atmospheric factors in the measurements, and recover the true signal.

In the simplest case, this is done by observing simple sources (i.e. point sources) of known flux density, spectrum and shape to derive the response of the instrument and modifications introduced by the atmosphere. Its often the case at low frequencies that there is no such thing as a blank patch of sky. However, a careful inspection of the visibility data is normally performed before calibration. This involves examining samples of data for unexpected amplitude levels or phase variations. This also includes examination of radio frequency interference (RFI) and identifying dead antennas. The antenna is termed dead, when it is not working during the observation.

In the following sections we are going to describe the common procedures adopted to obtain corrected visibilities.

2.2.1 Antenna-based Calibration

For a point of unit amplitude at the phase tracking centre, the visibility function is unity everywhere. We have argued that the visibility measurements should be calibrated because of the noisy interference from various objects. The calibration is performed because visibilities contains wavelength dependent atmospheric and instrumental terms.

The data reduction consist on deriving these terms from the observation of sources with known properties. For practical situations the relation between the observed and the true visibilities can be considered linear and it is possible to write,

$$V_{i,j}^{obs}(t) = G_{i,j}(t)V_{i,j}^{tru}(t) + \epsilon_{i,j}(t) + \eta_{i,j}(t), \quad (2.19)$$

where $G_{i,j}$ is the baseline based complex gain term, the time of the observations is given by t , $\eta_{i,j}$ is a stochastic complex noise term, and $\epsilon_{i,j}$ is the baseline based complex offset term (Taylor et al., 1999). Both V and $G_{i,j}$ have complex values and are general functions of frequency, polarization and time. The use of complex numbers is a convenience, since it describe the combination of two correlator outputs (often termed the Real and Imaginary, or Cosine and Sine correlator outputs) into one complex quantity (Taylor et al., 1999). Thus the complex offset and noises of two independent correlators. The term, $G_{i,j}$, is required to compensate for the atmospheric or instrumental effects.

As we will see in the data analysis chapters, calibration steps involves determining the values of $G_{i,j}$ (deriving the gains). In order to invert eqn. (2.19) and determine the best approximation of the true visibilities $V_{i,j}^{tru}$ from the observed visibilities $V_{i,j}^{obs}$, we would assume average values in periods of time in between which known calibration sources would be observed.

The measured antenna pair gains can be used to correct the correlator output data directly. However, “the best calibration procedure is used to determine the gain factors for individual antennas” (Taylor et al., 1999). The baseline based offset term $\epsilon_{i,j}$, is generally negligible unless a correlator is malfunctioning or unless there

is significant cross-talk between the various antenna channels. It should also be noted that the antenna gains can drift with time, and so we need to calibrate on times shorter than the instrument changes.

The simplest method to determine this term is to observe a part of the radio sky that contains no emission and integrate a few minutes in order to decrease the contribution from the stochastic noise sources.

2.2.2 Amplitude and Phase Calibration

We have outlined the basics of initial calibration, and the relationship between the observed and true visibilities. In this section we are going to explain in detail the calibration made by observations of radio sources in the sky. Calibration using radio source method does not determine the cause of the calibration problem i.e. corruption; it only determines the complex gains of the entire system at a specific time and in a specific direction (Taylor et al., 1999). Calibrator sources are most useful for determining temporal variations over time-scales longer than about a few minutes. Some of these variations are associated with refraction variations over the array, caused by the troposphere and the ionosphere.

The output of an interferometer or correlator is different from the true astronomical visibility for a variety of reasons i.e. due to instrumental effects and propagation effects in the earth atmosphere and ionosphere.

There are disturbances in the ionosphere due to effects like, solar flare effects, geomagnetic storm effects etc. At low radio frequency (e.g. < 1 GHz), these effects of the ionosphere are most dominant. There are two other effects, however, which are more troublesome. The first is scintillation, where because of diffractive effects the flux density of the source changes rapidly. The flux density modulation could approach 100 percent. The other is that slowly varying, large scale refractive index gradients cause the apparent source position to wander. At low frequencies, the source position could often wander by several arc-minutes, i.e. considerably more than the synthesized beam, which need to be corrected.

Although the scintillation effects cannot be corrected, to correct the other effects we need a source which can either be assumed to be a point source or have well determined structures. These sources can be termed as calibrator sources or simply calibrators.

As a standard observing procedure, calibrator sources are observed at least once an hour or sometimes as frequently as every 10 minutes. “These calibrator observations are not only important for tracking instrumental phase and gain drifts, atmospheric and ionospheric gain and phase variations, but for monitoring the quality and sensitivity of the data and for spotting the occasional gain and phase shifts” (Taylor et al., 1999). However, if a calibrator source is within $\sim 10^\circ$ of the target source, atmospheric phase fluctuations will be better calibrated. With these conditions, “hourly observations of the calibrators are more than sufficient, except at 22 GHz or higher frequencies where they should be no further apart than 30 minutes” (Taylor et al., 1999). So it is required to have a large set of calibrators for observations.

The visibilities $V(u, v)$ are a measurement of amplitude and phase. The phase of an astronomical source (e.g. point source) at the phase centre is known exactly from geometry. After compensating for group delay

the phase for a point source at the phase centre should be zero for every baseline. We observe a strong point source (flux/phase calibrator) periodically during the observations.

Since the phase calibrators amplitudes remain constant during the course of the observations, its measured amplitude provides a measure of the system gain (and its variation) for each baseline. The measured amplitudes and phases of these strong calibrators can be used to determined antennas-based complex gains (as described below). These gains are then applied to the data to obtain true visibilities for the entire observation.

Most data corruption occurs before the signal pairs are correlated, so that the baseline based complex gain $G_{ij}(t)$ can be approximated by the product of the associated antenna-based complex gains, $g_i(t)$ and $g_j(t)$ (see eqn. (2.20)),

$$G_{i,j}(t) = g_i(t)g_j^*(t) = a_i(t)a_j(t)e^{i(\phi_i(t)-\phi_j(t))}, \quad (2.20)$$

where $a_i(t)$ is an antenna-based amplitude correction and $\phi_i(t)$ is an antenna-based phase correction. Observations of calibrator sources determine $G_{ij}(t)$ for each of the $N(N-1)/2$ baselines, where N is the number of antennas. There are algorithms which then solve for the N values of $g_i(t)$.

In general, the gain corrections in time and frequency can be decoupled. The bandpass calibration which determines and corrects for variations in gains as a function of frequency is discussed later.

2.3 Bandwidth Smearing

Synthesis imaging is strictly valid only for monochromatic radiation. “When visibility measurements from a finite bandwidth are gridded as if monochromatic, aberration in the image will result” (Taylor et al., 1999). Radio synthesis telescope have an inherent chromatic aberration, often referred to as bandwidth or delay beam smearing, because they form images by adjusting phase $\Delta\phi$ rather than the arrival time $\Delta t = \Delta\phi/2\pi\nu$ of the correlated signals for each point in the image.

For observations of finite bandwidth this leads to a radial smearing that increases linearly away from the point in the image for which the time delays were equalized (this is known as the delay tracking centre). This aberration may be kept minimum by observations with a set of narrow bandwidth channels, i.e., in spectral line mode, since one may then use the actual central frequencies of each channel rather than the band centre frequency when constructing the images.

For wide field continuum images the maximum bandwidth per channel will be determined by the desire to avoid this delay beam smearing. Although the use of narrow frequency channels can minimise the delay beam smearing, there is still the problem that the uv -coverage itself changes with frequency (Taylor et al., 1999). This is because the Fourier spacings to which an interferometer is sensitive scale with frequency and implies that the point spread function (side-lobe structure) will too (Taylor et al., 1999).

This must be taken into account when analysing the spectral line data cubes or making continuum images using wide bandwidths.

2.4 Deconvolution

In this section we are going to describe how the visibility measurements collected by an interferometric array can be used to produce high quality maps of the sky. The methods that will be used are all non-linear and will generate estimates of the visibility function, $V(u, v)$, at positions in the Fourier plane where it is not measured. According to Taylor et al. (1999), the “deconvolution process or algorithms uses some a-priori knowledge about the image to remove the effect of dirty beam side-lobes”. The two most widely used algorithms are CLEAN and the maximum entropy method (MEM) (Taylor et al., 1999). In this report we will only discuss CLEAN in detail.

The CLEAN algorithm (J. Högbom (1974)), gives solutions to the convolution equation by representing the radio source by a number of point sources in an otherwise empty field of view (Taylor et al., 1999). According to Taylor et al. (1999), “CLEAN uses a simple iterative approach is employed to find the positions and strengths of these point sources”.

Therefore, a final deconvolved map, known as a CLEAN map, is the sum of these point components convolved with a CLEAN beam. Högbom CLEAN often greatly reduce the side-lobes in astronomical images even after the weighting tapers have been applied, since it makes use of the known form of the dirty or synthesized beam to further correct the image while reconstructing it.

CLEAN is a numerical deconvolution process applied in the image domain that relies mainly on the idea of “breaking down the intensity distribution into the sum of point sources responses, and then replace each one of them with the corresponding response to a clean beam, that is a beam free of side-lobes” (Taylor et al., 1999).

After Högbom, other deconvolution algorithms use the same ideas and it is therefore possible to speak of a family of CLEAN algorithms, most are based on the assumption that is somehow possible to model the intensity distribution as a collection of point sources.

Below, we are going to briefly describe Högbom CLEAN one of the current available CLEAN algorithm.

2.4.1 The Högbom Algorithm

According to Taylor et al. (1999), this algorithm proceeds as follows;

1. Compute the map and the response to a point source by Fourier transformation of the visibilities and the transfer function after some weighting has been applied, that is compute the dirty beam and the dirty map. This first step is also needed to initialize a clean component list to a set of zero values.
2. Find the global peak among these images, i.e. the scale that contains the maximum total flux, and record the position, flux, and scale size for the image in which this occurs .
3. Records the position and magnitude of the point source subtracted in the model.

4. Go to (2) except if any remaining peak is below some user specified level. The remainder of the dirty map is now termed the residuals.
5. Convolve the accumulated point source model, with an idealized CLEAN beam (Usually an elliptical Gaussian fitted to the central lobe of the dirty beam).
6. To the CLEAN map formed in (4), add the residuals of the dirty image.

2.5 Data Reduction and Spectral Line Analysis

The data from the interferometer such as GMRT and VLA must undergo editing, calibration, imaging, continuum subtraction and Doppler shift correction. In the following section, we discuss bandpass calibration, self-calibration, continuum subtraction and data cubes.

2.5.1 Bandpass Calibration

The bandpass calibration is used to compensate for the changes of gain with frequency. A strong source with a flat or known spectrum is observed (usually once every few hours). In an ideal interferometer under non-dispersive sky, “the instrumental response would be the same at all frequencies, i.e. the bandpass would be flat with amplitude 1.0 and phase 0.0” (Taylor et al., 1999). However, in reality this is not the case, because a variety of effects ensure that this is not achieved.

Generally there are delays or errors, introduced by dispersion in the delay lines and since they are fairly stable, they can be removed through occasional monitoring measurements. The correlator itself generates some frequency variations. Nevertheless, most of the effects introducing bandpass variations, vary slowly and therefore can be removed through observations of strong point sources (usually also the standard flux calibrator). Note that the bandpass calibrator need not be a point source, so long as its apparent structure does not change over the band.

It is important that the bandpass calibrator is observed long enough so that bandpass calibration does not make a “significant contribution to the signal to noise ratio in the dataset” (Taylor et al., 1999).

2.5.2 Self-Calibration

In this section we will briefly discuss self-calibration which interprets the visibility data by introducing some plausible assumptions about the source structure.

The gain of antenna element is unique to each antenna and its value needs to be calibrated against a target source on the sky. The basis of self-calibration is treating antenna gains as free parameters that can be iteratively adjusted to reconcile the observed visibilities with a model of a target source.

For a baseline, the complex gain $G_{i,j}(t)$ can be approximated by the product of two antenna based complex gains as in eqn. (2.20). However, by clever telescope design, $\varepsilon_{ij}(t) = 0$, we ignore noise for simplicity, therefore,

$$V_{ij}^{obs} \sim G_{ij}(t)V_{ij}^{tru} = g_i(t)g_j^*(t)V_{ij}^{tru}. \quad (2.21)$$

The self-calibration essentially involves producing a model of the sky that when Fourier transformed and corrected by gain factors reproduces the observed visibilities. One can determine the antenna gains by minimizing the sum of the squares of the residuals, as given below,

$$S = \sum_k \sum_{i,j} w_{ij}(t_k) |\bar{V}_{ij}(t_k) - g_i(t_k)g_j^*(t_k)\hat{V}_{ij}(t_k)|^2, \quad (2.22)$$

where w_{ij} are the weights, i.e. purely from signal to noise considerations, each should be set to the reciprocal of the variance of ε_{ij} . The time over which the gains should be held constant i.e. the solution interval depends upon the required signal to noise ratio to obtain reliable solutions and upon the variations introduced by the atmosphere and telescope.

An interesting and illuminating connection to ordinary calibration is apparent if eqn. (2.22) is re-expressed as (Taylor et al., 1999),

$$S = \sum_k \sum_{i,j} w_{ij}(t_k) |\hat{V}_{ij}(t_k)|^2 |X_{ij}(t_k) - g_i(t_k)g_j^*(t_k)|^2, \quad (2.23)$$

where,

$$X_{ij}(t) = \frac{\bar{V}_{ij}(t_k)}{\hat{V}_{ij}(t_k)}. \quad (2.24)$$

The main advantage of self-calibration is that fairly robust gain solutions can be derived as a function of time, in the direction of source (which is most of the times not possible through observations of primary and secondary calibrators), however the results and the speed of convergence depend on the initial source model.

An example of an iterative process that both solves for antenna gains and bootstraps the sky model is the following:

1. Create an initial source model, typically using calibrations based on the observations of primary and secondary calibrators.
2. Solve for complex gains; often starting with phase-only solutions and solving for both amplitude and phase in subsequent iterations.
3. Examine the derived solutions.
4. Apply the gains to correct the observed data.
5. Make a new model, from the corrected data.
6. Go to (2), unless the current model is satisfactory.

These are the steps for performing self-calibration. Below we introduce continuum subtraction.

2.5.3 Continuum Subtraction

Often the goal of spectral line observing and data reduction is to produce a cleaned data cube containing only the spectral line emission or absorption. The data cube is produced by imaging each frequency channel in the spectral line data the same way as would be applied to the single channel in a continuum data set. Channels can be used individually, but usually they are assembled into a single data structure with three axes, namely; right ascension, declination and frequency (Taylor et al., 1999). However, mathematically a data cube is not a true cube, its axes have two different types of units, angle and frequency, and it does not necessarily have the same number of pixels on each axis (Taylor et al., 1999).

In spectral line analysis, continuum subtraction is one of the first steps to be carried out after all the calibrations have been applied to the visibility data set. To begin with, subtraction of the continuum makes it easier to see the spectral line and to compare the emission or absorption in different channels, and then one does not have to deconvolve repeatedly the same continuum emission common to all the channels (Taylor et al., 1999). Thus, subtracting the continuum reduces, and in some cases avoids entirely, the effort involved in deconvolving line signal. This is a particularly beneficial because deconvolution is inherently non-linear and may give rather different results for different channels simply, because the (u, v) coverage and the noise are different (Taylor et al., 1999).

The continuum signal can be subtracted in the image plane or in the (u, v) data i.e. visibility plane. In the (u, v) data plane, the reduction steps involve, fitting a smooth function to the data for each baseline in the line free channels, and subtracting the function from the baselines. Alternatively, one can also make a continuum image using line-free channels and then subtract the model visibilities corresponding to these from the original dataset. Eventually, in both the approaches, the continuum subtracted dataset is Fourier transformed, and if necessary, deconvolved to make the spectral line cube (Taylor et al., 1999).

2.5.4 Velocity Reference Frames and CVEL

Most radio telescopes are attached to the surface of the Earth, so they are in the topocentric rest frame. However, most astronomical objects are not. Since spectral line observations give us a lot of information about velocities of the objects that we are observing, it is important to be clear on what velocity reference frame we are using. The control systems of most radio telescopes can transform among several rest frames by allowing for the Earth's rotation and orbital motion, the solar motion, and centre of mass effects within the solar system. The observing frequency is then tracked to keep a spectral line centred in a specific channel (Taylor et al., 1999).

Without this tracking, we may even see our spectral line shifting from channel to channel during the course of a single day observation i.e. resulting in the smearing of the line signal. The tracked frequency is usually called the sky frequency and it varies from day to day for our objects.

The velocity frame to use depends on the science objectives. For our observations presented in the thesis,

we are going to use barycentric (BARY) or heliocentric (HELIO) frames. The barycentric system is commonly used in observing galaxies, and the barycentric velocity is listed in many catalogs (Taylor et al., 1999). There are other reference frames such as the Local Standard of Rest (LSR) frame. This frame actually has two definitions of LSR, the kinematic LSR (LSRK) and dynamic LSR (LSRD). Most of the time LSRK is used and is generally synonymous with LSR. Velocities of objects in the Milky Way are often catalogued relative to LSR.

If we had to image our line datasets without correcting for the Doppler shift, we would end up blending/smearing our spectral features across channels. For this reason, spectral regridding of the data set is done prior to the imaging. For this purpose, the `CVEL` task has been developed in CASA. We will be using `CVEL` to correct for the Doppler shift, and at the same time, change the velocity reference frame to the BARY.

In the next chapters we are going to apply all the radio interferometry techniques covered in these sections to reduce the data set from GMRT and VLA.

GMRT Search for H I 21-cm Absorption Towards SDSS J1443+0214

In this chapter, we apply the principles of radio interferometry and data analysis discussed in the previous chapters to analyse a dataset from the Giant Metrewave Radio Telescope (GMRT). These GMRT data were taken on June 2, 2012 to search for H I 21-cm absorption towards the quasar from the Sloan Digital Sky Survey (SDSS) called SDSS J1443+0214 (see Fig. 3.1). The quasar is at redshift, $z_q=1.82$ and shows optical emission lines from a galaxy at $z_g=0.3714$. The presence of galaxy is determined only from the emission lines detected in the SDSS spectrum of the quasar. The SDSS image itself shows no indication of the presence of the galaxy. This implies that the galaxy is very faint. Based on the FIRST survey (Faint Images of the Radio Sky at Twenty-Centimeters), “the background quasar at 1.4 GHz has a peak and the integrated flux densities of 135 mJy/beam and 140 mJy”, respectively (White et al., 1997). The deconvolved source size in the FIRST survey which has a resolution of $\sim 5''$ is $1.26'' \times 0.94''$. This implies that the radio source is compact at the resolution of FIRST survey (White et al., 1997). The objective of the GMRT observation was to search for H I 21-cm absorption from the foreground galaxy at $z_g=0.3714$. The GMRT spectrum from these data are already published by Gupta et al. (2013). We perform a detailed analysis of this GMRT dataset to reproduce the published results.

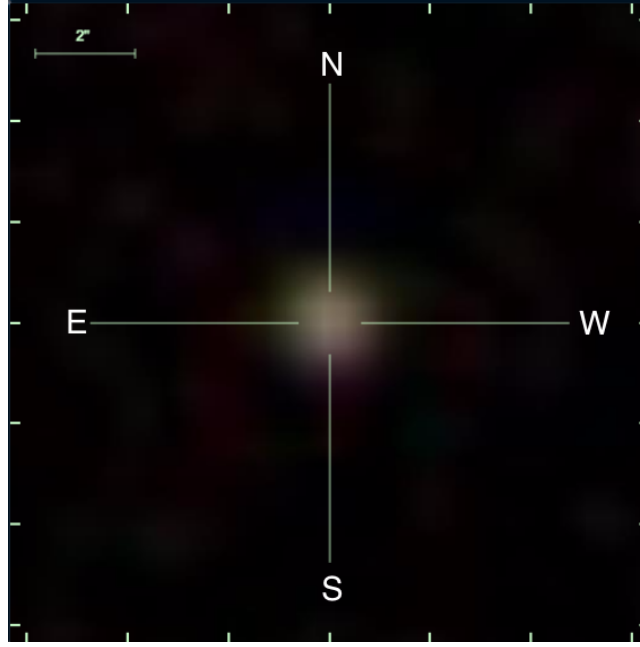


Figure 3.1: The Sloan Digital Sky Survey (SDSS) Data Release 12 image of the quasar J144304.53+021419.3.

3.1 Description of GMRT Observations

The Giant Metrewave Radio Telescope (GMRT) consists of 30 antennas, with diameter of 45 m. The configuration consists of a central core having 14 antennas positioned randomly within 1 km (see Fig. 3.2). This is also called the Central square. The remaining 16 antennas are distributed roughly in a Y-configuration, with the length of each arm being ~ 14 km. The shortest and the longest baseline are approximately 100 m and 25 km, respectively. The hybrid configuration allows GMRT to be sensitive to both small and large scale structures simultaneously. The array is designed to operate at 30 - 1450 MHz. In particular, it operates in six frequency bands which are referred to as 50, 153, 233, 325, 610 and 1420 MHz bands.

The redshifted 21-cm frequency for $z_g=0.3714$ is 1035.73 MHz. Therefore, for the GMRT observation of SDSS J1443+0214 to search for 21-cm absorption, the L-band i.e. 1420 MHz band which covers 1000-1450 MHz was used. The data were acquired in dual polarization mode. The GMRT software back-end was used to split the baseband bandwidth of 4.17 MHz into 512 channels. At the redshifted 21-cm frequency this corresponds to a velocity coverage and spectral resolution of ~ 1210 and 2.4 km/s, respectively. The standard flux density calibrator 3C286 was observed for flux and bandpass calibrations. The compact radio source J1445+099, which is classified as a very good calibrator for all four VLA calibrators and is within $\sim 7.08^\circ$ from the quasar was chosen as the phase calibrator and observed every 45 min for ~ 10 mins.

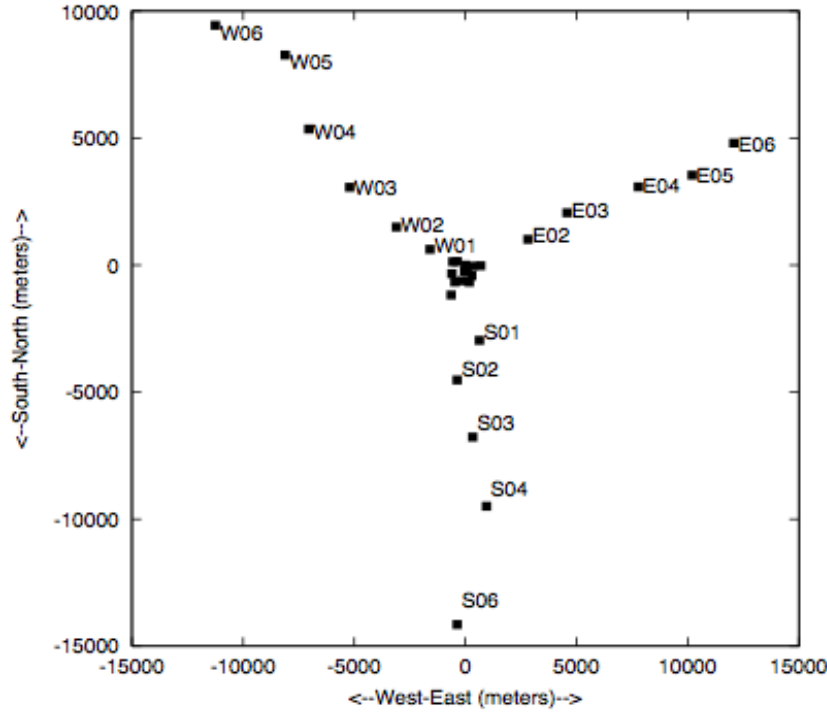


Figure 3.2: The figure shows all the 30 antennas of the GMRT with 14 of them clustered in the Central square and the rest along the Eastern, Southern and Western arms.

3.2 Data Analysis

The results presented in Gupta et al. (2013), were based on the data analysis carried out using the Astronomical Image Processing System package (AIPS). Here we perform the same analysis using the Common Astronomy Software Applications package (CASA) version 4.1.0. CASA is a suite of tools for calibration and analysis of astronomy data from single dish telescopes and radio interferometers. The CASA tasks are Python scripts which use CASA tools and are intended to be tasks that are commonly performed when analysing astronomical data. The first step in using CASA is to get the data into a usable format. CASA uses its own internal data structure, called a Measurement Set which is nothing more than a set of tables containing the data from the observations. In the following we describe various steps in the analysis.

1. **Importing data into CASA:** The data from the GMRT archive was obtained in the Flexible Image Transport System (FITS) format. Since CASA deals with measurement sets (ms), the first step in the analysis is to convert the FITS data into ms. For this we used the CASA task `importgmrt`.
2. **Obtaining a summary of the observation:** The next step is to obtain a summary of the ms. We use task `listobs` for this purpose. The output is shown in Fig. 3.3. As can be seen from this, the total observation time was 8.65 hrs. However, only ~ 6 hrs was used on-source i.e. SDSS J1443+0214. The remaining time was mostly used for observing the flux/bandpass calibrator (3C286) and the phase

calibrator (J1445+099).

Observer:		Project:				
Observation: GMRT						
Data records: 746460		Total integration time = 31133.1 seconds				
Observed from 02-Jun-2012/13:51:08.0 to 02-Jun-2012/22:30:01.2 (TAI)						
ObservationID = 0		ArrayID = 0				
Date	Timerange (TAI)	Scan	FldId FieldName nRows SpwIds Average Interval(s)			
02-Jun-2012/13:51:00.0	14:01:12.0	1	0 3C286_0 16530 [0] [16.1]			
14:03:37.0	14:10:19.6	2	1 1445+099_1 10875 [0] [16.1]			
14:14:05.1	14:59:10.9	3	2 J1443+0214_0 73080 [0] [16.1]			
15:00:47.6	15:15:17.3	4	1 1445+099_1 16530 [0] [16.1]			
15:18:46.7	16:03:36.4	5	2 J1443+0214_0 72645 [0] [16.1]			
16:04:56.9	16:11:39.6	6	1 1445+099_1 10875 [0] [16.1]			
16:14:52.8	16:59:42.6	7	2 J1443+0214_0 72645 [0] [16.1]			
17:01:03.1	17:07:45.7	8	1 1445+099_1 10875 [0] [16.1]			
17:11:15.1	17:56:04.9	9	2 J1443+0214_0 72645 [0] [16.1]			
17:57:25.4	18:04:08.0	10	1 1445+099_1 10875 [0] [16.1]			
18:08:09.6	18:19:58.3	11	0 3C286_0 19140 [0] [16.1]			
18:23:11.6	18:29:54.2	12	1 1445+099_1 10875 [0] [16.1]			
18:33:07.5	19:18:13.3	13	2 J1443+0214_0 73080 [0] [16.1]			
19:19:50.0	19:26:32.6	14	1 1445+099_1 10875 [0] [16.1]			
19:30:18.1	20:15:07.8	15	2 J1443+0214_0 72645 [0] [16.1]			
20:16:28.4	20:23:11.0	16	1 1445+099_1 10875 [0] [16.1]			
20:26:56.5	21:11:46.2	17	2 J1443+0214_0 72645 [0] [16.1]			
21:13:06.8	21:19:49.4	18	1 1445+099_1 10875 [0] [16.1]			
21:23:18.8	21:52:34.4	19	2 J1443+0214_0 47415 [0] [16.1]			
21:54:11.0	22:04:39.1	20	1 1445+099_1 16965 [0] [16.1]			
22:09:29.0	22:30:09.2	21	3 3C468.1_0 33495 [0] [16.1]			
(nRows = Total number of rows per scan)						
Fields: 4						
ID	Code Name	RA	Decl Epoch SrcId nRows			
0	3C286_0	13:31:08.285553	+30.30.32.86297	J2000	0	35670
1	C 1445+099_1	14:45:16.475854	+09.58.36.06985	J2000	1	120495
2	J1443+0214_0	14:43:04.506097	+02.14.19.26959	J2000	2	556800
3	3C468.1_0	23:50:54.877446	+64.40.18.33706	J2000	3	33495
Spectral Windows: (1 unique spectral windows and 1 unique polarization setups)						
SpwID	Name	#Chans	Frame	Ch1(MHz)	ChanWid(kHz)	TotBW(kHz) Corrs
0	none	512	TOPO	1037.663	8.138	4166.7 RR LL
Sources: 4						
ID	Name	SpwID	RestFreq(MHz)	SysVel(km/s)		
0	3C286_0	0	1037.666624	0		
1	1445+099_1	0	1037.666624	0		
2	J1443+0214_0	0	1037.666624	0		
3	3C468.1_0	0	1037.666624	0		

Figure 3.3: The `listobs` output showing the scan summary, source coordinates and frequency set-up for the observations. The target SDSS J1443+0214 is referred to as Field ID 2.

The `listobs` output also provides the frequency set-up used for the observations. As can be seen, the baseband bandwidth of 4.17 MHz which is split into 512 frequency channels and starting from 1037.663 MHz was used for the observations. Generally, it is a good idea to save the `listobs` output for future reference, as it gives the basic structure of the observations, indicating for example which source was observed at what time. As GMRT observations are usually reduced with AIPS, our choice of using CASA to reproduce the results, also enables some comparisons between the CASA and AIPS.

- Inspecting and flagging 3C286 visibilities:** A careful inspection of the flux calibrator is needed to identify bad data. As bad data can lead to wrong calibration we need to identify and flag these so that they are not included in the calibration procedures. For this, we display the data set in various ways. As the first step in calibration is to determine gains as a function of time, we first focus on identifying bad data for a single frequency channel. For this purpose, we choose channel 100 which is far away from the band centre i.e. likely to be free from line emission/absorption. The channel is also away from the band edges to reliably identify bad data.

We use `task plotms` to plot the visibilities of 3C286 for channel 100. In CASA tasks, one can use either the source name e.g., `field = 3C286` or the source ID e.g., `field = 0` to specify a particular

source. We set `spw = 0:100` to select the data for channel 100. The output is shown in Fig. 3.4 where we plot amplitudes and phase as a function of uv-distance.

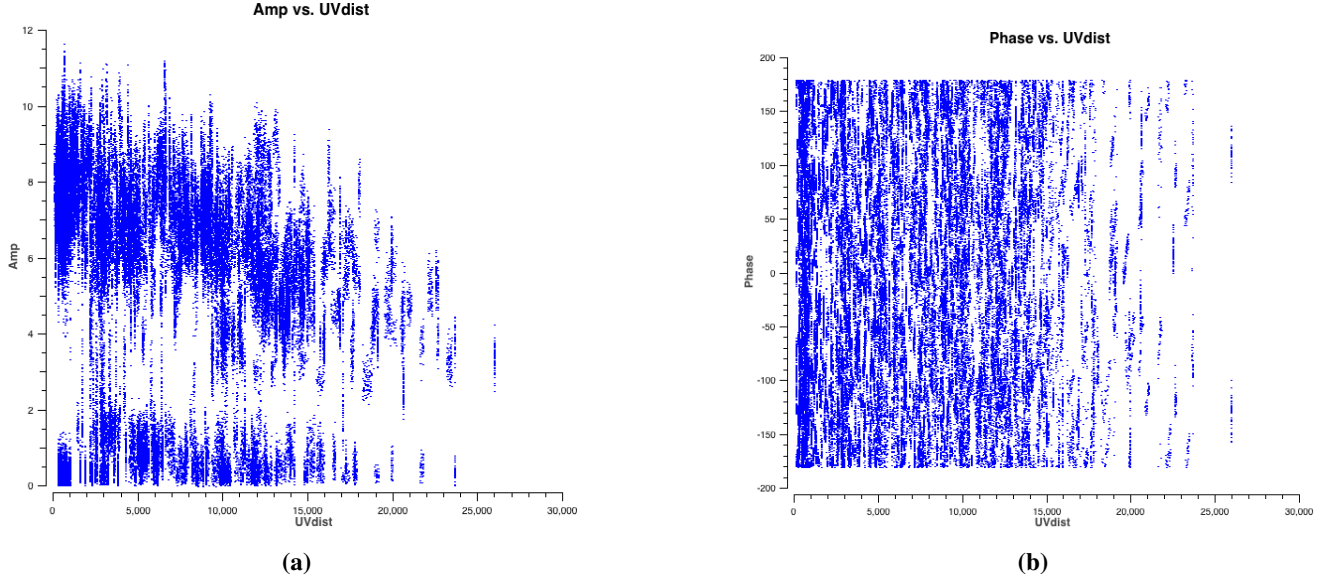


Figure 3.4: Amplitude and Phase vs uv-distance for 3C286.

As 3C286 is a point source (unresolved) for GMRT at L-band it should give us constant amplitudes and phase with respect to uv-distance. But since the data plotted in Fig. 3.4 are uncalibrated this is not the case. Also we notice that amplitudes for several baselines are close to zero. These may be coming from antennas not working during the observations. We identify that these data are corresponding to four bad antennas, W03, C10, S01 and W05. Plotting individual baselines for these antennas shows that the phases with respect to time are totally random. This further confirms that the antennas were not working and the amplitudes are not low because of the low gain of these antennas. We use task `flagdata` to flag the antennas, W03, C10, S01 and W05 for all sources and all times. Next we iterate over the baselines of remaining antennas to identify time-ranges with problems and flag these using `flagdata`. The data after flagging are shown in Fig. 3.5. Most of the low amplitude visibilities have been accounted for.

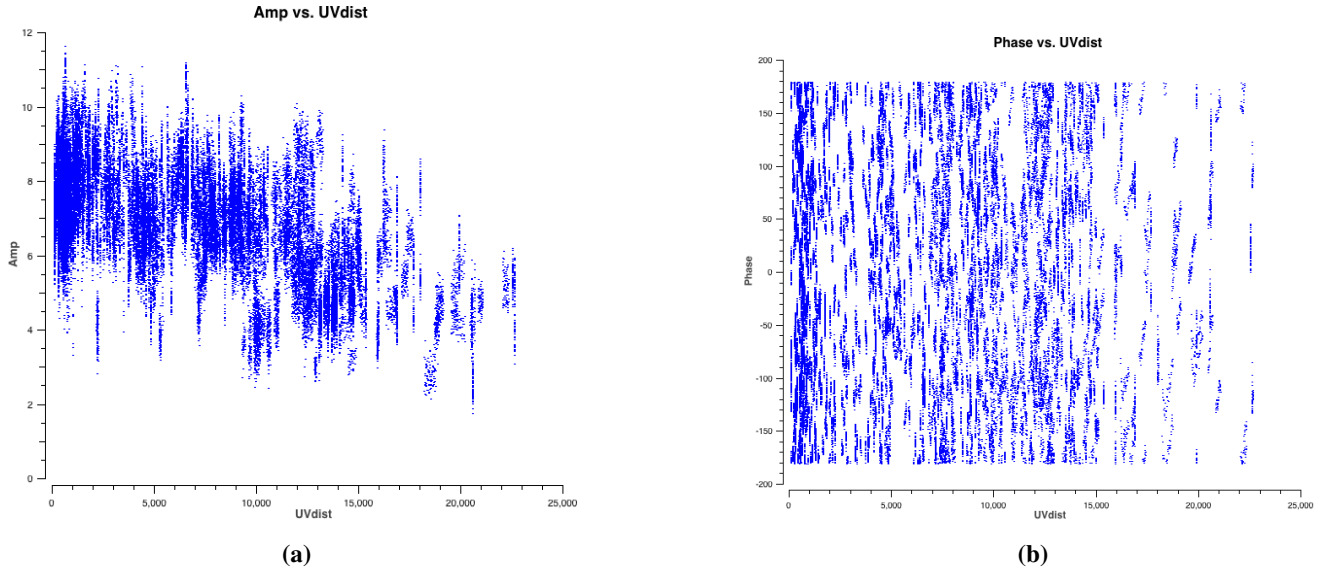


Figure 3.5: Amplitude and Phase vs uv-distance for 3C286, after initial inspection and flagging of the data.

4. **Obtaining the model of 3C286 :** CASA already has models (clean component image) for standard flux density calibrators such as 3C286 at various frequencies. We use task `setjy` to fill the model visibility column for 3C286 with the amplitudes and phases corresponding to the source model at the observing frequency. We chose the fluxscale to be `standard = 'Perley-Butler 2010'` and set `fluxdensity = -1` which allows us to choose the default standard values. `Setjy` produces the output in the logger, from which one can see that it has identified calibrator source 3C286 and computed the flux density of 16.96 Jy at the observing frequency for stokes I.
5. **Choosing the reference antenna:** All the calibration procedures require choosing a reference antenna. Using task `plotants` we look at the graphical plot of the GMRT antenna positions (see Fig. 3.2). This plot is useful for picking a reference antenna. Typically, an antenna close to the centre of the array is a good choice, and having no problems during the observations. In our analysis we will use antenna C01 as the reference antenna.
6. **Solving for antenna based gains for 3C286:** We use task `gaincal` to solve for antenna based complex gains for 3C286. We set the parameter `spw = 0:100` to select the data for channel 100 as mentioned above and `calmode = ap` to specify amplitude and phase calibration. We set the `solint = 1 min`. The table produced by the task `gaincal` is then applied to the flux calibrator using task `applycal` to check if the flagging and calibration are well done. As before we use task `plotms` for inspection. But this time we set the input parameter `datacolumn = corrected` instead of `data`. The calibrated data plotted this way are shown in Fig. 3.6. The amplitudes and phases are as expected for a standard flux density calibrator.

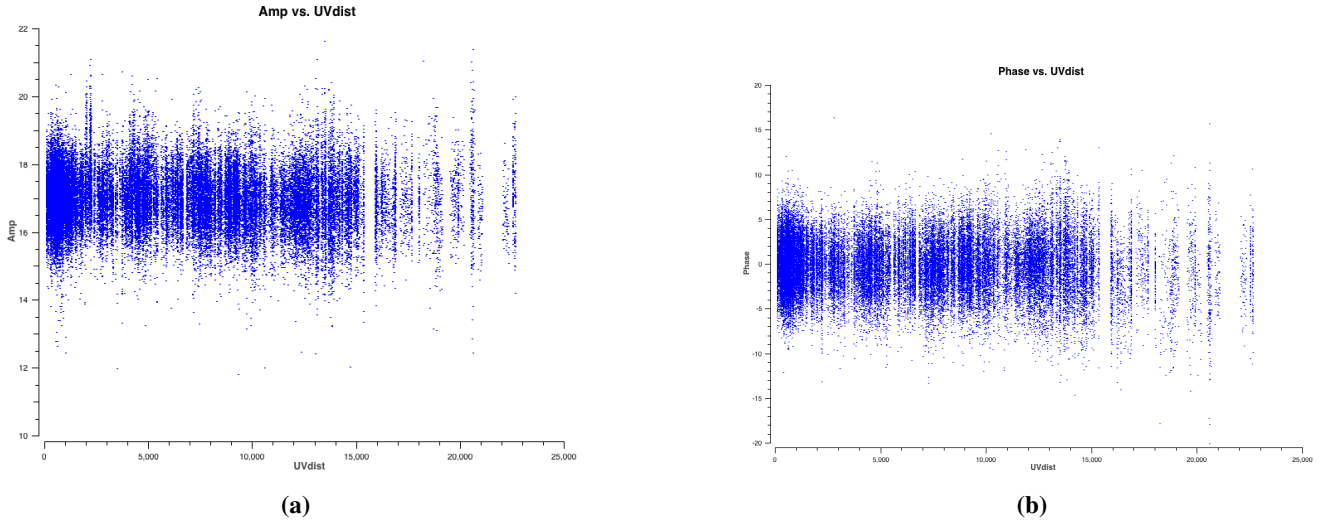


Figure 3.6: Amplitude and Phase vs uv-distance for 3C286, after flagging and calibration.

7. RFI inspection: In this step we identify and flag radio frequency interference (RFI) in the calibrated baseline based visibilities for 3C286. We use `CASA viewer` for this. Using `viewer` we can plot the data for each baseline as a raster plot with x-axis as frequency channel and y-axis as time. The calibrated visibilities for a baseline (C01-C02) are shown in the left panel of Fig. 3.7. The visibilities affected by RFI appear as a bright horizontal line. This is true for RFI appearing at a particular time. RFI appearing at a particular frequency (e.g. satellite) will be seen as vertical line in the plot shown. To flag these, we use the mouse to draw a region around the corrupted visibilities and double click in that region. This region (blue) in Fig. 3.7 (right panel) shows the flagged visibilities. Like this we examined all the baselines to identify and flag RFI affected data.

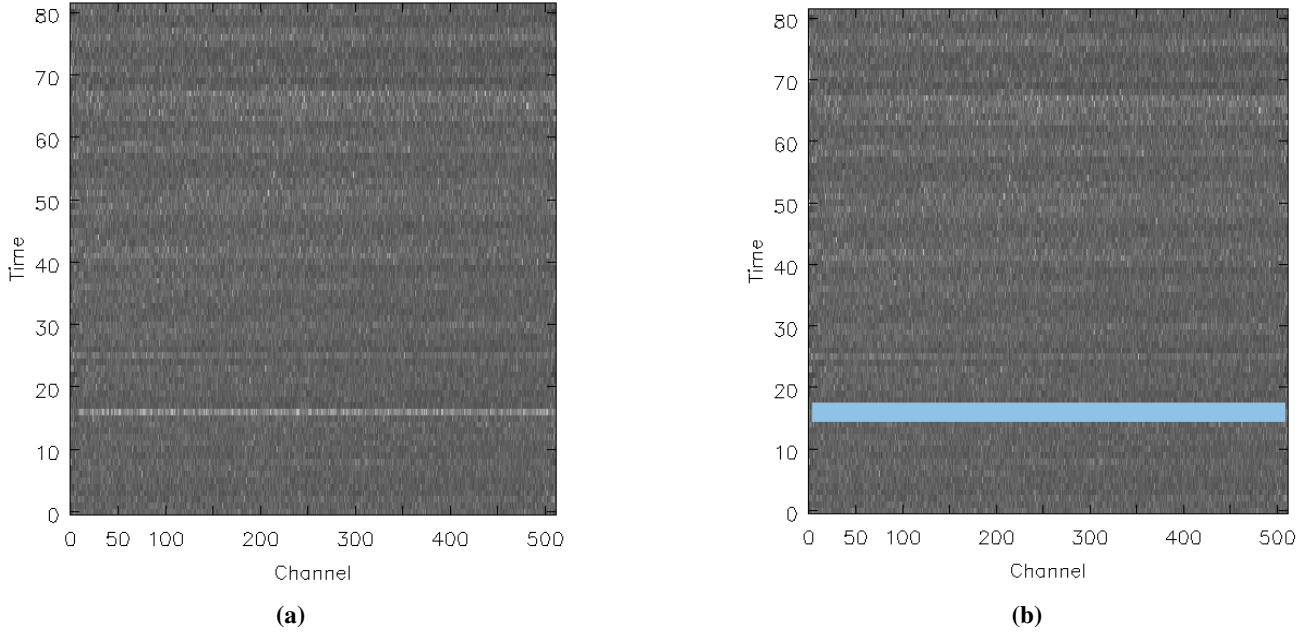


Figure 3.7: RFI inspection for 3C286 calibrated visibilities. (a) Unflagged RFI appear as a bright horizontal line, (b) Flagged data is marked in blue.

8. **Determining bandpass calibration:** After successfully determining gains as a function of time for 3C286 and flagging RFI affected visibilities, the next step is to determine gains as a function of frequency. This is done using the task `bandpass`. We use the input `solint = inf`. This will derive one bandpass solution for the whole 3C286 scan. We also use `combine = scan`. If there had been two observations of the bandpass calibrator (for example), this command would have combined the data from both the scans to form one bandpass solution. During this procedure, we apply the calibration table obtained when we performed task `gaincal` on the fly with the parameter `gaintable`. This allows us to average 3C286 over the entire scan without losing the signal-to-noise ratio. Bandpass calibration simply builds a table with the amplitude and phase as a function of frequency for each spectral window containing more than one channel. Typically, solutions are near unity for the central channels and decrease near edges. The bandpass solutions for nine of the GMRT antennas are shown in Fig. 3.8.

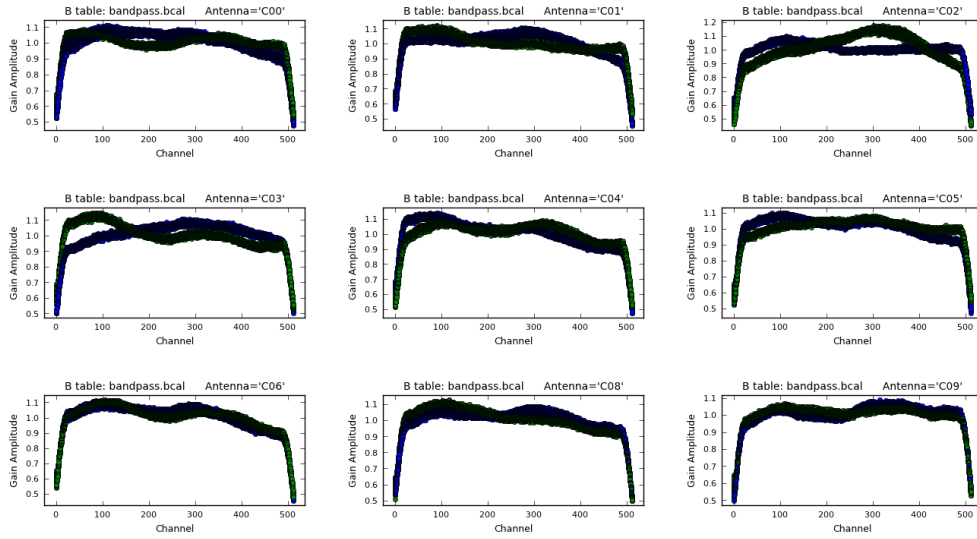


Figure 3.8: Bandpass solution for nine GMRT antennas. The different colours represent different polarizations.

9. **Solving for antenna based gains for J1445+099:** We chose J1445+099 to be the phase calibrator because it is close to SDSS J1443+0214. Therefore atmospheric phase fluctuations between the two will be correlated. The phase calibrator was inspected following the same procedure as in the flux calibrator. We use task `gaincal` to solve for antenna based amplitudes and phases for J1445+099. We set the parameters `spw = 0:100`, `solint = 1 min` and `calmode = ap` as before. But for this step, we apply the bandpass solutions on the fly, specified in `gaintable` input parameter, and we use `field = 0,1`. This task generates a second `gaincal` table.

10. **Fluxscale:** The next step is to set the flux density scale using task `fluxscale`. We use the flux calibrator whose flux density was set in `setjy` to derive the flux density of J1445+099. For this step, we apply the table produced in step (9) on the fly while running task `fluxscale`. After using task `fluxscale` we get that the flux density of our phase calibrator J1445+099 to be 2.57 ± 0.02 Jy.

To check whether or not the application procedure was correct, we use task `applycal` to apply the calibration solutions to the phase calibrator itself. We apply both the `bandpass` and `gaincal` tables for this purpose and use task `plotms` to examine the calibrated data. The calibrated data are shown in Fig. 3.9. We stress that for a point-like source amplitude should be flat (and without any ripples) and the phase should be flat and centred at 0 degrees.

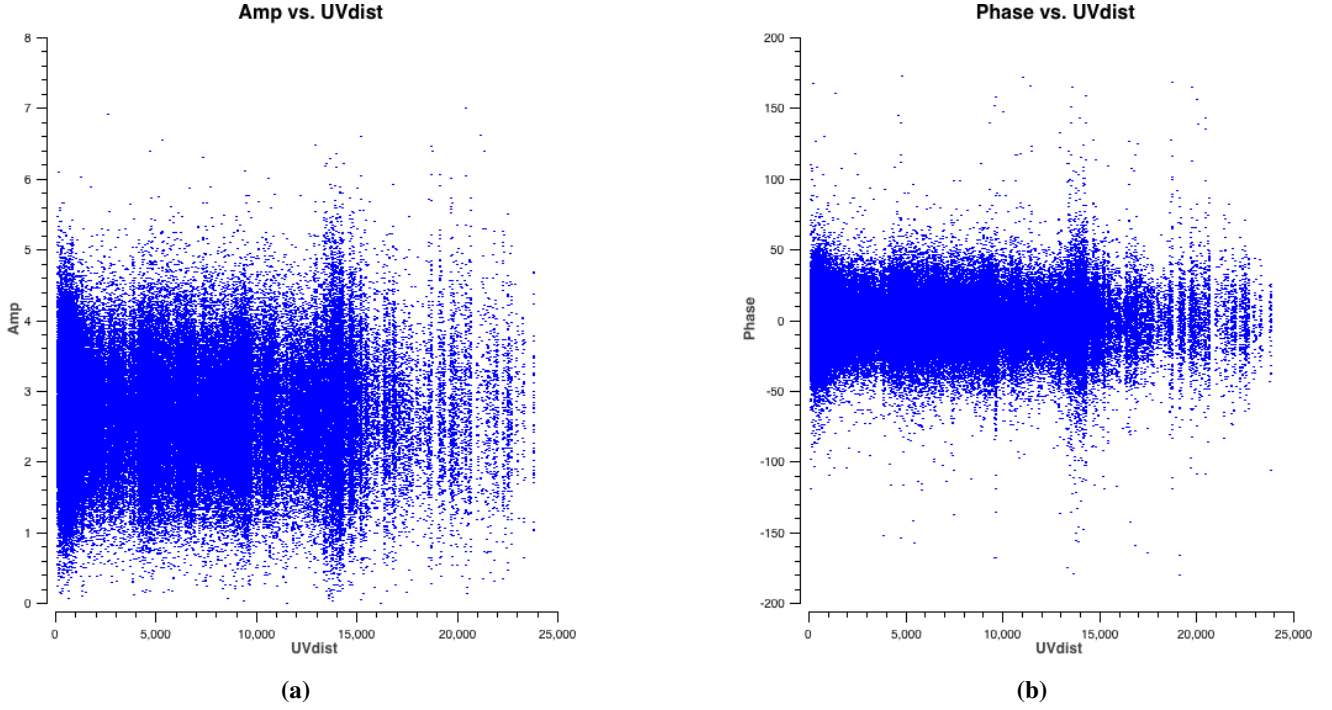


Figure 3.9: Amplitude and Phase vs uv-distance for phase calibrator, after flagging and calibration.

11. **Apply calibration to calibrators and target source:** In this step we use task `applycal` to interpolate the gains in time and apply the calibration tables i.e. both gains as a function of time and frequency, to the calibrators and the target source. We do this by setting the `gainfield` and `gaintable` parameters appropriately. RFI inspection was performed on the target source after applying the calibration.
12. **Splitting the calibrated data:** The next step is to split the calibrated data for calibrators and target source into separate files using task `split`. This speeds up the processing for subsequent steps. Any further analysis will be done on these splitted data files.
13. **Continuum imaging:** As mentioned above, the task `split` was used to separate the uv-data for each source. In this step we make a single channel map of the calibrators and the target source. This is done by using task `clean` in CASA. This task was used to Fourier invert the calibrated data for channel 100 and then perform CLEANing i.e. deconvolution. We use the input parameter `mode = mfs` which makes a single multi-frequency synthesis image out of the specified channels. Input `psfmode = clark` sets the algorithm to make the synthesized beam, and the parameter `imagermode = csclean` sets the mode of the CLEAN. We set the image size and the pixel size with input parameters, `imsize = 1024` and `cell = 0.5 arcseconds`, respectively. The pixel size was determined from the resolution (R) of the interferometer, where the pixel size is $\frac{1}{3}R$ ($R \sim 1.73$ arcseconds). The task `clean` creates five datasets with extensions `.flux`, `.image`, `.model`, `.psf`, and `.residual`. Fig. 3.10 shows CLEAN maps of flux calibrator and phase calibrator, which has flux densities and rms of 16.96 ± 0.01 Jy, ~ 9.33 mJy/beam/channel and 2.57 ± 0.02 Jy, ~ 2.97 mJy/beam/channel, respectively.

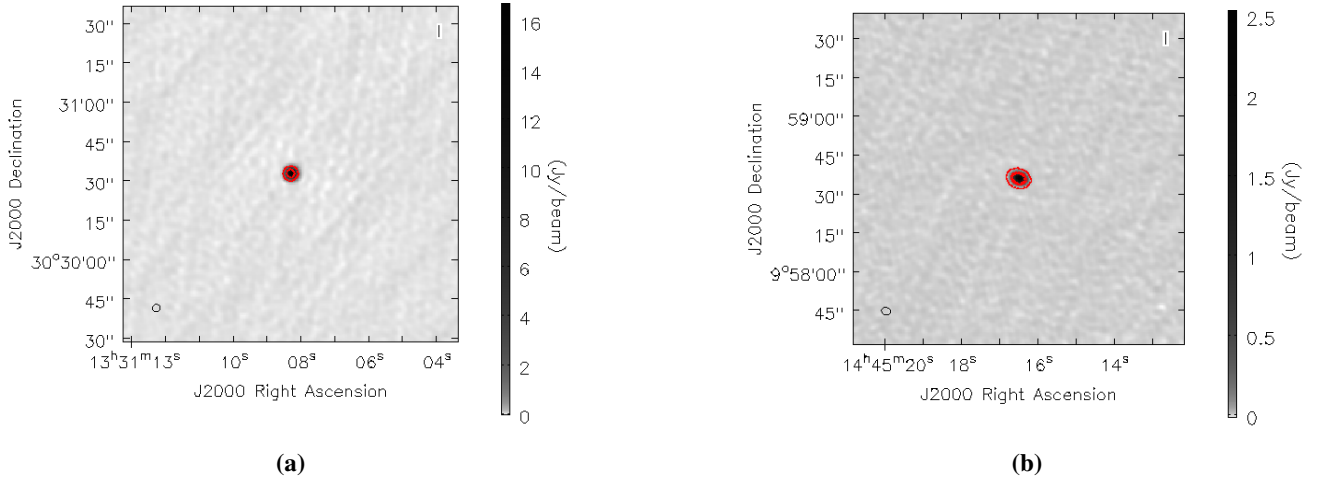


Figure 3.10: Single channel maps, of (a) 3C286 and (b) J1445+099. The contour levels start at 3σ .

Fig. 3.11 (a) shows the single channel map of SDSS J1443+0214, which has a flux density of 113.83 mJy and rms of ~ 1.58 mJy/beam/channel. Clearly, there are significant phase and amplitude errors in the map, as a result of which the target source does not come out as a point source.

In the next step, we make a channel averaged continuum image of the target source to obtain the continuum map with best possible signal-to-noise ratio (SNR). As the absorption line is between channels 200 and 350, we use task `split` to select only the line-free channels. We now have two data sets: one with line free channels and the one with all the frequency channels. For obtaining the continuum map, we use the same parameters in `clean` as before, except that now we average all the (line free) channels to make the image (see Fig. 3.11 (b)).

In addition to creating a CLEAN image, `clean` also saves the clean components i.e. model of the target source. The parameter `usescratch = True` tells `clean` to save the visibilities corresponding to this model as a discrete data column in the MS. This model is required for later self-calibration steps. However, as can be seen from the right panel of Fig. 3.11, although the model is not a point source, but is a good starting point for the self-calibration. Compared to the previous single channel image, the errors appear to be larger in this channel averaged image. This is primarily due to the higher SNR in the latter so that the errors which were previously buried in the noise are now detectable.

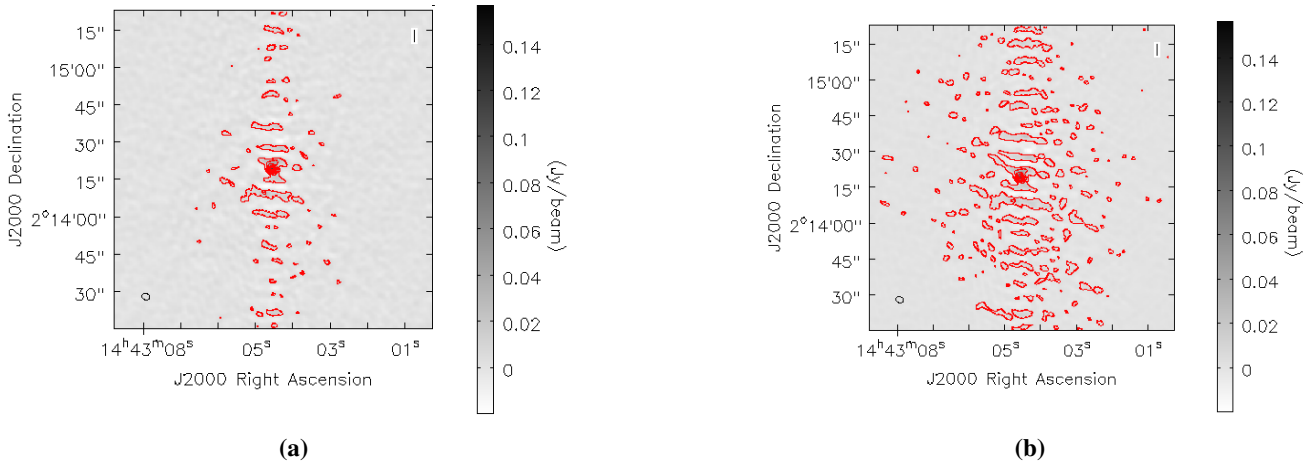


Figure 3.11: (a) Single channel map of SDSS J1443+0214. (b) Channel averaged map of SDSS J1443+0214. The contour levels start at 3σ .

14. **Self-calibration:** In the previous step we made an approximate model, averaging ~ 200 line-free channels. With a reasonable model in place, we are in a position to (self-)calibrate the science target directly. We use task `gaincal` for this purpose. The task is used both for general gain calibration using an external calibrator, and for self-calibration.

We first focus on correcting only for phase errors. For this, we perform phase-only self-calibration using the task `gaincal`. This compares the data column with the model column, which has been filled with the clean components corresponding to the initial model. For phase-only self-calibration, we would like the solution interval to be short enough so that it tracks the changes in the atmospheric phase with high accuracy, but long enough so that we measure phases with good SNR. The solution interval used is `solint = 1.0 min`, and the input `calmode = p` specifies that we are only doing phase only self-calibration. The phase solutions are written in the table produced by `gaincal`. We examine the derived phase solutions using task `plotcal`. We find these solutions to be reasonable and apply these to the line free channel data using task `applycal`.

At this point the self-calibrated data are stored in the MS in the `corrected data` column. Because we want to try more rounds of self-calibration, it is often useful (though not strictly necessary) at this point to split out the channel averaged corrected data into a new data set. The next step is to clean the self-calibrated data to generate the map shown in Fig. 3.12 (a). The residuals look better this time around. We use `viewer` and compare the first (see Fig. 3.11 (b)) and second images (see Fig. 3.12 (a)). One can see a noticeable improvement in the noise and some improvement in the signal, so that the overall signal-to-noise ratio has significantly improved.

The phase-only self-calibration was repeated three times until the map stopped improving further. The results are summarized in Table. 3.1 and Fig. 3.12. In Fig. 3.12 (c), it can be noted that the improvement with respect to the previous image (panel-b) is marginal. Therefore, the next step is to correct for

amplitude errors through amplitude-and-phase (ap) self-calibration.

As amplitude varies much more slowly, the solution interval used for this step is `solint = 15 min` with input `calmode = ap`, specifying that we are doing amplitude and phase self-calibration. The input visibility data for this step is the channel averaged, phase-only self-calibrated dataset. After performing the ap self-calibration, the next step is to make another map using the same `clean` parameters as before (see Fig. 3.12 (d)). We compare the third and fourth images. The noise level is much better, while the flux has not changed markedly.

We attempted another round of ap self-calibration but it did not improve the image further. Therefore, this i.e. the image in panel (d) is our best continuum image. The results of the self-calibration such as peak flux density and rms after each iteration of phase-only or ap self-calibration are shown in Table. 3.1.

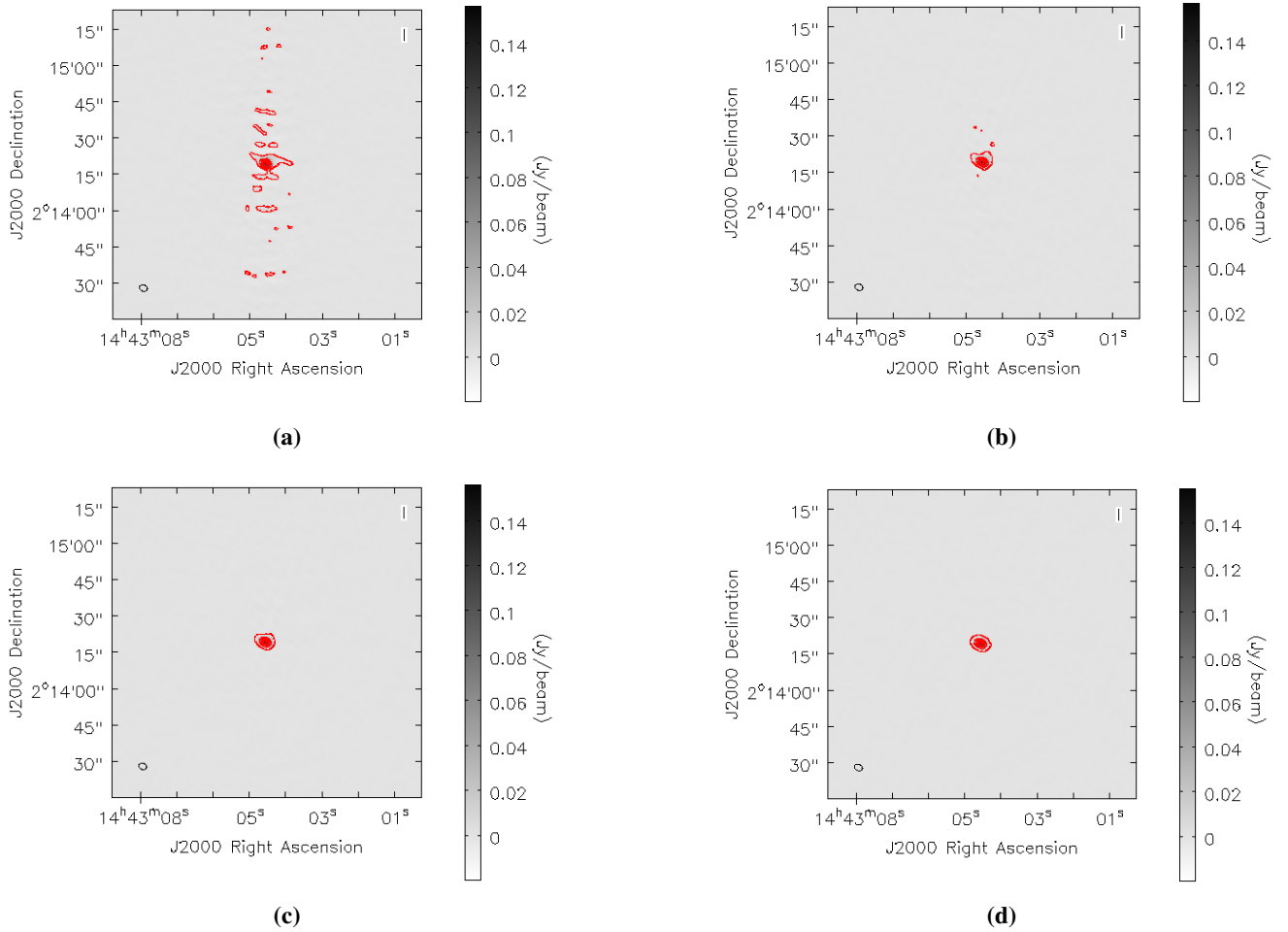


Figure 3.12: Continuum image of SDSS J1443+0214 after phase-only (panels a, b and c) and amplitude calibration (panel d). The contour levels start at 3σ .

Table 3.1: Results of self-calibration.

Model	Peak flux density [mJy/beam]	rms [mJy/beam/channel]	Figure Reference
Initial model	112.90	0.408	Fig. 3.11 panel (b)
1 phase-only	156.87	0.408	Fig. 3.12 panel (a)
2 phase-only	159.75	0.204	Fig. 3.12 panel (b)
3 phase-only	160.37	0.184	Fig. 3.12 panel (c)
1 amp and phase	159.46	0.162	Fig. 3.12 panel (d)

15. **Applying self-calibration solutions to line dataset:** Next step is to apply gains from the last iteration of phase-only and the amplitude-and-phase self-calibration steps to the line visibility data set. We use task `applycal` for this purpose and then split the calibrated data column.
16. **Continuum subtraction:** Next we subtract the continuum from the self-calibrated line data set obtained in step (15) using task `uvconstsub`. This task makes fits to the line free channels and subtracts the emission in the uv-domain. The task `uvconstsub` operates on the corrected data column and writes the continuum subtracted data in a new measurement set with the extension `.contsub`. However, setting the input parameter `want cont = T`, produces two new datasets, including `.contsub` the continuum subtracted data and `.cont` the continuum estimate.
17. **Setting velocity rest frame:** Since spectral line observations give us a lot of information about kinematics of the objects, it is important to be clear on what reference frame we are using. There are two ways to change the rest frames in CASA. The task `clean` can change the reference frame of the spectral axis. However, task `cvel` is a more general spectral regridding tool, which corrects for Doppler shifts, or change the channelisation of the data prior to imaging. For our analysis, we use `cvel` to correct for the Doppler shift, and at the same time, change the velocity reference frame to BARY.

Before we do that, we set the rest frequency of H I 21-cm line in the measurement set. Here we are using an MS file with extension `.contsub` that was produced in step (16). The rest frequency of the H I 21-cm line is 1420.405752 MHz. We open the spectral window table of the MS using `tb.open` and insert the rest frequency using `tb.putcell`. The default rest frequency in the file is the central observing frequency. After inserting the rest frequency we close the file using `tb.close`. We also ran the task `listobs` to check that the reference frequency has been actually changed. Finally, we run task `CVEL`, with input parameter `outframe = BARY` to change the reference frame of this data set.

18. **Imaging the continuum subtracted line data set to obtain the image cube:** Next step is to image the line dataset obtained from the previous step. For this step, we use `clean` as before. This time, We set the input parameter `mode = channel` to produce an image with multiple frequency channels. We

set threshold = 3 mJy i.e. roughly 3 times the expected spectral rms. This forces clean to stop if the maximum residual is below this value. We also set the maximum number of clean iterations to be niter = 200. The clean with these parameters produces the final stokes I image cube. We detect H I 21-cm absorption at the location of the quasar from this cube. The spectrum which has an rms of 1.2 mJy/beam/channel is presented in the next section.

3.3 Results

The studies of H I 21-cm absorption and emission have led to the discovery of neutral interstellar medium (ISM) with temperatures over the range, $\approx 20 - 10^4$ K. These studies have led to models suggesting that there exist, “two distinct stable H I phases which co-exist in pressure equilibrium: a cold, high-density ($n \approx 10 - 100 \text{ cm}^{-3}$) phase, the cold neutral medium (CNM) and a warm diffuse, low-density ($n \approx 0.1 - 1 \text{ cm}^{-3}$) phase, the warm neutral medium (WNM)” (e.g. Roy et al., 2013).

According to Kulkarni & Heiles (1988), “the high number densities in the CNM indicate that the H I 21-cm transition is likely to be thermalized in this phase, with the H I 21-cm excitation temperature (the ‘spin temperature’, T_s) approximately equal to the kinetic temperature T_k ”. In the WNM, “the relation between the spin and kinetic temperatures is complicated”, however, Liszt (2001), suggest that “the spin temperature is expected to be lower than the kinetic temperature in this phase”. The relative filling factors of the different phases remain uncertain and may vary with location in the galaxy (Braun & Walterbos, 1992). Roy et al. (2013) suggest that, “the difficulty of detecting the WNM in H I 21-cm absorption (i.e. due to its low optical depth) has meant that relatively little is observationally known about the physical conditions in the WNM”.

The kinetic temperature and spin temperature, are two different temperature used to describe the conditions in the gas for H I. The physical (kinetic) temperature T_k , characterizes the velocity distribution of the H I atoms in small scales i.e. scales on which bulk motions are negligible. The spin temperature T_s , “it describes the population in the two hyperfine levels of the ground state of neutral hydrogen, i.e. it is defined by the Boltzmann distribution, $n_1 = 3n_0 e^{-h\nu_{10}/k_B T_s}$, where n_0 and n_1 represent the populations in the lower and upper levels of H I 21-cm hyperfine transitions and ν_{10} is the rest frequency of the H I 21-cm line” (Field, 1958).

Field (1958) suggested that, “for a single H I cloud, T_s is determined by a combination of three mechanisms, namely: collisions, the Lyman- α radiation field and the radiation field around the rest wavelength of the hyperfine 21-cm transition”. These mechanisms may cause direct transition between the two hyperfine states. In the ISM, especially in the regions far away from H II regions and Supernovae remnants, the H I 21-cm continuum radiation field generally contributes negligibly to the excitation.

Roy et al. (2013) emphasizes that “in high density regions of ISM (i.e. far from bright UV sources), the collisional mechanism dominates over Lyman- α excitation mechanism and the spin temperature is equal to the kinetic temperature” i.e. this is the case in the CNM. However, the collisions can not thermalize the H I 21-cm transition in the WNM i.e. because the density is very small. Liszt (2001) obtained “ $T_s \sim 1000 - 5000$

K for $T_k \sim 5000 - 10000$ K, for typical ISM pressures, in the absence of external influences (e.g. bright radio sources and sources of UV photons)”.

Roy et al. (2013) argues that, “if the excitation by the Lyman- α in the WNM is intense (e.g. for a single homogeneous H I cloud) and resonant scattering of Lyman- α radiation causes the Lyman- α colour temperature to approach the kinetic temperature, then the spin temperature would be driven to kinetic temperature”. However, this is somewhat uncertain but it does appear reasonable to assume that $T_s \approx T_k$, in the CNM and that $T_s < T_k$ in the WNM. Below we are going to estimate the kinetic and spin temperature following Liszt (2001) discussion.

According to Liszt (2001), “the gas kinetic temperature is typically estimated from the Doppler temperature, T_D , T_D represents the width of the Gaussian core of the line”. “The Doppler temperature is derived from the full width at half maximum (FWHM) of an H I 21-cm component by the relation, $T_D = 21.86W^2$ K, where W is the FWHM (km/s)”, definition used by Payne et al. (1982).

With negligible contributions from bulk motions, turbulence, etc, the line width will be dominated by thermal broadening i.e. one would have $T_k = T_D$. According to Leung & Liszt (1976), T_D is given by the expression,

$$T_D = T_k + \frac{m_H v_{turb}^2}{k_B}, \quad (3.1)$$

where “ m_H is the mass of the hydrogen atom, v_{turb} gives the contribution to the line width from the thermal motions and k_B is the Boltzmann constant”.

One can use T_D and T_k interchangeably i.e. If such non-thermal broadening is negligible. In the general case, “the Doppler temperature only provides an upper limit to the kinetic temperature” (Roy et al., 2013). In H I 21-cm absorption spectra, “both the spin and Doppler temperatures affect the line profile; the spin temperature determines the total integrated optical depth, while the Doppler temperature” i.e. the combination of the “kinetic temperature and any non-thermal motions” determines the line width (see eqn. (3.1)) (Roy et al., 2013). The Doppler temperature measurements shown in Table. 3.2 are estimated using Payne et al. (1982) definition.

Generally, an absorption profile can be treated as arising from a number of absorbing clouds along the line of sight. However, if each cloud of gas is individually in equilibrium, at the kinetic temperature T_k , its line profile would be the Voigt profile. The Voigt profile, is a convolution of the Gaussian function with the Lorentzian, which reduces to a Gaussian for unsaturated absorption lines i.e. if collisional broadening is neglected. As such, “the simplest physically motivated model for an unsaturated absorption profile consists of a sum of multiple Gaussian components, with the width of each component determined by the kinetic temperature of the gas”. In principle, “such a Gaussian de-composition allows one to derive the kinetic temperature of individual clouds” (Roy et al., 2013).

In our analysis, a strong H I 21-cm absorption line is detected at $z_g = 0.3715$ towards SDSS J1443+0214. In Fig. 3.13, we normalized the spectrum using the continuum flux density and fitted two Gaussian components

(Model A & B) simultaneously to model the absorption. Our attempt to use only one component resulted in large residuals. However, using two Gaussian components produce a good fit (having small residuals) to the absorption spectrum. We show the Gaussian fits to the profile (Fig. 3.13) and summarize the results in Table. 3.2. The total integrated H I 21-cm optical depth due to the absorber towards SDSS J1443+0214 was calculated by integrating across the line profile, and is estimated to be $\int \tau dv \sim 3.6 \pm 0.2$ km/s.

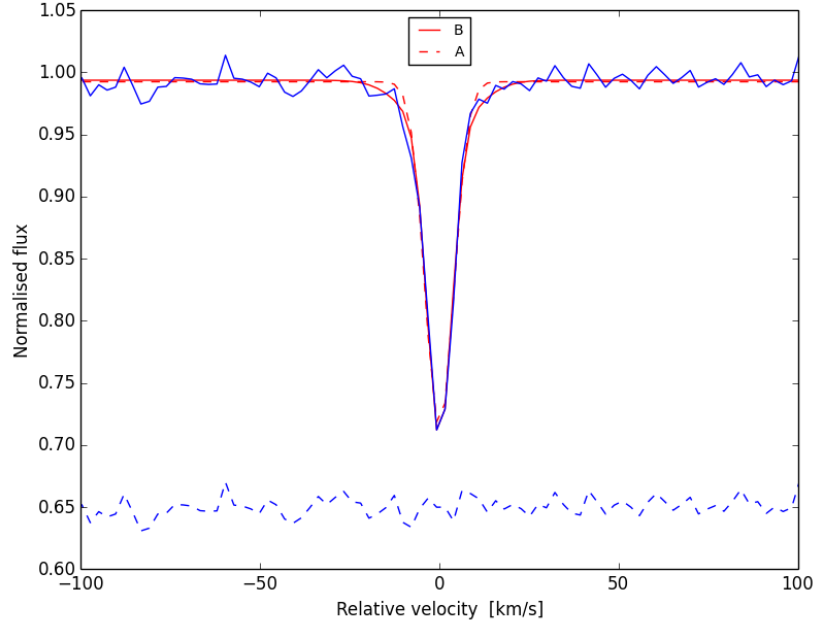


Figure 3.13: The GMRT spectrum showing H I 21-cm absorption detected towards SDSS J1443+0214 . The zero velocity axis corresponds to the 1035.63 MHz. The fitted parameters are given in Table. 3.2. The red lines are the Gaussian fits to the absorption spectrum. Residuals are plotted in dashed line and they are arbitrarily shifted for clarity.

Table 3.2: Two component Gaussian fits to the 21-cm absorption profile.

Quasar	ID	τ_{peak}	FWHM (km/s)	T_k (Kelvin)
SDSS J1443+0214	A	0.290	9 ± 1	1800
	B	0.040	20 ± 4	8800

The H I column density (density projected along the line of sight towards the quasar) for an optically thin cloud is estimated using the relation (e.g. Kulkarni & Heiles, 1988),

$$N_{\text{HI}} = 1.835 \times 10^{18} \times \frac{T_s}{f_c} \int \tau(v) dv \text{ cm}^{-2}, \quad (3.2)$$

where T_s is the spin temperature of H I gas in Kelvin, f_c represents the fraction of H I cloud that covers a background radio source and $\tau(v)$ is the 21-cm optical depth in a velocity interval $v - v + dv$. We assume f_c

to be unity, T_s is an unknown quantity and here we adopt a value of 100 K, typical temperature for CNM in the Galaxy. Using eqn. (3.2), we measure the H I column density to be $\sim 6.6 \times 10^{20} \text{ cm}^{-2}$. Thus this system qualifies as a damped Lyman- α (DLA) and perhaps corresponds to a sight line passing through the disk of a galaxy. Further, the upper limit on the temperature of component A is consistent with it being arising from CNM. The limit on the temperature of component B is too high to draw any direct conclusions. However, since the Hubble Space Telescope (HST) offers a much greater sensitivity, the measurement of H I 21-cm column density using the HST are required to estimate the total H I 21-cm column density along the sight line and put constraints on the spin temperature and physical conditions in the gas. Finally, we also note that the observational results derived from our analysis through CASA are identical to those published in Gupta et al. (2013).

GMRT and VLA Search hydroxyl (OH) Absorption

In the interstellar medium, molecular gas is present over a wide range of densities from diffuse gas to dense clouds. The different types of molecular clouds are classified on the basis of their optical appearance i.e. the visual extinction (A_V). The clouds with $A_V < 1$ and $1 < A_V < 5$ are called diffuse and translucent clouds, respectively. In these clouds, the Carbon, whose ionization potential is less than that of Hydrogen, is mainly in the singly ionized state. The clouds with larger A_V s are referred to as dark clouds. Due to the absence of any ionizing radiation field in these clouds, the Carbon is mostly in neutral state or in CO. Most of the molecular gas in ISM are in Giant Molecular Clouds (GMCs) with masses ranging from 10^3 to $10^5 M_\odot$. These have well defined boundaries and complex substructures, and are the sites of active star formation. Therefore, detecting and understanding the molecular phase is crucial to understand the current and future star formation in galaxy(ies). Molecules are also of overwhelming importance for studying cold regions which do not produce H I emission and are optically thick or opaque to optical lines.

Molecules in ISM can be detected through emission and absorption lines. The first detection of an interstellar molecule at radio wavelengths was the hydroxyl (OH) radical. It was detected at 1667 MHz (18-cm) in absorption against Cassiopeia A by Weinreb et al. (1963). This discovery provided a positive evidence for the existence of OH, and in general the presence of molecular gas, in the interstellar medium. It is now well known that OH is present in both diffuse and dense phases of the molecular ISM.

The ground state of OH has an electronic angular momentum $L = 1$ and spin angular momentum $S = 1/2$. Thus, by spin-orbit coupling, the total angular momentum is either $J = 3/2$ or $J = 1/2$, leading to the $^2\pi_{3/2}$ and the $^2\pi_{1/2}$ rotational states. The microwave transitions of OH in the ground state, $^2\pi_{3/2}$, $J = 3/2$, arise from two Λ -type doublet-levels (i.e. due to the interaction between the rotation of the nuclei and the unpaired electron in the outer shell), each of which is split by hyperfine interactions with the hydrogen nucleus, resulting in four transitions (Weinreb et al., 1963). This splitting is illustrated in Fig. 4.1, where these states are labelled

with ‘+’ and ‘-’ for the higher and lower energy states, respectively.

For our observations to search for OH absorption lines, we chose two quasar sight lines passing through foreground galaxies. Both these sight lines show (i) 21-cm absorption (i.e. the presence of cold atomic gas is confirmed) and (ii) signatures of reddening by dust, thus exhibiting conditions favourable to possess molecules. We searched for OH absorption in these galaxies through observations of OH main lines at the frequencies of 1665.4018 MHz and 1667.3590 MHz.

In this chapter we present GMRT and VLA observations of OH molecular absorption lines towards these quasars, namely, SDSS J1443+0214 and SDSS J0849+5108 (see Fig. 3.1, and Fig. 4.15). First, we are going to focus on the quasar SDSS J1443+0214, at redshift, $z_q = 1.82$. This system has already been introduced in the previous chapter and H I 21-cm absorption line was detected at $z_g = 0.3715$. The H I 21-cm absorption from the galaxy at $z_g = 0.3120$ towards the quasar SDSS J0849+5108, $z_q = 0.584$ has been presented in Gupta et al. (2013).

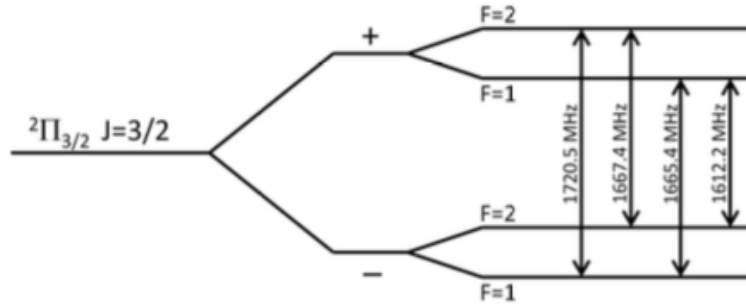


Figure 4.1: The 18-cm ground state transitions of the OH molecule. These transitions are due to hyperfine interactions with the nuclear spin, and each doublet state is further split into 2 levels, corresponding to $F = J + I$, where I is the nuclear spin, equal to $\pm 1/2$. Transitions between these 4 independent energy states result in the 18-cm ground state spectral line at ~ 1612 , 1665, 1667, and 1720 MHz.

4.1 GMRT Search for OH Absorption Towards SDSS J1443+0214

4.1.1 Description of GMRT Observations

The GMRT observation of OH was carried out in January, 2013 using a baseband bandwidth (for observations at L-band) of 4.17 MHz split into 512 spectral channels (resolution ~ 2 km/s). A summary of the observation is given by the `listobs` output in Fig. 4.2. The standard flux density calibrator 3C286 within $\sim 33.7^\circ$ from the quasar was observed twice during observing track for both flux and bandpass calibration. The compact radio source J1445+099 within $\sim 7.08^\circ$ from the quasar was chosen as the phase calibrator and observed every 45 min for ~ 10 mins.

4.1.2 Data Analysis

The NRAO CASA package (version 4.1.0) was used for data reduction, following standard procedures as described in the previous chapter. As usually, the data of flux-density calibrator, phase calibrator and target source were inspected at various stages for bad antennas, baselines and time ranges. The observations, especially the data on phase calibrator J1445+099 and the target source SDSS J1443+214, were affected by radio frequency interference (RFI).

In the following we describe various steps in the analysis. As we are using GMRT for the observations here, therefore the first step follows exactly like in the previous chapter where we convert the data from FITS format into a MS using the task `importgmrt`.

1. **Obtaining a summary of the observation:** The summary of the measurement set is shown in Fig. 4.2. We use task `listobs` for this purpose. The total observation time was 8.20 hrs. However, only ~ 6 hrs was used on-source i.e. SDSS J1443+0214. The remaining time was mostly used for observing the flux/bandpass calibrator (3C286) and the phase calibrator (J1445+099).

Observer: Project:	
Observation: GMRT	
Data records: 723405 Total integration time = 29490.3 seconds	
Observed from 31-Jan-2013/20:20:46.6 to 01-Feb-2013/04:32:16.9 (TAI)	
ObservationID = 0 ArrayID = 0	
Date	Timerange (TAI)
31-Jan-2013/20:20:38.5 - 20:36:12.7	1 0 3C286_0 25230 [0] [16.1]
20:41:18.7 - 20:48:17.5	2 1 1445+099_1 11310 [0] [16.1]
20:51:46.9 - 21:35:48.3	3 2 J1443+0214_0 71340 [0] [16.1]
21:36:52.7 - 21:43:35.3	4 1 1445+099_1 10875 [0] [16.1]
21:47:04.7 - 22:31:06.1	5 2 J1443+0214_0 71340 [0] [16.1]
22:32:10.6 - 22:38:53.2	6 1 1445+099_1 10875 [0] [16.1]
22:42:38.7 - 23:26:24.0	7 2 J1443+0214_0 70905 [0] [16.1]
23:27:44.5 - 23:34:27.2	8 1 1445+099_1 10875 [0] [16.1]
23:38:12.7 - 00:21:57.9	9 2 J1443+0214_0 70905 [0] [16.1]
01-Feb-2013/00:23:18.5 - 00:30:01.1	10 1 1445+099_1 10875 [0] [16.1]
00:33:46.6 - 01:17:31.9	11 2 J1443+0214_0 70905 [0] [16.1]
01:18:52.5 - 01:25:35.1	12 1 1445+099_1 10875 [0] [16.1]
01:29:04.5 - 02:13:05.9	13 2 J1443+0214_0 71340 [0] [16.1]
02:14:10.3 - 02:21:09.1	14 1 1445+099_1 11310 [0] [16.1]
02:24:22.4 - 03:08:23.8	15 2 J1443+0214_0 71340 [0] [16.1]
03:09:28.2 - 03:16:10.8	16 1 1445+099_1 10875 [0] [16.1]
03:19:40.2 - 04:07:11.0	17 2 J1443+0214_0 76995 [0] [16.1]
04:08:31.5 - 04:15:46.4	18 1 1445+099_1 11745 [0] [16.1]
04:17:55.3 - 04:32:25.0	19 0 3C286_0 23490 [0] [16.1]
(nRows = Total number of rows per scan)	
Fields: 3	
ID	Code Name RA Decl Epoch SrcId nRows
0	3C286_0 13:31:08.279845 +30.30.32.90104 J2000 0 48720
1	C 1445+099_1 14:45:16.469838 +09.58.36.10086 J2000 1 99615
2	J1443+0214_0 14:43:04.539831 +02.14.19.26087 J2000 2 575070
Spectral Windows: (1 unique spectral windows and 1 unique polarization setups)	
SpwID	Name #Chans Frame Ch1(MHz) ChanWid(kHz) TotBW(kHz) Corrs
0	none 512 TOPO 1212.837 8.138 4166.7 RR LL
Sources: 3	
ID	Name SpwID RestFreq(MHz) SysVel(km/s)
0	3C286_0 0 1212.83328 0
1	1445+099_1 0 1212.83328 0
2	J1443+0214_0 0 1212.83328 0

Figure 4.2: The `listobs` output showing the scan summary, source coordinates and frequency set-up for OH observations. The target SDSS J1443+0214 is referred to as Field ID 2.

In the `listobs` output (Fig. 4.2), one can see that the observing frequency has now been changed to cover the OH main lines.

2. **Inspecting and flagging 3C286 visibilities:** In the next step, we identify bad data on 3C286. For this purpose we choose channel 100 which is far away from the band centre i.e. likely to be free from line

emission/absorption. We use task `plotms` to plot the visibilities of 3C286 for channel 100. The output is shown in Fig. 4.3, where we plot the amplitude and phase as a function of uv-distance.

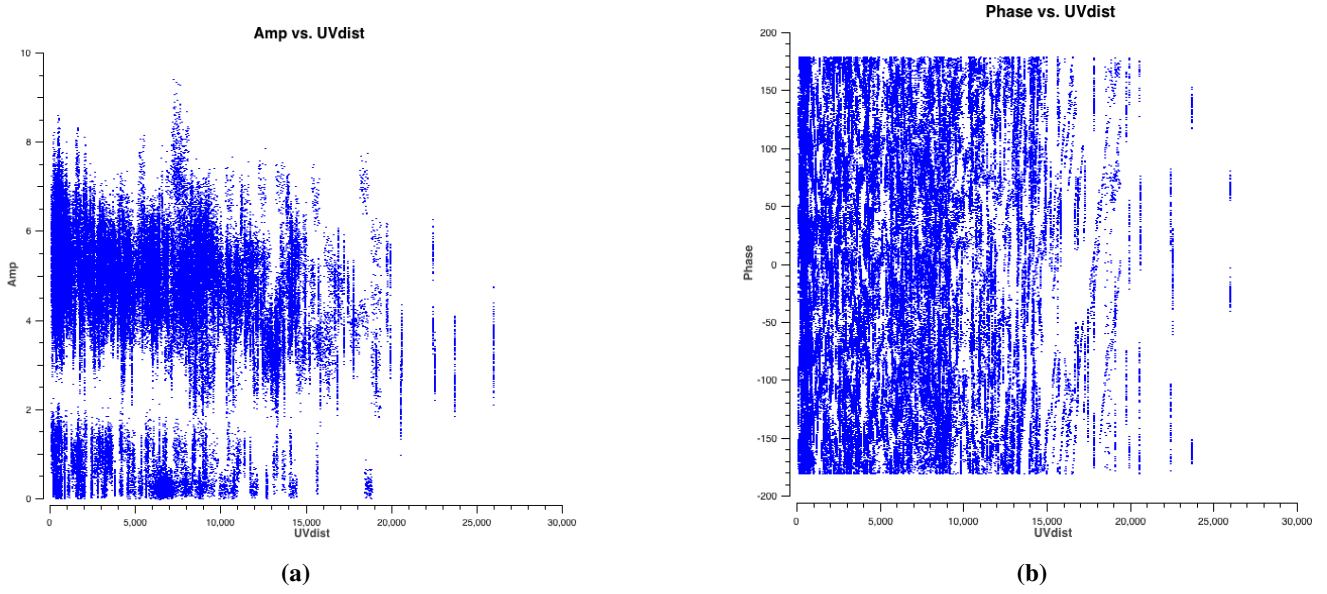


Figure 4.3: Amplitude and Phase vs uv-distance for 3C286.

The data plotted in Fig. 4.3 are uncalibrated. We notice that the amplitudes for several baselines are close to zero. These may be coming from antennas not working during the observations. We identify that these data are corresponding to four bad antennas, C09, C12, W02 and W05. Plotting individual baselines for these antennas shows that the phases with respect to time are totally random. This further confirms that the antennas are not working and the amplitudes are not low because of the low gains of the antennas.

We use task `flagdata` to flag the antennas, C09, C12, W02 and W05 for all sources and all times. However, we also noticed that antennas, C06, S06 and E05 have bad band-shapes showing spikes and the phases for individual baselines for these antennas with respect to time are also totally random. We use task `flagdata` to flag these antennas as well. The data after flagging are shown in Fig. 4.4. Most of the low amplitude visibilities have been accounted for.

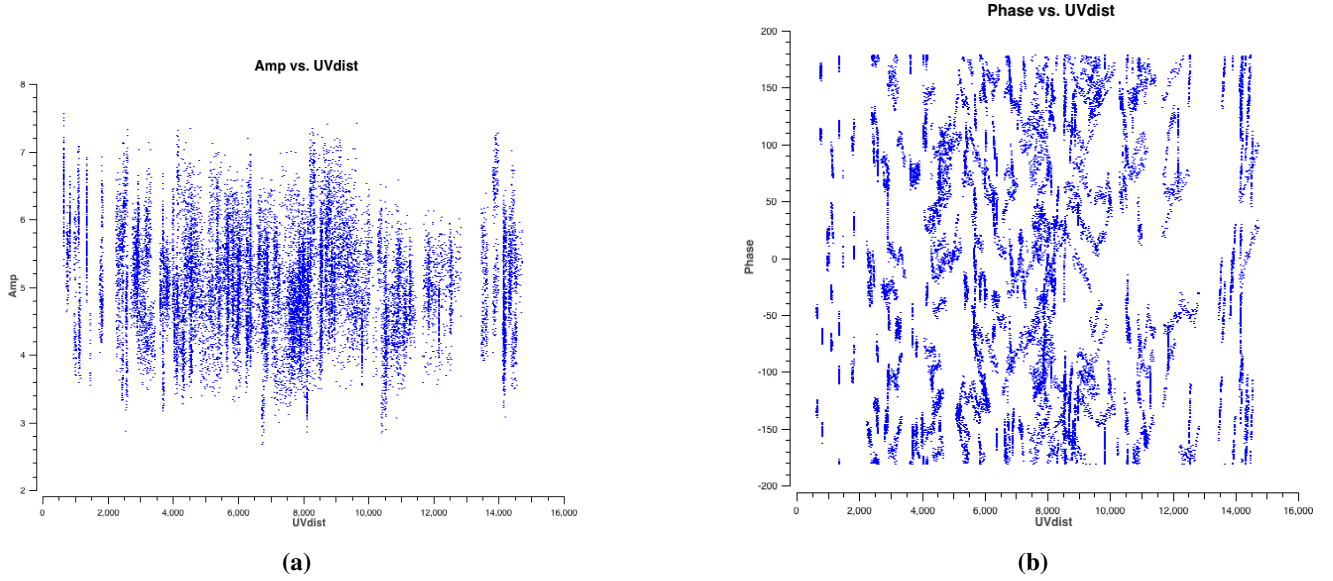


Figure 4.4: Amplitude and Phase vs uv-distance for 3C286, after initial inspection and flagging of the data.

3. **Obtaining the model of 3C286:** In this step, we use task `setjy` to fill the model visibility column for 3C286 with amplitudes and phases corresponding to the source model at the observing frequency. We choose the fluxscale to be `standard = 'Perley-Butler 2010'` and set `fluxdensity = -1`, which allows us to choose the default standard values. `Setjy` produces the output in the logger, from which one can see that it has identified the calibrator source 3C286 and filled in the know flux density of 15.857 Jy for stokes I. The flux density of 3C286 is slightly different from the one obtained in the previous chapter because we are observing at a different frequency, `RestFreq = 1212.83328` MHz.
4. **Choosing the reference antenna:** In our analysis we will use antenna C00 as the reference antenna (see Fig. 3.2). The behaviour of this antenna was also checked and found to be good during initial inspection.
5. **Solving for antenna based gains for 3C286:** We use task `gaincal` to solve for antenna based amplitudes and phases for 3C286. We set the parameter `spw = 0:100` to select the data for channel 100 and `calmode = ap` to specify amplitude and phase calibration. We set `solint = 1 min`. The table produced by the task `gaincal` is then applied to the flux calibrator using task `applycal` to check if the flagging and calibration are well done. As before we use task `plotms` for inspection. But this time we set the input parameter `datacolumn = corrected` instead of `data`. The calibrated data plotted this way are shown in Fig. 4.5. Clearly the amplitudes and phases are as expected for a standard flux density calibrator.

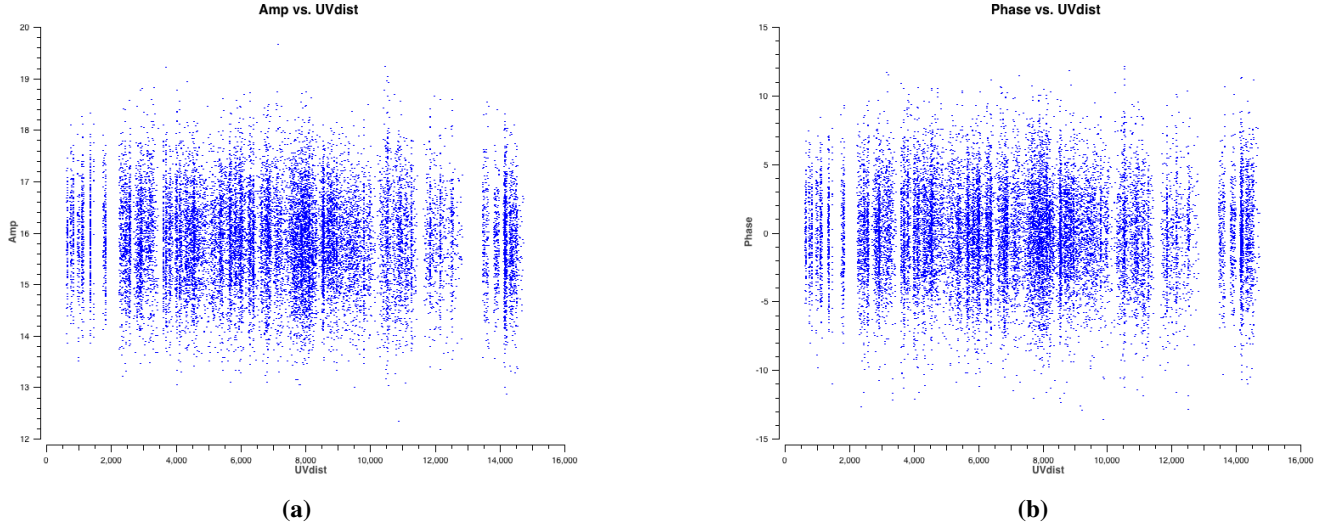


Figure 4.5: Amplitude and Phase vs uv-distance for 3C286, after flagging and calibration.

6. **3C286 RFI inspection:** In this step, we use `viewer` to plot the data for each baseline as raster plot with x-axis as frequency channel and y-axis as time. Fig. 4.6 on the left panel, show the calibrated visibilities for a baseline (E03 - E04). The visibilities affected by RFI appear as a black horizontal stripe (this is true for RFI appearing at a particular time). To flag these, we use the mouse to draw a region around the corrupted visibilities and double click in that region. This region (blue) in Fig. 4.6 (on the right panel) shows the flagged visibilities. This data is strongly affected by RFI, especially channels 266 and 430. Like this we examine all the baselines to identify and flag RFI affected data.

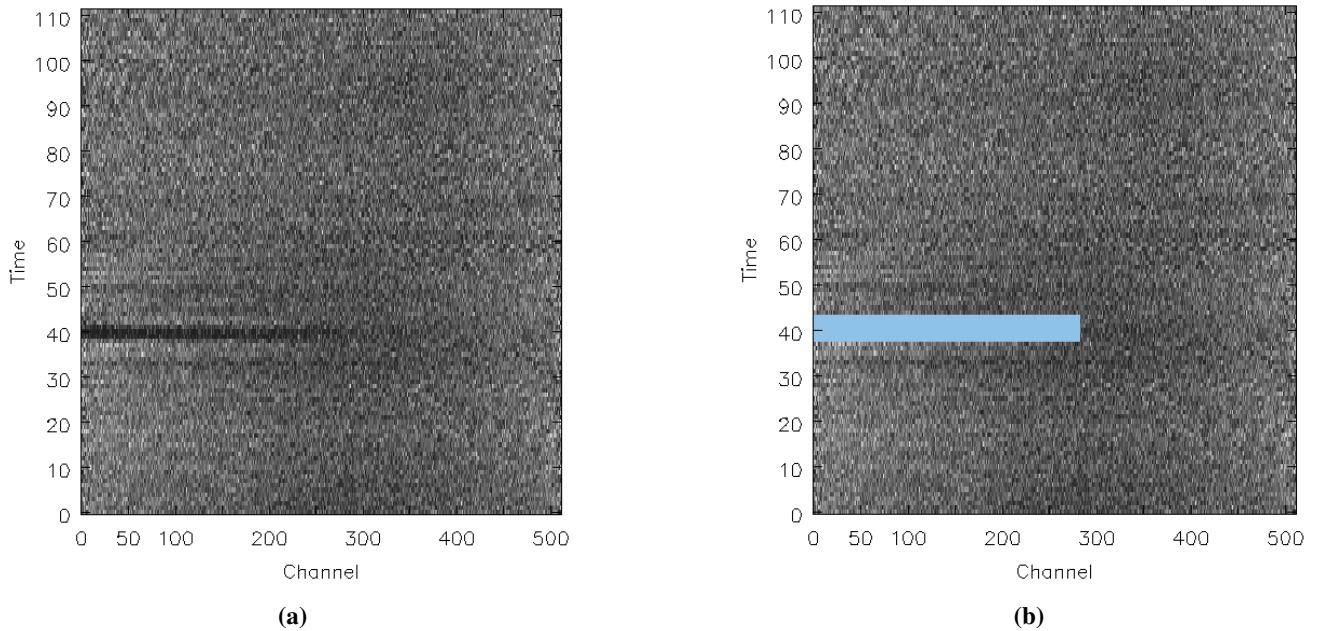


Figure 4.6: RFI inspection for 3C286 calibrated visibilities. (a) Unflagged RFI appear as a black horizontal stripe, (b) Flagged data is marked in blue.

7. **Determining bandpass calibration:** After successfully determining gains as a function of time for 3C286 and flagging RFI affected visibilities, the next step is to determine gains as a function of frequency. This is done using the task `bandpass`. We set the input `solint = inf` i.e. doing so, will derive one bandpass solution for the entire 3C286 scan. We also use `combine = scan`. During bandpass calibration, we apply the calibration table obtained when we performed task `gaincal` on-the-fly with the parameter `gaintable`. This allows us to average 3C286 over the entire scans without losing the signal-to-noise ratio. Bandpass calibration builds a table with the amplitude and phase as a function of frequency for each spectral window containing more than one channel. Typically, solutions (e.g. for a perfect bandpass) are near unity for the central channels and decrease near the edges. The bandpass solutions for seven of the GMRT antennas are shown in Fig. 4.7.

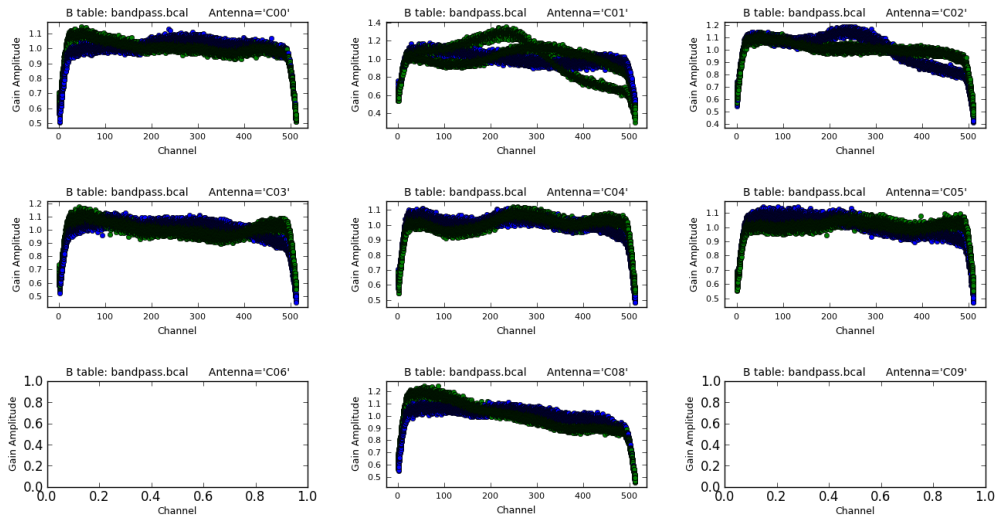


Figure 4.7: Bandpass solution for seven GMRT antennas. The different colours represent different polarizations. Antenna C06 and C09 were affected by RFI and were removed.

8. **Solving for antenna based gains for J1445+099:** We choose J1445+099 to be the phase calibrator because it is within 7.08° from SDSS J1443+0214. This source was inspected following the same procedure as in the flux calibrator. We use task `gaincal` to solve for antenna based amplitudes and phases for J1445+099. We set the parameters `spw = 0:100`, `solint = 1 min` and `calmode = ap` as before. But for this step, we apply the bandpass solutions on-the-fly, specified in `gaintable` input parameter, and we use `field = 0, 1`. This task generates a second `gaincal` table.
9. **Fluxscale:** The next step is to set the flux density scale using task `fluxscale`. For this, use the flux calibrator whose flux density was set in `set_jy` to derive the flux density of J1445+099. For this step, we apply the table produced in step (8) on-the-fly. After using task `fluxscale` we get that the flux density of our phase calibrator J1445+099 to be 2.59 ± 0.02 Jy. The flux density for J1445+099 is almost the same as the one obtained in the previous chapter, which was 2.57 ± 0.02 Jy.

To check whether or not the calibration procedure was correct, we use task `applycal` to apply the calibration solutions to the calibrator itself (J1445+099). We apply both the `bandpass` and `gaincal` tables that have been generated in the previous sections. The calibrated data are shown in Fig. 4.8. We stress that for a point-like source amplitude should be flat (and without any ripples) and the phase should be flat and centred at 0 degrees.

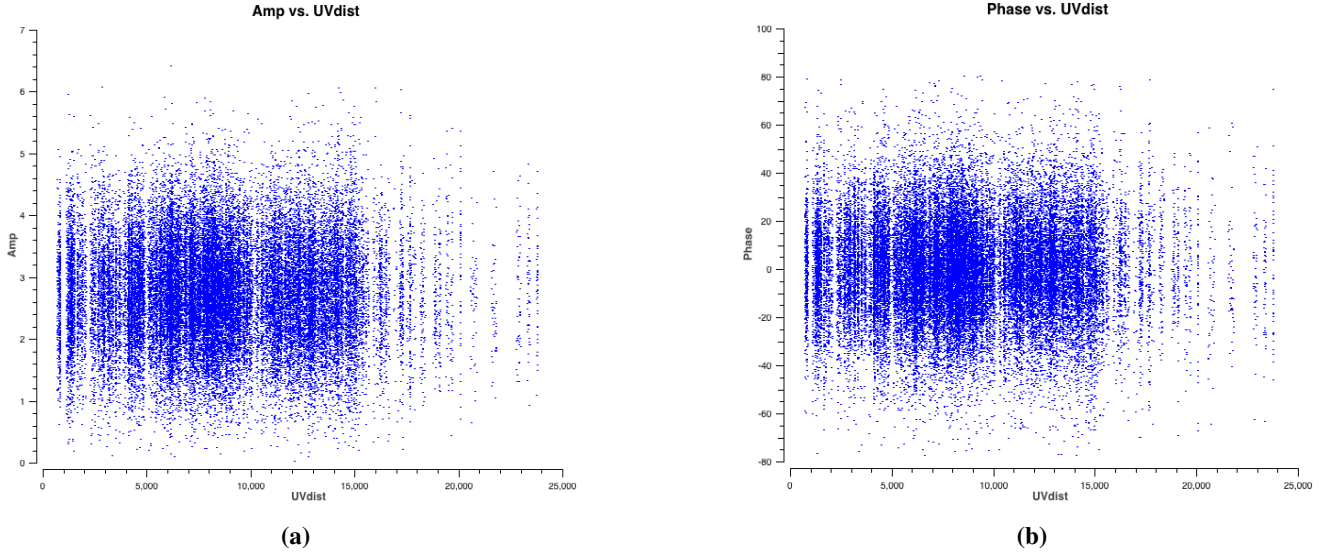


Figure 4.8: Amplitude and Phase vs uv-distance for phase calibrator, after flagging and calibration.

10. **J1445+099 RFI inspection:** In this step, we use `viewer` to plot the data for each baseline as raster plots. The visibilities affected by RFI appear as darker stripes. Following the same procedure as in step (6) we examined all the baselines to identify and flag RFI affected data.

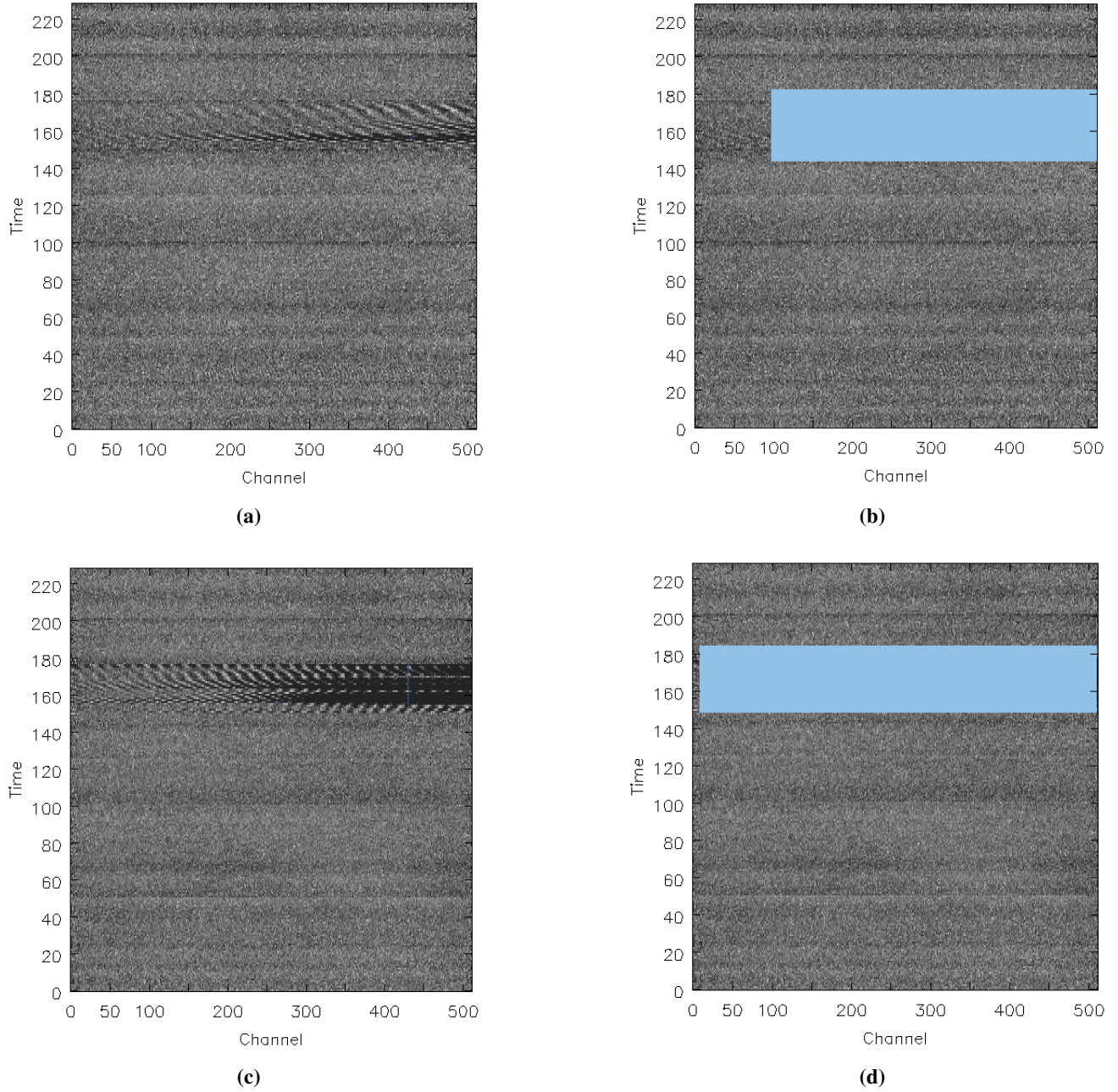


Figure 4.9: RFI inspection for J1445+099 calibrated visibilities. (a) In baseline C00 - E04 and (c) C08 - E04, the unflagged RFI appear as darker stripes. In (b) and (d) flagged data are marked in blue.

11. **Apply calibration to calibrators and target source:** In this step we use `task applycal` to interpolate the gains in time and apply the calibration tables i.e. both gains as a function of time and frequency, to the calibrators and the target source. We do this by setting the `gainfield` and `gaintable` parameters appropriately. RFI inspection was performed on the target source after applying the calibration, see Fig. 4.10.

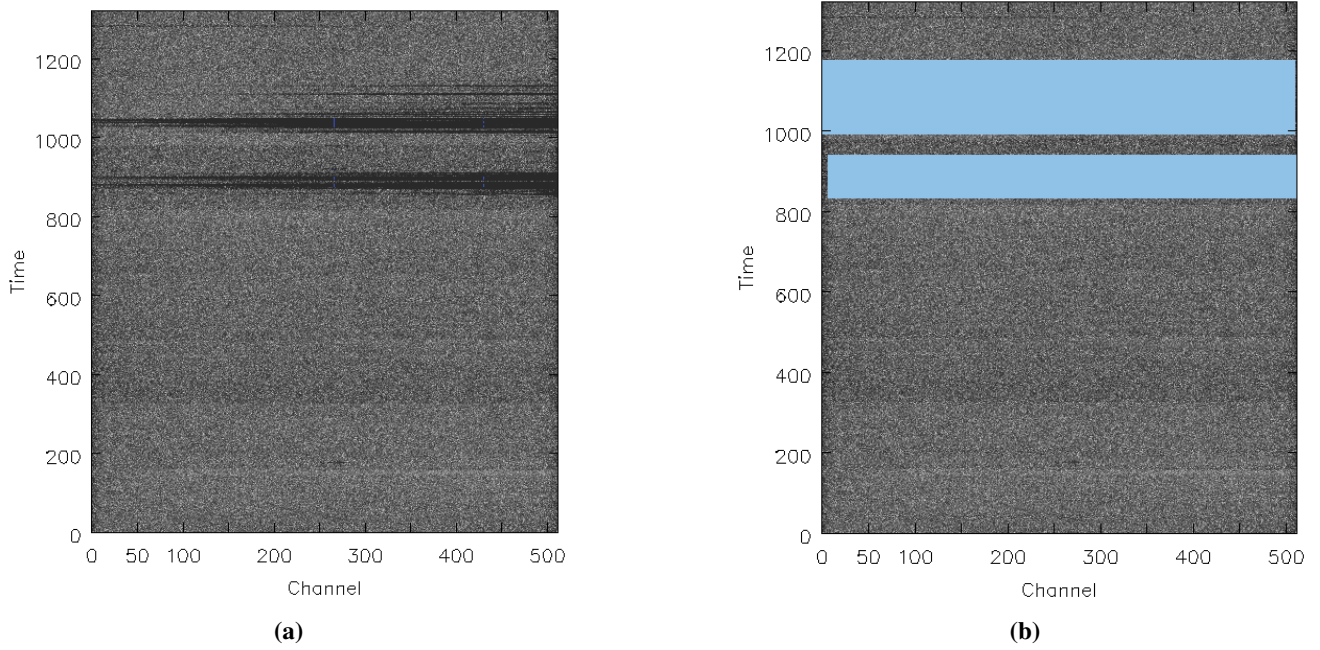


Figure 4.10: RFI inspection for SDSS J1443+0214 calibrated visibilities. Here we only show one baseline C08 - E04.

12. **Splitting the calibrated data:** The next step is to split the calibrated data for calibrators and target source into separate files using task `split`. This speeds up the processing for subsequent steps. Any further analysis will be done on these splitted data files.
13. **Continuum imaging:** As mentioned above, the task `split` was used to separate the uv-data for each source. In this step we make a single channel map of the calibrators and the target source. This task, Fourier inverts the calibrated data for channel 100 and CLEANing is controlled interactively. We use the input parameter `mode = mfs` which makes a single multi-frequency synthesis image out of the specified channels. Input `psfmode = clark` sets the algorithm to make the synthesized beam as `clark` which is also the default choice.

The parameter `imagermode = csclean` sets the mode of the CLEAN in the visibility plane. We use the same image size and the pixel size as in the previous chapter because we are using the same array and observing at a similar frequency. Fig. 4.11 shows maps of the flux calibrator and phase calibrator, which has a flux density and rms of 15.83 Jy, ~ 8.69 mJy/beam/channel and 2.58 Jy, ~ 5.12 mJy/beam/channel respectively.

We also notice that for 3C286, the rms in Fig. 4.11 (left panel) is almost equal to that obtained in the map (rms ~ 9.33 mJy/beam/channel) of the same source (see Fig. 3.10) obtained in the last chapter. The rms of J1445+099 is two times compared to that obtained in the previous map of the same source. This is because large portions of J1445+099 data is affected by RFI and flagged.

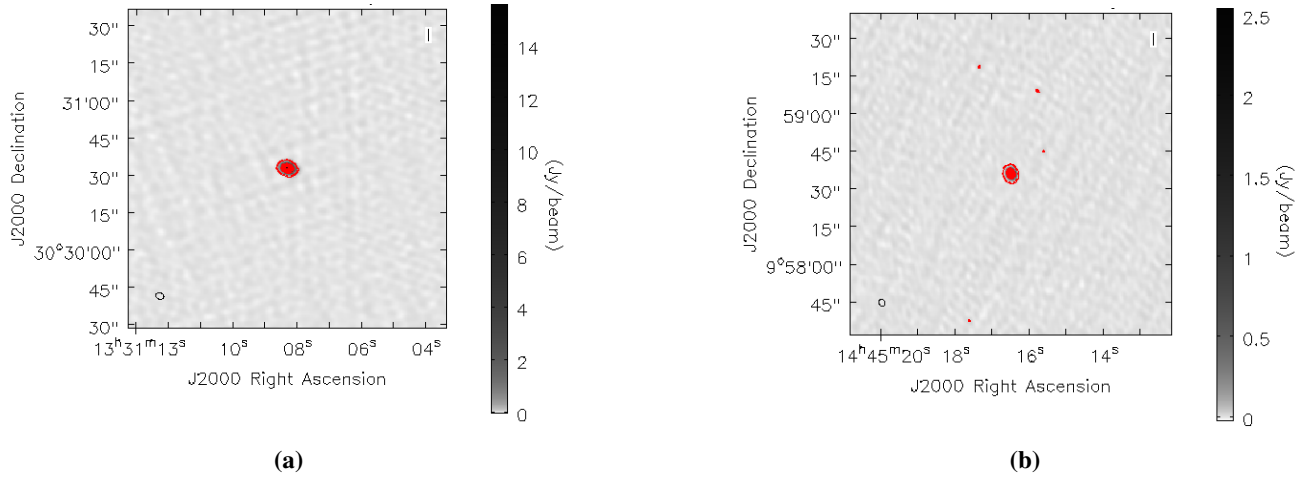


Figure 4.11: CLEAN maps of (a) 3C286 and (b) J1445+099. The contour levels start at 3σ .

14. **Self-calibration:** The next step (refer to the previous chapter) is to make an approximate model of the source via the task `clean`, averaging ~ 200 line free channels, see Fig. 4.12 (a). With a reasonable model in place, we are in a position to (self-)calibrate the science target directly. We use task `gaincal` for this purpose. The task is used both for general gain calibration using an external calibrator, and for self-calibration.

The phase self-calibration was repeated two times until the map stopped improving i.e. we checked the changes in the rms and peak flux density (results are shown in Table. 4.1). Also note that in Fig. 4.12 (c), the improvement with respect to the previous map is really marginal.

The next step is to experiment with amplitude and phase self-calibration. The solution interval used for this step is `solint = 15 min` with input `calmode = ap` specifying that we are doing amplitude and phase self-calibration. We compare the third image, Fig. 4.12 (c), and fourth image Fig. 4.12 (d). The noise level is much better, while the flux has not changed markedly. The contour levels in these images start at 3σ . Fig. 4.12 (d) is our best continuum image. The results of the self-calibration such as peak flux density and rms are given in Table. 4.1.

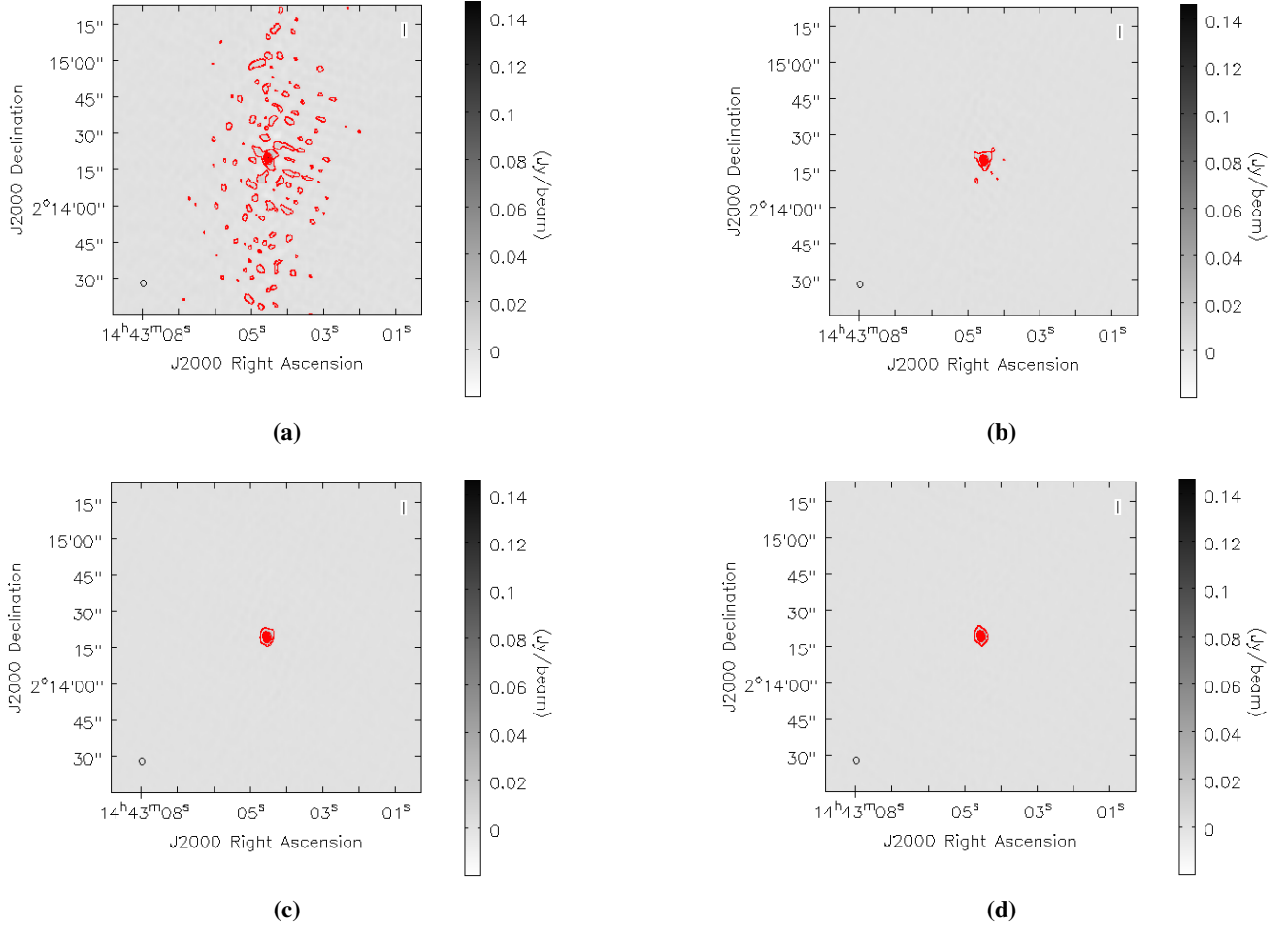


Figure 4.12: (a) Channel averaged map of SDSS J1443+0214. Continuum image of SDSS J1443+0214 after phase-only (panels b and c) and amplitude calibration (panel d). The contour levels start at 3σ .

Table 4.1: Results of self-calibration.

Model	Peak flux density [mJy/beam]	rms [mJy/beam/channel]	Figure Reference
Initial model	124.97	0.335	Fig. 4.12 panel (a)
1 phase-only	140.41	0.251	Fig. 4.12 panel (b)
2 phase-only	141.47	0.251	Fig. 4.12 panel (c)
1 amp and phase	143.25	0.245	Fig. 4.12 panel (d)

15. **Applying self-calibration solutions to line dataset:** Next step is to apply gains from the last iteration of phase-only and the amplitude-and-phase self-calibration steps to the line visibility data set. We use task `applycal` for this purpose and then split the calibrated data column.
16. **Continuum subtraction:** Next we subtract the continuum from the self-calibrated line data set obtained in step (15) using task `uvconstsub`. Like in the previous section, this task makes fits to the line free channels and subtracts the emission in the uv-domain. The task `uvconstsub` operates on the corrected

data column and writes the continuum subtracted data in a new measurement set (MS) with the extension `.contsub`.

17. **Setting velocity rest frame:** Here, we use `cvel` to correct for the Doppler shift, and at the same time, change the velocity reference frame to BARY.

Before we do that, we set the rest frequency of OH 18-cm line in the measurement set. Here we are using an MS file produced in the previous step. The rest frequency for this observation is 1666.3804 MHz i.e. this is the average frequency of the two main lines that we are interested in. We open the spectral window table of the MS using `tb.open` and insert the rest frequency using `tb.putcell`. The default rest frequency in the file is the central observing frequency. After inserting the rest frequency we close the file using `tb.close`. We also ran the task `listobs` to check that the reference frequency has been actually changed. Finally, we run task `CVEL`, with input parameter `outframe = BARY` to change the reference frame of this data set.

18. **Imaging the spectral continuum subtracted data set to obtain the image cube:** Next step is to image the line dataset obtained from the previous step. For this step, we set the input parameter `mode = channel` to produce an image with different planes. We set `threshold = 3 mJy`, telling clean to stop if the maximum residual is below this value. A dirty cube (`niter = 0`) is generated by task `clean`, after setting all the parameters and running `clean`. `Viewer` provides the animation function useful for inspecting the 3D data cube. The rms in this cube was ~ 1.7 mJy/beam/channel. This rms is a little bit higher compared to the rms we measured in a search for H I 21-cm absorption towards SDSS J1443+0214 (recall that we measured the rms of ~ 1.2 mJy/beam/channel in H I 21-cm absorption spectrum). This is most likely due to higher levels of RFI in the OH data set.

4.1.3 Results

We do not detect OH absorption towards SDSS J1443+0214. The spectrum is shown in Fig. 4.13. According to Gupta et al. (2006), “the OH column density of the absorbing gas N_{OH} (i.e. for an optically thin cloud in thermal equilibrium), is related to the excitation temperature T_x and the 1667.3590 MHz (main line) optical depth τ_{1667} by the expression”,

$$N_{OH} = 2.25 \times 10^{14} \left(\frac{T_x}{f} \right) \int \tau_{1667}(v) dv, \quad (4.1)$$

where f is the fraction of the background emission covered by the absorber. The column density, N_{OH} , is in cm^{-2} , T_x is in Kelvin and dv in km/s. However, the OH excitation temperature T_x cannot be directly estimated. So we assume $T_x = 10$ K as in Gupta et al. (2006). This is a typical temperature in dark clouds in the Milky Way. In the optically thin regime, the integrated optical depth of the line and 3σ optical depth limit on it is estimated using,

$$\int \tau_{1667}(v) dv = 1.06 \frac{3 \times \sigma_{rms}}{S_{cont}} \times FWHM_{H\,I}, \quad (4.2)$$

where σ_{rms} is the rms for the smoothed H I 21-cm spectrum, $S_{cont} = 143.25$ mJy/beam (see Table. 4.1) is the flux density of the continuum source, and $FWHM_{H\,I}$ of the detected H I 21-cm absorption line/components (see Table. 4.2). The upper limit on OH column densities for detected H I 21-cm absorption components are given in Table. 4.2.

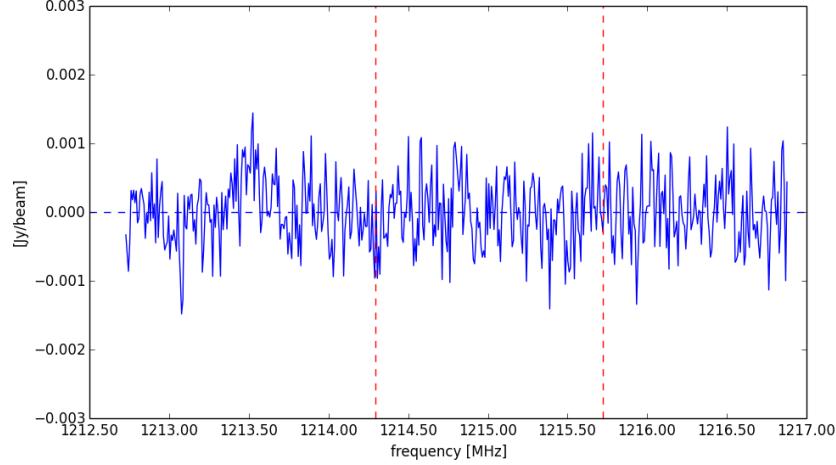


Figure 4.13: GMRT spectrum towards SDSS J1443+0214 showing OH non-detection. The vertical lines at frequency 1214.2922 MHz and 1215.7193 MHz represents the expected locations of OH main lines corresponding to $z_{abs} = 0.3715$ for the H I 21-cm absorption towards SDSS J1443+0214.

Table 4.2: OH column density limits (3σ) for the H I 21-cm absorption components presented in the previous chapter. The rms ($\sigma_{rms} = 0.7$) used here was obtained from the spectrum of H I 21-cm absorption smoothed to ~ 15 km/s (corresponding to the average FWHM of two H I 21-cm absorption components). This was done using the task `specsmooth`.

Quasar	$FWHM_{H\,I}$ (km/s)	N_{OH} (cm^{-2})
SDSS J1443+0214	9 ± 1	5×10^{14}
	20 ± 4	1×10^{15}

4.2 VLA Search for OH Absorption Towards SDSS J0849+5108

In this section, we will briefly discuss the analysis of the VLA search for OH absorption towards SDSS J0849+5108.

4.2.1 Description of VLA Observations

The Very Large Array (VLA), like GMRT, is a radio interferometer.

Astronomers from around the world, mainly, use VLA for “atmospheric/weather studies, satellite tracking, and other miscellaneous science”. The VLA “consists of 27 antennas (e.g. each antenna is 25 m in diameter) in a Y-shaped array with four configurations, arranged such that the **A** array, has a maximum antenna separation of 36 km, **B** array 10 km, **C** array 3.6 km, and **D** array 1 km” (see Fig. 4.14) (Thompson et al., 1980). Generally, the telescopes are switched between these configurations every four months or so. The antennas can be moved along rails to different positions.



Figure 4.14: Figure showing all the 27 VLA antennas. Photo reference: http://images.nrao.edu/images/VLASouth_med.jpg

The VLA telescope is very similar to the GMRT except for the operating frequencies and the fact that VLA is reconfigurable. As mentioned in the previous chapter, GMRT also has a Y-shaped configuration but consists of fixed antennas spread over 25 km. The other main difference between the two arrays is their range of operating frequencies. While VLA primarily observes above ~ 1 GHz, GMRT operates below ~ 1 GHz. They are thus complimentary.

The VLA operates at the higher frequency bands ranging from 1 GHz to 50 GHz. There are also a few lower frequency bands such as 74 MHz and 327 MHz. The antennas have receivers for seven wavelength bands, “centred near 90, 20, 6, 3.6, 2, 1.3, 0.7 cm i.e. these bands are commonly referred to as P, L, C, X, U, K and Q bands” (Thompson et al., 1980).

We used VLA L-band to search for OH main lines from $z_g = 0.3120$ towards the quasar SDSS J0849+5108, $z_q = 0.584$. As discussed by Gupta et al. (2013), “the background radio source of quasar galaxy pair (QGP) SDSS J0849+5108 has been the subject of considerable debates and there are speculations about its optical spectrum being affected by foreground galaxy lensing/or reddening”. “They also reported the detection of H I 21-cm, Na I and Ca II absorption at $z_g = 0.3120$ in the spectrum of QSO and associated these to a luminous red galaxy (LRG)” (Gupta et al., 2010). Based on the FIRST survey, “the background quasar at 1.4 GHz has a peak and the integrated flux densities of 344 mJy/beam and 350 mJy” (White et al., 1997). The deconvolved source size in the FIRST survey which has a resolution of $\sim 5''$ is $0.93'' \times 0.48''$.

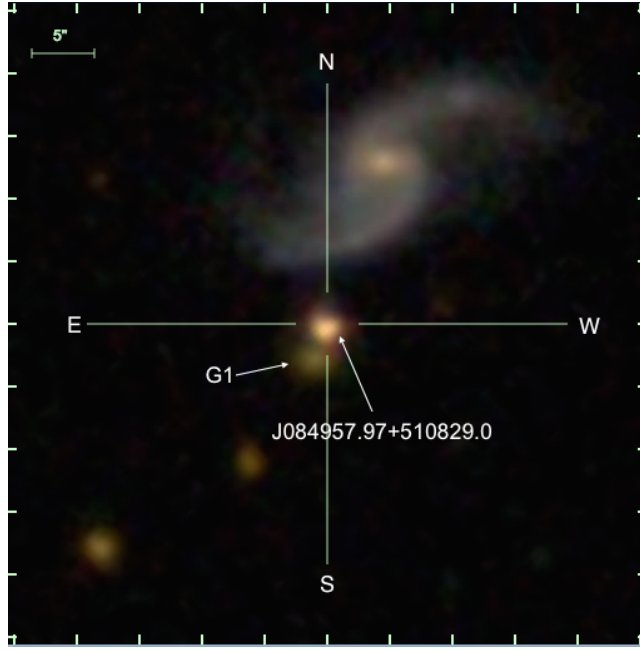


Figure 4.15: The Sloan Digital Sky Survey (SDSS) Data Release 12 image of the quasar J084957.97+510829.0. The galaxy responsible for H I 21-cm, Ca II and Na I absorption at $z_g = 0.3120$ is represented by ‘G1’.

The VLA A-array observations to search for OH were carried out in October, 2012. The A-array was chosen as it is most effective in reducing the impact of RFI. The total observing time was 4 hrs and split into two observing runs of 2 hrs that took place on the 27 and 28 October 2012. The observing strategy and set-up were exactly same for both the runs. The standard calibrator 3C147 was used for flux and bandpass calibration, and the compact radio source J0834+5534 was observed every 20 mins for about 1 min for phase calibration. The observational parameters are summarized in Fig. 4.16. We have used 0.5 MHz baseband bandwidth split into 128 frequency channels (with 16 unique spectral windows and two circular polarization channels called RR and LL) yielding a spectral resolution of ~ 0.95 km/s.

One of the main difference (apart from multiple IFs) from the previous datasets considered till now is that the data file from the two individual runs are about 100 GB i.e. an order of magnitude larger than the GMRT datasets. Otherwise, the VLA data analysis was carried out following the same strategy as adopted for the GMRT observations described in the previous sections. In the following, we will describe in broad strokes the steps carried out in the data reduction.

4.2.2 Data Analysis

The data analysis was carried out using the CASA (version 4.1.0) developed by the NRAO, using standard procedures. Most of these data were corrected out for a variety of reasons (e.g. malfunctioning antennas, radio frequency interference etc.). After editing the data, standard calibration procedures were carried out to obtain the antenna-based complex gains. Then imaging, self-calibration and spectral analysis steps were carried out.

The first step in the data reduction as usual is to obtain a summary of the measurement set (MS). We use task `listobs` for this purpose. The output is shown in Fig. 4.16. As can be seen in Fig. 4.16, the spectral windows were chosen such that to centre the sub-bands appropriately to cover the OH main lines with sufficient spectral resolution, and also to cover the maximum bandwidth to yield the good continuum sensitivity (see also Table 4.3).

Observer: Dr. Neer		Project:					
Observation: EVLA							
Data records: 41580800		Total integration time = 7144 seconds					
Observed from 27-Oct-2012/11:46:07.5 to 27-Oct-2012/13:45:11.5 (UTC)							
ObservationID = 0		ArrayID = 0					
Date	Timerange (UTC)	Scan	FldId FieldName	nRows	SpwIds	Average Interval(s)	ScanIntent
27-Oct-2012/11:46:07.0	11:46:07.0 - 11:46:32.0	1	0 J0542+4951	146000	[0, 1, 2, 3, 4, 5, 6, 7, 8, 9, 10, 11, 12,		
11:46:33.0	11:58:30.0	2	1 J0542+4951	4181440	[0, 1, 2, 3, 4, 5, 6, 7, 8, 9, 10, 11, 12,		
11:58:31.0	12:03:49.0	3	2 J0834+5534	1857120	[0, 1, 2, 3, 4, 5, 6, 7, 8, 9, 10, 11, 12,		
12:03:50.0	12:23:06.0	4	3 J0849+5108	6733520	[0, 1, 2, 3, 4, 5, 6, 7, 8, 9, 10, 11, 12,		
12:23:07.0	12:24:05.0	5	2 J0834+5534	338720	[0, 1, 2, 3, 4, 5, 6, 7, 8, 9, 10, 11, 12,		
12:24:06.0	12:43:21.0	6	3 J0849+5108	6739360	[0, 1, 2, 3, 4, 5, 6, 7, 8, 9, 10, 11, 12,		
12:43:23.0	12:44:22.0	7	2 J0834+5534	344560	[0, 1, 2, 3, 4, 5, 6, 7, 8, 9, 10, 11, 12,		
12:44:23.0	13:03:38.0	8	3 J0849+5108	6733520	[0, 1, 2, 3, 4, 5, 6, 7, 8, 9, 10, 11, 12,		
13:03:40.0	13:04:39.0	9	2 J0834+5534	344560	[0, 1, 2, 3, 4, 5, 6, 7, 8, 9, 10, 11, 12,		
13:04:40.0	13:23:56.0	10	3 J0849+5108	6739360	[0, 1, 2, 3, 4, 5, 6, 7, 8, 9, 10, 11, 12,		
13:23:57.0	13:24:55.0	11	2 J0834+5534	338720	[0, 1, 2, 3, 4, 5, 6, 7, 8, 9, 10, 11, 12,		
13:24:56.0	13:44:11.0	12	3 J0849+5108	6739360	[0, 1, 2, 3, 4, 5, 6, 7, 8, 9, 10, 11, 12,		
13:44:13.0	13:45:12.0	13	2 J0834+5534	344560	[0, 1, 2, 3, 4, 5, 6, 7, 8, 9, 10, 11, 12,		
(nRows = Total number of rows per scan)							
Fields: 4							
ID	Code	Name	RA	Decl	Epoch	SrcId	nRows
0		J0542+4951	05:42:36.137916	+49.51.07.23356	J2000	0	146000
1	K	J0542+4951	05:42:36.137916	+49.51.07.23356	J2000	1	4181440
2	D	J0834+5534	08:34:54.904117	+55.34.21.07098	J2000	2	3568240
3		J0849+5108	08:49:57.970000	+51.08.29.00001	J2000	3	33685120
Spectral Windows: (16 unique spectral windows and 1 unique polarization setups)							
SpwID	Name	#Chans	Frame	Ch1(MHz)	ChanWid(kHz)	TotBW(kHz)	Corrs
0	none	128	TOPO	1227.164	3.906	500.0	RR LL
1	none	128	TOPO	1227.664	3.906	500.0	RR LL
2	none	128	TOPO	1228.164	3.906	500.0	RR LL
3	none	128	TOPO	1228.664	3.906	500.0	RR LL

Figure 4.16: The `listobs` output showing the scan summary, source coordinates and frequency set-up for the observations. The target SDSS J0849+5108 is referred to as Field ID 3. Note that this is not the complete `listobs` output. For frequency set-up see Table 4.3.

After this, as a general data editing and examination strategy, at this stage in the data reduction process, one wants to focus on the calibrators. The data reduction scheme is to determine various corrections from the calibrator sources, then apply these correction factors to the science target. In this step we inspect the flux/bandpass calibrator. We examined all the spectral windows for bad data i.e. bad antennas, baselines and RFI using the steps/tools already described. The task `set jy` was then used to fill the model visibility column for J0542+4951 with amplitudes and phases corresponding to the source model at the observing frequency. The flux densities estimated by `Set jy` for different IFs are given in Table 4.3.

Table 4.3: Frequency set-up used for VLA observations. The last column has fluxes determined by `set jy` for J0542+4951.

IF No.	Freq(GHz)	BW(kHz)	Ch.Sep(kHz)	Flux (Jy)
1	1.22741397	500.0000	3.9063	24.8759
2	1.22791397	500.0000	3.9063	24.8682
3	1.22841397	500.0000	3.9063	24.8605
4	1.22891397	500.0000	3.9063	24.8528
5	1.22941397	500.0000	3.9063	24.8451
6	1.22991397	500.0000	3.9063	24.8374
7	1.23041397	500.0000	3.9063	24.8298
8	1.23091397	500.0000	3.9063	24.8221
9	1.26843905	500.0000	3.9063	24.2595
10	1.26893905	500.0000	3.9063	24.2522
11	1.26943905	500.0000	3.9063	24.2449
12	1.26993905	500.0000	3.9063	24.2376
13	1.27043905	500.0000	3.9063	24.2303
14	1.27093905	500.0000	3.9063	24.2230
15	1.27143905	500.0000	3.9063	24.2157
16	1.27193905	500.0000	3.9063	24.2084

In the next step, we use task `gaincal` to solve for antenna based complex gains for J0542+4951 and then determine the bandpasses. In Fig. 4.17, we show the calibrated data for J0542+4951 for IF 11 with parameter `spw = 11:50`. The bandpasses for IF 11 are shown in Fig. 4.18.

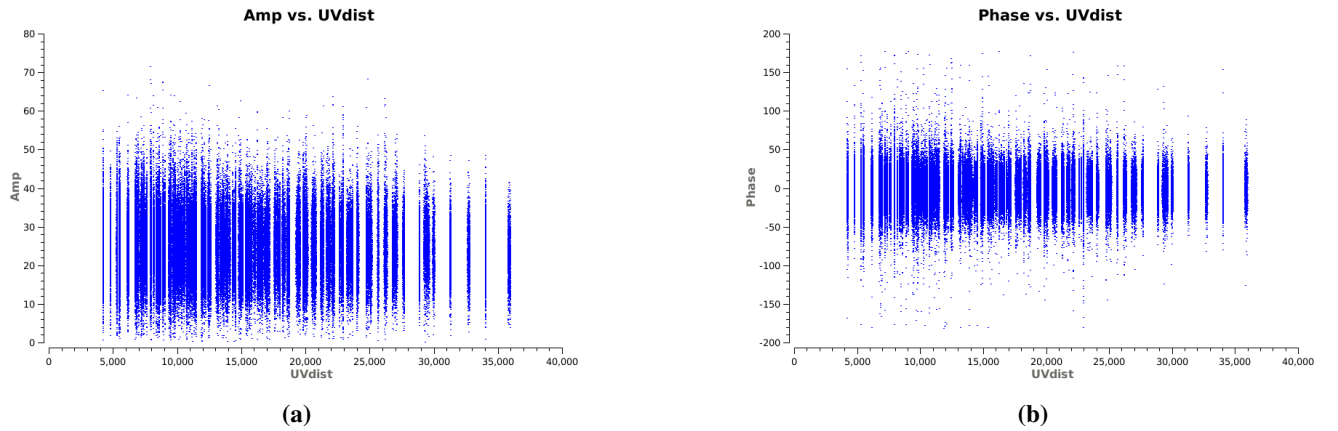


Figure 4.17: Amplitude and Phase vs uv-distance for J0542+4951 (IF 11), after flagging and calibration.

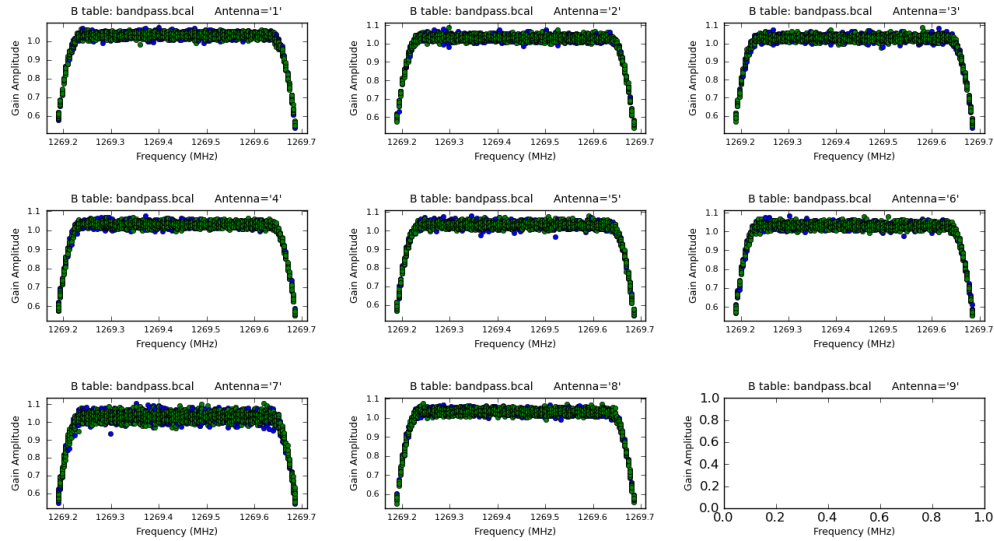


Figure 4.18: Bandpass solution for eight VLA antennas. The different colours represent different polarizations. These Bandpass solutions are for spectral window 11. Antenna 9 was affected by RFI and removed.

The next step is to use task `gaincal` to solve for antenna based amplitudes and phases for J0834+5534 for all the IFs. We set the parameters `spw = 0:50`, `solint = 1 min` and `calmode = ap`. In this step, we apply the bandpass solutions on-the-fly, specified in `gaintable` input parameter, and we use `field = 1, 2`. This task generates a second `gaincal` table.

After this we set the flux density scale using task `fluxscale`. To derive the flux density of J0542+4951, we use the flux calibrator whose flux density was set in `set jy`. From this we get the flux density of our phase calibrator J0834+5534 to be ~ 6.3 Jy.

We then applied all the calibrations to the target source and split the calibrated data. As OH main lines are in IFs 11 and 14 of the dataset, we splitted only IFs 9 to 16. All the above mentioned steps were carried out for the data from both the observing runs, and the calibrated data were combined.

In the following, we focus only on calibrated data from IFs 11 and 14. After performing all the preliminary steps, we proceed to do self-calibration. We first focus on correcting only for phase errors. For this, we perform phase-only self-calibration using the task `gaincal`. The solution interval used is `solint = 1.0 min` for phase self-calibration for both IFs 11 and IF 14. In the next step we perform amplitude and phase self-calibration. The solution interval used for this step is `solint = 8.0 min`. The self-calibrated images for IF 11 and the results are given in Fig. 4.19 and Table. 4.4, respectively. For IF 14 the results are given in Fig. 4.20 and Table. 4.5. In these images, the contour levels start at 3σ . Fig. 4.19 panel (d) and Fig. 4.20 panel (d) are our best (self)-cal images.

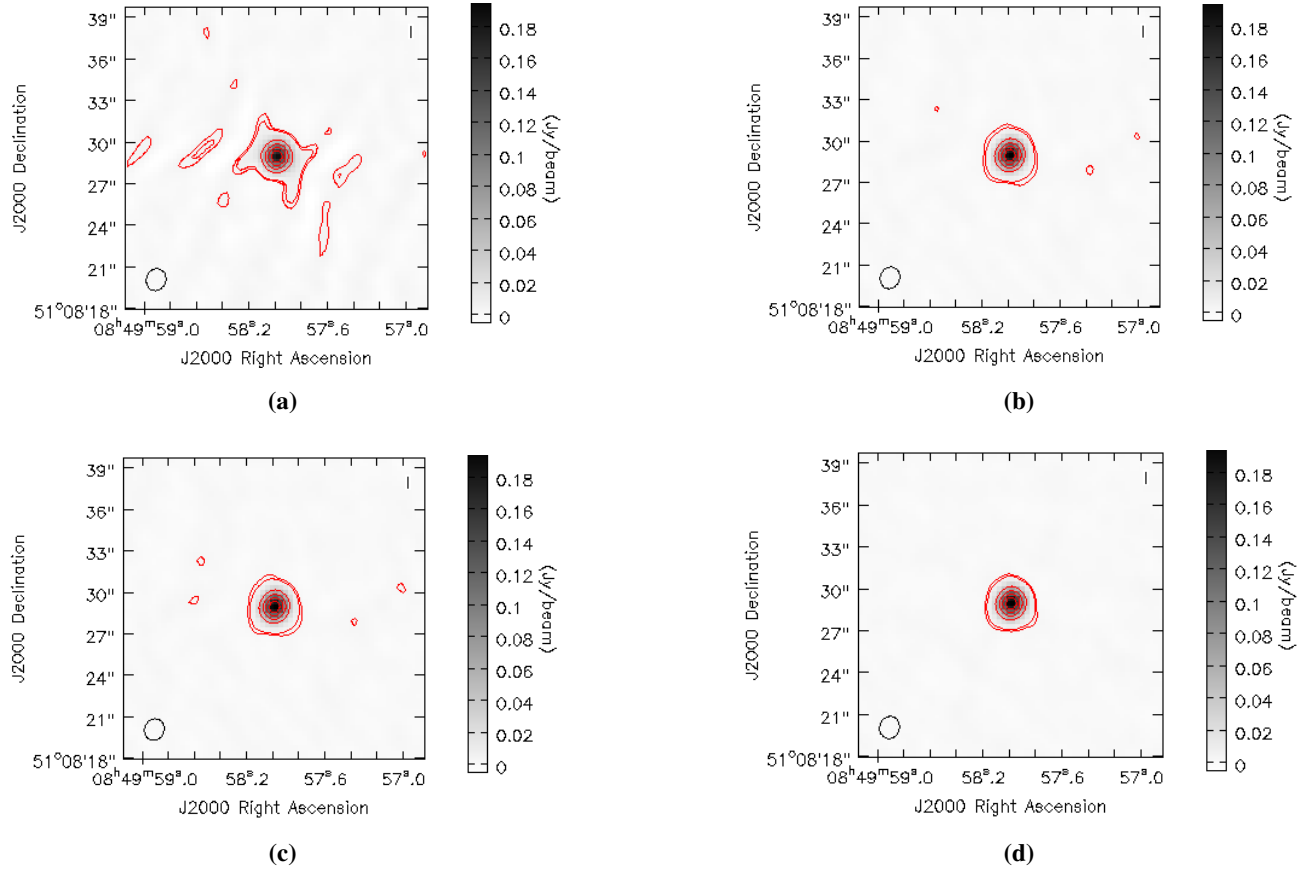


Figure 4.19: (a) Channel averaged map of SDSS J0849+5108 for IF 11. Continuum image of SDSS J0849+5108 after phase-only (panels b and c) and amplitude calibration (panel d). The contour levels start at 3σ .

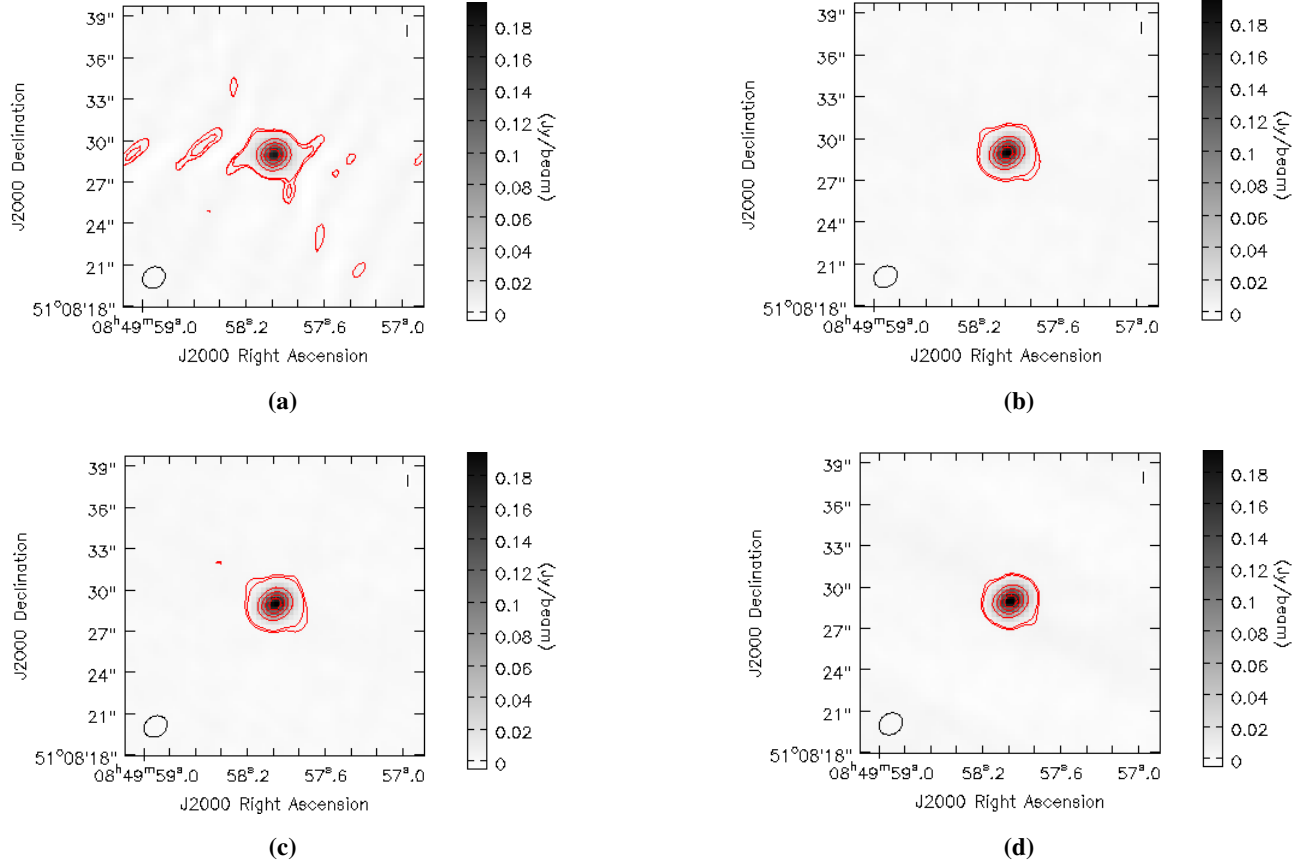


Figure 4.20: (a) Channel averaged map of SDSS J0849+5108 for IF 14. Continuum image of SDSS J0849+5108 after phase-only (panels b and c) and amplitude calibration (panel d). The contour levels start at 3σ .

From the final self-calibrated continuum image of the target from the combined dataset, we measure a flux density of ~ 208 mJy. The source is compact i.e. unresolved. We then subtracted the continuum and corrected data for the heliocentric motion of the Earth. Finally, this was imaged to get the spectral line cubes for IFs 11 and 14 that cover the two OH main lines. The spectra are shown in Fig. 4.21. The spectral rms in the unsmoothed spectra are 3.9 and 4.4 mJy/beam respectively.

Table 4.4: Results of self-calibration for IF 11.

Model	Peak flux density [mJy/beam]	rms [mJy/beam/channel]	Figure Reference
Initial model	189.1370	1.3340	Fig. 4.19 panel (a)
1 phase-only	204.3566	0.6856	Fig. 4.19 panel (b)
2 phase-only	204.8465	0.6827	Fig. 4.19 panel (c)
1 amp and phase	207.9471	0.6712	Fig. 4.19 panel (d)

Table 4.5: Results of self-calibration for IF 14.

Model	Peak flux density [mJy/beam]	rms [mJy/beam/channel]	Figure Reference
Initial model	180.6421	1.0866	Fig. 4.20 panel (a)
1 phase-only	200.6427	0.6822	Fig. 4.20 panel (b)
2 phase-only	201.7470	0.6439	Fig. 4.20 panel (c)
1 amp and phase	208.4010	0.6311	Fig. 4.20 panel (d)

4.2.3 Results

Given the redshift of the 21-cm absorption from Gupta et al. (2013), we expect the corresponding OH lines with rest frequencies of 1665.4018 and 1667.3590 MHz to occur at 1269.3611 MHz and 1270.8528 MHz, respectively. There is, however, no evidence of OH absorption in either case (see Fig. 4.21). However, Gupta et al. (2013) detected H I 21-cm absorption at $z_g = 0.3120$ and the H I 21-cm profile is resolved into three components. We used these components and the same idea as in the previous chapter to estimate the limits on OH column density. In Table. 4.6 we list the estimates of OH column density for this system obtained using eqn. (4.1). The OH filling factor f was assumed to be unity for these calculations.

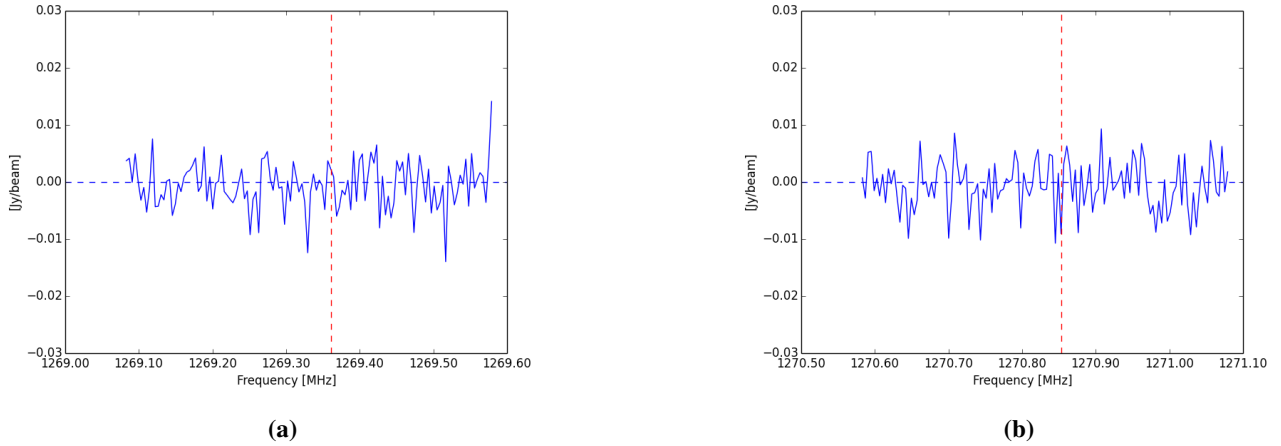


Figure 4.21: GMRT spectra towards SDSS J0849+5108 showing OH non-detection for two main lines, (a) and (b). The vertical dashed lines at (a) 1269.3612 MHz and (b) 1270.8530 MHz, represent the expected locations of OH main lines corresponding to $z_g = 0.3120$ from the H I 21-cm absorption towards SDSS J0849+5108.

Table 4.6: OH column density limits (3σ) for the H I 21-cm absorption components presented in Gupta et al. (2013). The rms used here for IF 11 and IF 14 (smoothed to 10 km/s) is $\sigma_{rms} = 1.2$ mJy/beam/channel and $\sigma_{rms} = 1.4$ mJy/beam/channel, respectively (Fig. 4.21).

Quasar	$FWHM_{H\,I}$ (km/s)	N_{OH} (cm^{-2})
J0849+5108	4 ± 1	1.8×10^{14}
	13 ± 2	5.9×10^{14}
	8 ± 2	3.6×10^{14}

4.3 Conclusion

Liszt & Lucas (1999) has suggested that OH is a good tracer of molecular hydrogen H_2 (e.g. H_2 has no permanent dipole and no radio emission), under a variety of physical conditions. Since it is difficult to directly detect H_2 , its column density, is usually inferred from observations of other species referred to as tracers of H_2 (e.g. Combes & Pineau des Forêts, 1999). “The OH column density is known to correlate with the visual extinction A_V and, hence, with the total hydrogen column density, N_{H_2} ” (Crutcher, 1979). In this project we have carried out a search for redshifted OH absorption in two sight-lines i.e. towards SDSS J1443+0214 and SDSS J0849+5108.

Despite the detection of H I 21-cm absorption and signature of reddening due to dust, we do not detect OH absorption to the levels of 10^{15} cm^{-2} in both the cases. Given that the level of extinction is not very high, it is quite likely that these sight lines are (at best) tracing diffuse or translucent molecular gas. In that case, our column density limits are about an order of magnitude poorer. This is generally true for molecular absorption line searches in the literature.

Our datasets were highly affected by radio frequency interference (RFI). This signal can result in a negative effect on discovering new systems, especially systems with low column densities. Constant presence of RFI can hide new line detections as well as disguise lines. As long as RFI is present in low-frequency spectra observations there will be certain redshift bins in which H I 21-cm or OH absorption lines cannot be detected due to irremovable RFI, which will negatively effect discoveries of new systems.

Although new detections are always the preferred outcome, the lack of new detections does not necessarily correlate to a lack of results. We are still able to derive the column density for OH in both cases. When we estimate the column densities of our objects we need to bear in mind the uncertainties in the values of spin temperature and covering factor for the different objects. The spin temperature T_s could be greater than 100 K. If this were so, it would only increase our estimate of the column density. And the covering factor might be less than unity.

The next major improvement in this field will therefore come from the availability of MeerKAT telescope

which will be the most sensitive telescope at ~ 1 GHz and ideally suited for OH absorption lines in diffuse ISM. As MeerKAT will also be capable of doing blind H I 21-cm and OH absorption line searches it will also detect sight lines through dense molecular ISM that have been missed till now. This will also lead to a much better understanding of the global evolution of cold gas in the (e.g. $z < 1$) Universe, but will also turn up many interesting instances of galaxies at intermediate redshifts in which the ISM can be studied (Zwaan et al., 2015).

Building a Dust-unbiased Sample of Radio Loud Quasars

In the previous chapters, we presented results of H I 21-cm and hydroxyl (OH) absorption line searches from two quasar-galaxy pairs (QGP). The H I 21-cm absorption and moderate amounts of dust extinction are detected in both cases. These signatures suggest that the sight lines are passing through the cold atomic gas and the physical conditions in the gas may be favourable for the formation of molecules. However, we do not detect OH absorption in either case using GMRT/VLA.

In general, despite large efforts from the community over last three decades, most of the molecular absorption line searches till date have resulted in null detections. At present, about 50 intervening 21-cm absorbers are known at $0 < z < 3.5$. In comparison, only a handful of molecular absorbers are known.

OH and CO are the most abundant molecules that can be searched for using radio telescopes. While “CO emission is detected in bright quasi-stellar objects (QSOs)” (e.g. Omont et al., 1996) and starburst galaxies, the available radio telescopes are not sensitive enough to detect CO emission from normal galaxies beyond the local Universe. Due to the same reasons i.e. lack of suitable strong sources at mm-wavelengths, the extragalactic CO absorption at mm-wavelengths, besides two low- z active galactic nucleus (AGNs), has only been detected in four sources. This scenario at mm-wavelengths is expected to change with the “Atacama Large Millimeter/submillimeter Array” (ALMA) and other upcoming facilities (Carilli & Blain, 2002). Similarly, 18-cm OH mega-maser emission has been reported from starburst galaxies (Darling & Giovanelli, 2002). However, at $z \geq 0.1$ only five OH molecular absorption systems are known to date; in two of these cases absorbing gas is associated with the AGN itself, and in the remaining three cases absorption arises from the intervening lensing galaxy (e.g. Darling, 2004; Kanekar et al., 2004).

The scarcity of molecular absorption line detections at radio wavelengths is due to the following two reasons:

1. **Small size/covering factor of molecular clouds:** Compared to the diffuse atomic gas which is most commonly detected in absorption line surveys, the molecular gas clouds have much smaller volume filling factor in ISM. Due to the smaller absorption cross-section, the probability to detect these clouds is much smaller.
2. **Limitations of current radio telescopes:** The instantaneous bandwidths offered by the current radio telescopes have been too small. In addition, large fraction of frequency ranges have been affected by the radio frequency interference (RFI). As a result large blind surveys of absorption lines have not been possible. Instead, H I 21-cm or OH absorption line searches of sight lines selected based on the presence of Mg II absorber or DLAs from optical surveys have been carried out. Since molecular gas is accompanied by dust, the sight lines passing through molecular ISM are expected to be missed out in optical surveys, and therefore, searches based on optical surveys are not ideal for detecting molecular ISM.

Due to these reasons, although radio absorption line searches, till date, have provided valuable constraints on the evolution of diffuse atomic gas in galaxies, they haven't really been helpful in detecting reservoirs of molecular gas (Gupta et al., 2012). Therefore, a large blind absorption line survey (e.g. the MeerKAT Absorption Line Survey) at radio wavelengths can overcome these limitations, and provide an unbiased view of the cold atomic and molecular gas in galaxies.

The MeerKAT Absorption Line Survey (MALS) will use the excellent sensitivity and large instantaneous bandwidth of MeerKAT to carry out the first sensitive search of atomic and molecular gas in the ISM at $z < 1.5$. The main strategy is to observe radio-loud quasars (RLQs) i.e. brighter than 200 mJy (at ~ 1 GHz). This will allow the survey to obtain 5σ sensitivity to detect 100 K atomic gas in subDLAs ($N(\text{HI}) > 10^{19} \text{ cm}^{-2}$) over $0 < z < 1.5$ in < 2 hrs of integration. It is important that the target RLQs for MALS are selected in a dust-unbiased way.

Therefore, through the MALS collaboration, we are carrying out an ambitious program to build a purely infrared selected sample of ~ 600 radio loud quasars (RLQs; 200 mJy at 1 GHz) at $z > 1.5$ ¹. These RLQs candidates are well-suited for both, (i) studying various AGN related issues at the main epoch of galaxy formation and AGN evolution, and (ii) follow-up in radio, which is also unaffected by the dust extinction, to search for intervening H I 21-cm and OH absorption lines using MeerKAT radio telescope to constrain the evolution of cold ISM in galaxies at $z < 1.5$. The sample of Infrared (IR) selected RLQs and intervening absorbers discovered through this program will be the largest to-date.

In this chapter, we briefly discuss the details of observations and analysis of a sample of 16 targets observed with the Southern African Large Telescope (SALT) to test the target selection and observing strategy.

¹The redshift and flux density cut are motivated by MALS. As MeerKAT Ultra high frequency (UHF) band can observe H I 21-cm absorption at $z < 1.5$, observations of $z > 1.5$ quasars is required to maximize the redshift path of the survey. The flux density of > 200 mJy will allow the survey to reach desired optical depth sensitivities in < 2 hrs of observing time per target.

5.1 Target Selection for the Pilot Project with SALT

In this section we are going to give a brief overview of four astronomical surveys and then give a summary of how they were used for target selection.

1. The NRAO VLA Sky Survey (NVSS) is a “1.4 GHz ($\sim \lambda = 20\text{-cm}$) continuum survey covering the entire sky north of J2000.0” $\delta = -40^\circ$ declination (82% of the celestial sphere) (Condon et al., 1998) i.e. covering the total area of $\sim 33,700 \text{ deg}^2$. This survey produced images with a “full width at half-maximum (FWHM) resolution of $45''$ and a limiting peak source brightness of about 2.5 mJy/beam” (Condon et al., 1998). The rms uncertainties in right ascension and declination vary from $\leq 1''$ for sources stronger than 15 mJy to $7''$ at the survey limit.
2. The Catalina Real-Time Transient Survey (CRTS) is a synoptic sky survey that utilizes data taken by the “three wide-field telescopes in Arizona and Australia, covering the total area of $\sim 30,000 \text{ deg}^2$ ” in order to discover rare and interesting transient phenomena. According to Drake et al. (2014), the “three telescopes repeatedly survey the sky between declination $\delta = -75^\circ$ and $+65^\circ$ ”. The limiting magnitudes are $\sim 20 - 21$ mag per exposure. With time baselines from 10 mins to 6 years (Djorgovski et al., 2011). The “basic goal of CRTS is a systematic exploration and characterization of the faint, variable sky” (Drake et al., 2014). However, “each of the telescope is ran as a separate sub-survey”. These telescopes consist of the “Catalina Schmidt Survey (CSS), the Mount Lemmon Survey (MLS) and the Siding Spring Survey (SSS)”. Each telescope has a “ $4k \times 4k$ CCD camera, which for the CSS, MLS and SSS cover $8.2, 1.1$ and 4 deg^2 ”, respectively (Drake et al., 2014).
3. The Sydney University Molonglo SKy Survey (SUMSS) is a “radio imaging survey at 843 MHz of the whole sky south of declination -30° covering the total area of $\sim 8,000 \text{ deg}^2$ ”. “With a resolution of $43''$ and an rms noise level of $\sim 1 \text{ mJy/beam}$ ”. The SUMSS has a “similar sensitivity and resolution to the NVSS” (Sadler & Hunstead, 2002).
4. The “Wide-field Infrared Survey Explorer (WISE) uses a 40 cm telescope feeding arrays with a total of 4 million pixels. WISE is achieving a sensitivity more than 100 times better than InfraRed Astronomical Satellite (IRAS) in the $12 \mu\text{m}$ band” (Wright et al., 2010).

The number density of radio sources ($>200 \text{ mJy}$) with their optical counterparts are very sparsely identified in the Southern hemisphere. We use IR colours from AllWISE catalogue to identify $z > 1.5$ RLQ candidates. The AllWISE catalogue provides all sky W1 ($3.4\mu\text{m}$), W2 ($4.6\mu\text{m}$), W3 ($12\mu\text{m}$) and W4 ($22\mu\text{m}$) photometry. We cross-correlate all the sources brighter than 200 mJy at declination $< +20$ degrees from NVSS/SUMSS with the AllWISE catalogue and identify ~ 8500 radio sources with counterparts within 3 arcsec. In Fig. 5.1, we plot the distribution of W2-W3 and W1-W2 colours for these in Cyan. The radio sources identified as

galaxies (all are at $z < 1$) and quasars in the literature are plotted as filled black and coloured circles respectively. We searched for the best criterion to separate $z > 1.5$ quasars from the rest and find that the $(W1-W2) < 1.3(W2-W3) - 3.04$ and $W1-W2 > 0.6$ maximises ($\sim 75\%$ efficiency) the $z > 1.5$ quasar fraction. Using this criterion (dashed lines in Fig. 5.1), we identify ~ 1500 radio sources that are unresolved in NVSS/SUMSS, and also detected in CRTS. Overall, we have about [450, 850, 200] RLQ candidates in the magnitude bins of $[V < 20, 20 < V < 22 \text{ and } V > 22]$. Note that the CRTS criterion is only imposed to increase the likelihood of obtaining a good SNR spectrum with the chosen telescope, and the candidate selection is purely IR-based.

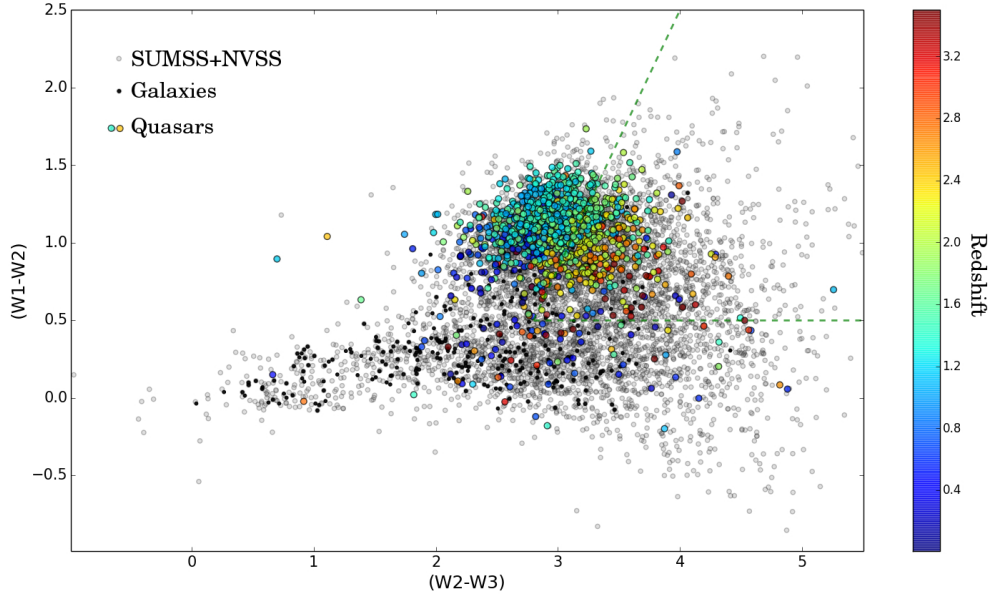


Figure 5.1: WISE colour-colour plot for radio sources ($\delta < +20^\circ$, > 200 mJy) with WISE counterparts (Cyan). Radio galaxies and quasars are shown as black and coloured circles respectively.

For the pilot project with SALT we selected 16 targets with $V < 22$ from the parent sample of 1500 candidates (PI: N. Gupta; Program ID: 2014-2-SCI-027). Here, we present results from the SALT Robert Stobie Spectrograph (RSS) observations of this sample.

5.2 Description of SALT Observations

With a 10-metre diameter, the Southern African Large Telescope (SALT) is the largest single optical telescope in the Southern hemisphere and it is designed mainly for spectroscopy. The segment design consists of a spherical primary mirror mosaic of 91 separated but identical 1 m wide hexagons. The SALT primary mirror is mounted at a fixed altitude of 37° from the vertical and can move in azimuth for target acquisition. By moving the instrument payload at the primary focus, astronomical objects can be tracked i.e. the payload tracker has a range of $\pm 6^\circ$ (Smith et al., 2006). The spherical aberration corrector (SAC) mounted concentric to and 13.08 m (half the radius of curvature) away from the primary mirror, has a circular 8 arc-minute field of view over a declination range of -75° to $+10^\circ$ and feeds the prime focus with an F/4.2 beam.

SALT has a fixed elevation and therefore observing with it is more difficult than observing with most ground-based telescopes. SALT can rotate through 540° in azimuth. Astronomical objects are “traced as the earth rotates without adjusting the azimuth angle for a period of up to two hours i.e. using a tracker, which moves across the mirror on a virtual spherical focus” (Smith et al., 2006). Hence, this gives the telescope an annulus-shaped observing area in the sky (see Fig. 5.2).

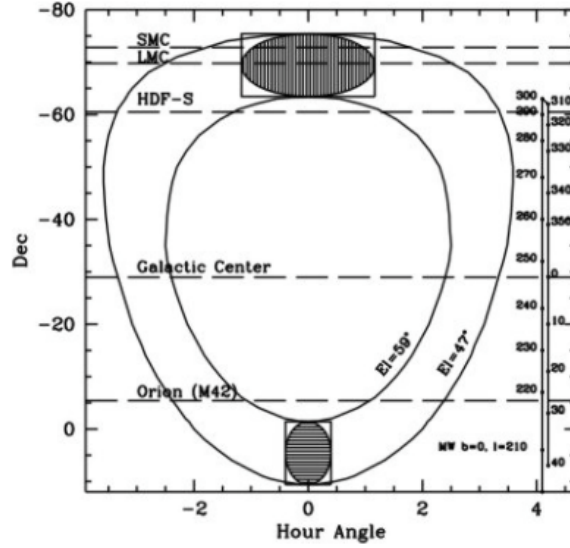


Figure 5.2: Visibility annulus of objects observable with SALT as a function of declination and hour angle, and the hashed area shows the range of motion for the tracker at two different declinations. Photo reference: <http://www.sal.wisc.edu/PFIS/docs/rss-vis/ebb/pfis/observer/intro.html#SALT>

The objective of our observations, was to obtain the low-resolution spectra of 16 high- z quasar candidates. The Robert Stobie Spectrograph (RSS) with $2''$ slit and grating pg0900 (low resolution) covering 4500 - 7500 Å were used for this purpose. This results in a resolution of ~ 4 Å. Each object was typically observed for 15-20 minutes with additional ~ 10 min for set-up and acquisition. The candidates are typically faint (V -magnitude: 20-21.5, see Table. 5.1) and we rely on the detection of strong emission lines, for the success of these observations. For wavelength calibration and flat fielding we requested day time spectral flats and arc lamp images. The same set-up was used for all the targets and the position angle of the slit was chosen such that a bright star always falls in the slit. Fig. 5.3 shows one example of typical data which we use in this work. The bright star (see Fig. 5.3) is represented by the broad horizontal white line and the target object i.e. candidate RLQ appears as a faint horizontal white line. The sky lines are the vertical white (bent) lines in Fig. 5.3. We drew a red vertical line to show the bending of the sky lines (see Fig. 5.3). The spectral coverage has two gaps, this is due to physical gaps between three CCD chips that read out the dispersed spectra (see Fig. 5.3).

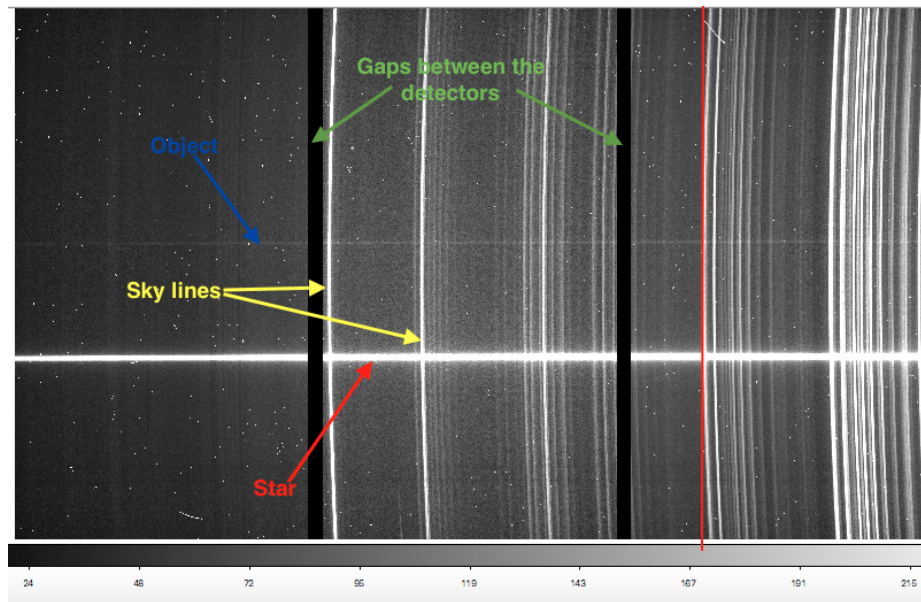


Figure 5.3: The 2D spectrum taken with SALT. The horizontal axis is the dispersion direction with wavelength getting redder towards the right. The coloured bar at the bottom is the intensity scale of the image. The three CCD chips comprising the RSS detector can also be seen, with gaps between them. The red vertical line show the bending of the sky lines.

Table 5.1: Spectroscopic observations summary for Galaxies-possible quasar discussed in this work. The SALT RSS-pg0900 grating with pc03850 order-blocking filter was used for all observations. Slitlets in all masks were 8' long and 2'' wide.

Target	RA (J2000)	Dec. (J2000)	Moon phase [%]	CRTS V-mag	Date
J040015-142328	04h00m15.04s	-14d23'28.2''	58.5	19.20 - 19.70	2014-11-30
J093919-173135	09h39m19.19s	-17d31'35.6''	75.8	19.00 - 19.60	2015-02-09
J095231-245351	09h52m31.67s	-24d53'51.0''	78.4	19.00 - 19.40	2015-03-30
J101313-254654	10h13m13.09s	-25d46'54.7''	61.3	20.70 - 21.70	2014-11-30
J111820-305458	11h18m20.61s	-30d54'58.5''	76.5	17.80 - 18.00	2015-02-28
J115222-270126	11h52m22.02s	-27d01'26.1''	1.3	19.90 - 20.60	2015-03-19
J115450-281251	11h54m50.43s	-28d12'51.0''	90.8	20.20 - 21.00	2015-03-02
J121128-351002	12h11m28.44s	-35d10'2.5''	20.9	20.90 - 21.90	2015-03-16
J123409-332638	12h34m9.97s	-33d26'38.7''	17.4	20.50 - 21.30	2015-02-22
			20.8	20.50 - 21.30	2015-03-16
J124553-161645	12h45m53.74s	-16d16'45.7''	1.2	20.20 - 21.00	2015-03-19
J125215-310351	12h52m15.17s	-31d03'51.2''	45.5	19.80 - 20.50	2015-04-25
J125443-383357	12h54m43.00s	-38d33'57.3''	41.4	20.00 - 20.70	2015-03-14
J130508-285041	13h05m8.44s	-28d50'41.8''	2.0	20.00 - 20.70	2015-03-21
J131736-134532	13h17m36.56s	-13d45'32.6''	41.2	19.80 - 20.50	2015-03-14
J141327-342235	14h13m27.16s	-34d22'35.6''	76.3	19.10 - 19.60	2015-04-09
J143708-294718	14h37m8.95s	-29d47'18.7''	80.0	19.30 - 19.90	2015-03-30

5.3 Spectroscopic Data Reduction

In this section we describe the methods of reducing the data provided from the SALT pipeline (the “product” data) into wavelength calibrated spectra. The data are based on observations (long-slit) obtained between November, 2014 and April, 2015.

In these observations the arc lamp was used only for the arc frames needed for wavelength calibration. The objects under investigation are the quasar candidates (see Table. 5.1), which are at unknown redshifts. The purpose of this pilot project was to confirm QSO nature of the objects and measure their redshifts.

The data reduction was carried out using the pipeline which reduces SALT RSS data, provide by **Dr Matt Hilton**. The data were in the Flexible Image Transport System (FITS) format. All spectroscopic data reduction are carried out by the pipeline, which include wavelength calibration and sky subtraction (flux calibration was not performed). The pipeline removes the cosmic rays at the extraction step, therefore the 1D spectra is cosmic ray free. A summary of the data reduction for long-slit spectroscopy is given below.

1. **Bias-subtraction:** The subtraction of the bias level is the first step in the data reduction. This bias level is introduced onto the CCD chip for ensuring that the chip is working in a linear regime. Such offsets are subtracted from all the images, by using a bias image, taken without exposing the chip.
2. **Flat-fielding:** This is a technique used to correct for the bias of the pixel sensitivity due to the intrinsic performance of the CCDs and the optics. To correct for anomalies in the optical path i.e. such as specs of dust on the optical surfaces, flat field frames are used. This correction can be done by dividing the science image by the normalised flat-field frame. In our SALT observations, the flat field image was obtained through observing uniform light (see Fig. 5.3).
3. **Distortion correction:** The sky lines have a definite curvature (distortions) along the spatial axis (see Fig. 5.3). This is due to the different path lengths the light takes through the optics along the slit. Generally, it is impossible to guide incident light into an instrument without aberration. Effects such as aberration or distortion in the images are mostly significant and recognizable. The raw spectra seen in the image invariably show a series of bent spectral features i.e. SALT data also have such artefacts.
4. **Wavelength calibration:** In this step, we associate the pixel coordinates in the CCD with the absolute wavelength by comparison with emission data whose absolute wavelengths are generally known. The Neon arc lamp was used for this purpose.

5.4 Quasar Redshift Measurements

We used a similar idea as Kurtz & Mink (1998), to measure the redshift of quasars by “cross-correlating the spectra with the Sloan Digital Sky Survey (SDSS) galaxy spectral and QSO templates using the RVSAO/XCSAO package for image reduction and analysis facility (IRAF)”. RVSAO is a set of programs used to obtain redshifts from digital spectra. It operates in the IRAF environment. However, the very important task of the system is XCSAO, which implements the cross-correlation method. We examined each spectrum individually, using an initial guess for the redshift based on visual inspection as an input for XCSAO. The 2D spectra is used as a sanity check to identify that the lines in the 1D spectra are real.

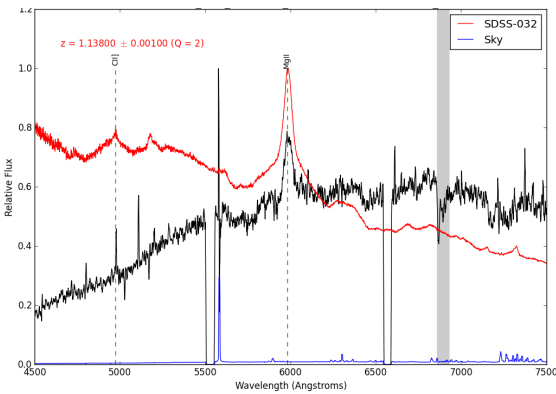
In order to test for the confidence level of each redshift measurement, we used a quality-rating system (Q) on visual inspection. $Q = 3$ rating, or $Q = 2$, were given to quasar candidates exhibiting multiple emission features or to quasars exhibiting two strongly detected emission features. Quasars showing two emission features, but exhibiting both faint and strong emission feature were given $Q = 1$; and quasars with tentative z values i.e. these were quasars showing only one faint emission line, were given $Q = 0$.

Through these steps we successfully measured redshifts of 12 out of 16 targets. Of these 12, 8 are at $z > 1.5$ i.e. 67 % efficiency of detection $z > 1.5$ quasars. The results are summarized in Table. 5.2 and the spectrum of each object is shown in Fig. 5.4, 5.7 etc. The SALT RSS spectra corresponds to the black lines in Fig. 5.4,

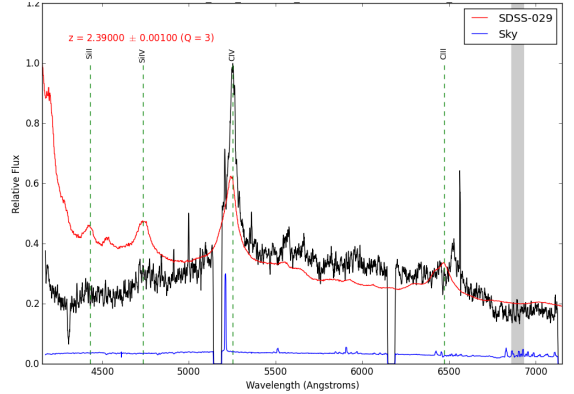
blue lines are the sky lines, and the red lines show the best match redshifted SDSS spectra in each case. The emission line(s) used to determine the redshifts are also identified.

Table 5.2: Spectroscopic redshifts of quasars measured using SALT RSS. Q is the redshift quality flag.

Target	Redshift	Q
J040015-142328	1.138	2
J093919-173135
J095231-245351	2.390	3
J101313-254654	2.969	3
J111820-305458	2.132	3
J115222-270126	2.698	3
J115450-281251	0.896	1
J121128-351002
J123409-332638
J124553-161645	1.045	0
J125215-310351	1.939	2
J125443-383357	2.777	3
J130508-285041
J131736-134532	1.267	2
J141327-342235	2.553	3
J143708-294718	2.111	3

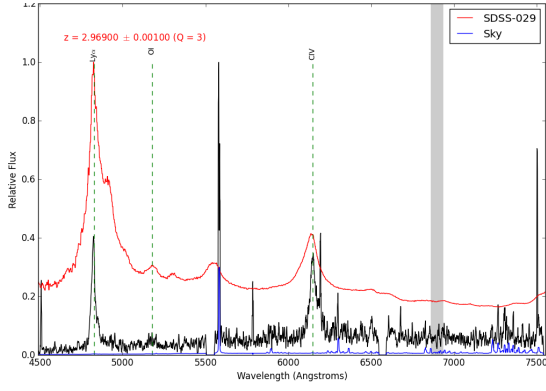


(a)

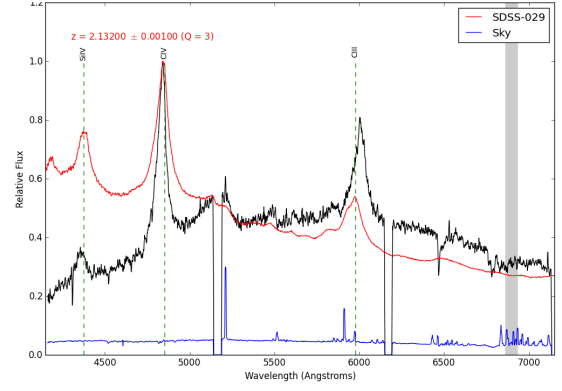


(b)

Figure 5.4: (a) The $z_{em} = 1.138$ quasar J040015-142328, showing C II and Mg II emission lines. (b) The $z_{em} = 2.390$ quasar J095231-245351, showing Si II, Si IV, C IV and C III emission lines.

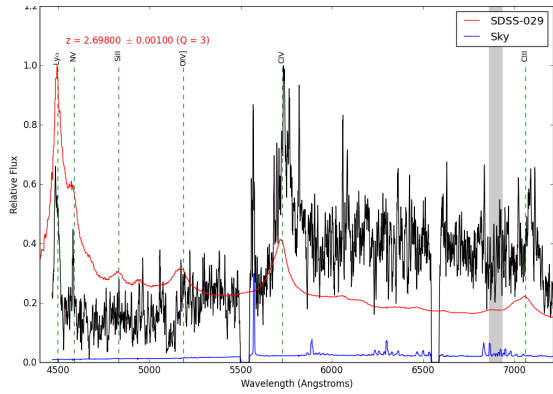


(a)

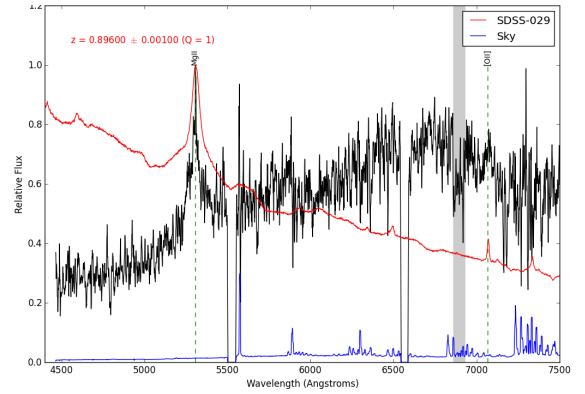


(b)

Figure 5.5: (a) The $z_{em} = 2.969$ quasar J101313-254654, showing Lyman- α , O I and C IV broad emission lines. (b) The $z_{em} = 2.132$ quasar J111820-305458, showing Si IV, C IV and C III emission lines.

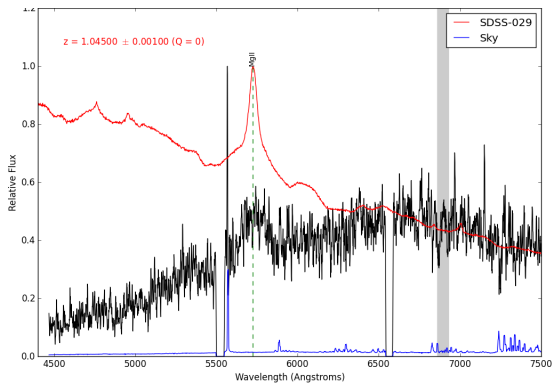


(a)

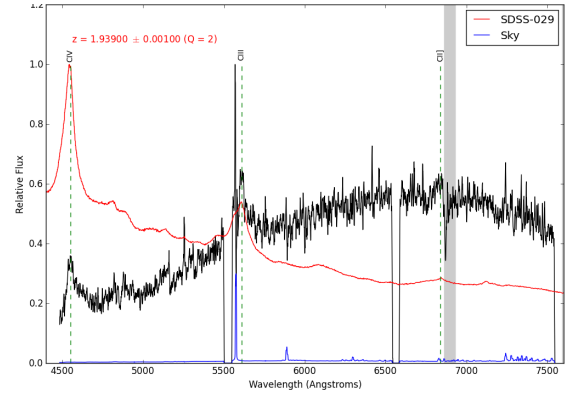


(b)

Figure 5.6: (a) The $z_{em} = 2.698$ quasar J115222-270126, showing Lyman- α , N V, Si II, O IV, C IV and C III emission lines. (b) The $z_{em} = 0.896$ quasar J115450-281251, showing Mg II and O II emission lines.

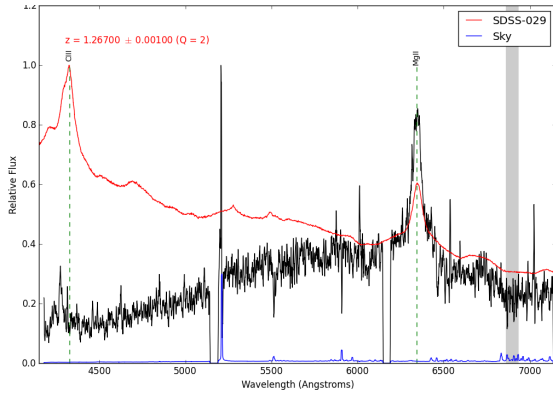


(a)

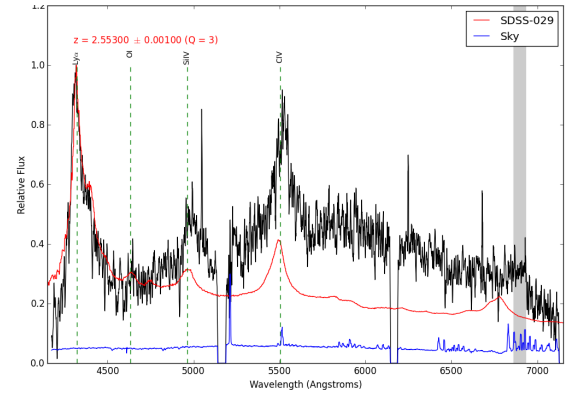


(b)

Figure 5.7: (a) The $z_{em} = 1.045$ quasar J124553-161645, showing Mg II emission line. (b) The $z_{em} = 1.939$ quasar J125215-310351, showing C IV, C II and C III emission lines.

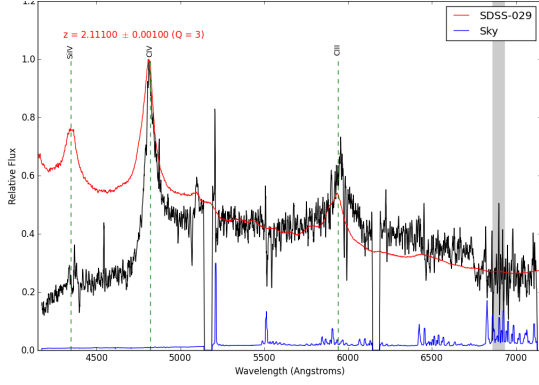


(a)

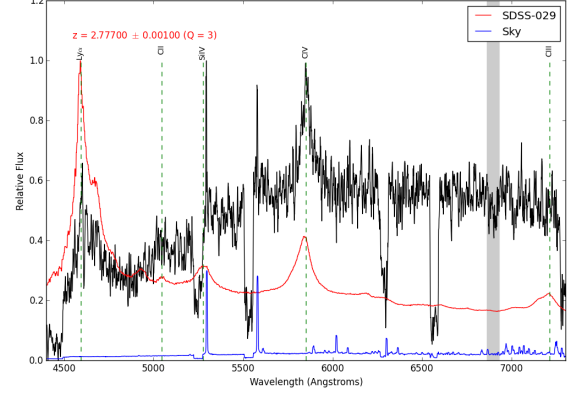


(b)

Figure 5.8: (a) The $z_{em} = 1.267$ quasar J131736-134532, showing a broad C III and Mg II emission lines. (b) The $z_{em} = 2.553$ quasar J141327-342235, showing Lyman- α , O I, Si IV and C IV emission lines.



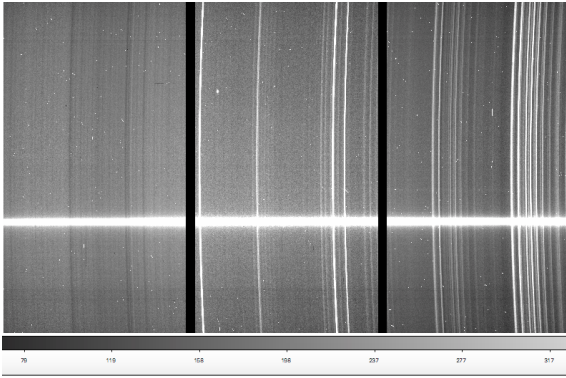
(a)



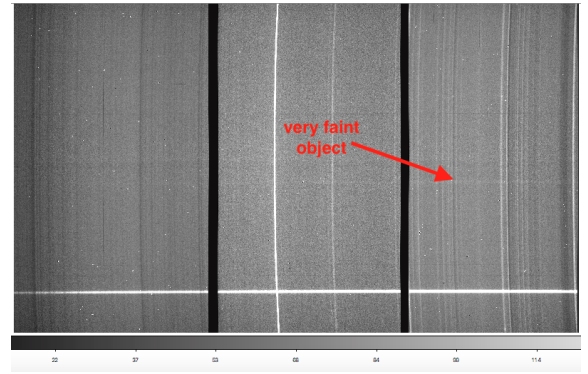
(b)

Figure 5.9: (a) The $z_{em} = 2.111$ quasar J143708-294718, showing Si IV, C IV and C III emission lines. (b) The $z_{em} = 2.777$ quasar J125443-383357, showing Lyman- α , C II, Si IV, C IV and C III emission lines.

We were not able to measure redshifts for all 16 candidates observed. In 2 cases, namely J123409-3326383 and J121128-351002, the data were unusable as the observing conditions did not meet the Principal Investigator (PI) constraints and the telescope had technical problems (e.g. issues such as telescope/instrument problems, incorrect observational set-ups, standard stars with low counts). In the fourth i.e. case of J093919-173135, the spectrum of the target source is overwhelmed by the nearby bright star leading to non-detection. For J130508-285041, the quasar trace was not detectable so the redshift cannot be measured. In Fig. 5.10, we show two long-slit 2D spectra: the one on the left, shows the case of J093919-173135. On the right panel, we show a typical example of successful observations.



(a)



(b)

Figure 5.10: (a) On the left panel, the target object is undetectable due to bright nearby star. The sky emission and the reference star have completely overwhelm the spectrum of the object of interest. (b) On the right panel, we show an example of long-slit 2D spectra of a faint QSO. Here, we notice that there is a faint horizontal white line corresponding to the target source (see text for details).

Despite all this, it is apparent that our target selection strategy is generally successful. We plan on continuing in the field and in the upcoming SALT semesters, we will observe a much larger sample of candidate

RLQs to gather targets for MALS and address various issues related to AGNs.

Future Prospects

The existence of red (i.e. dust-obscured) quasars are predicted in both the orientation-based AGN unification models and the evolutionary scenarios where the obscured phase represents a transitional phase between the merger-induced starburst stage and the unobscured UV-bright quasar stage. In addition, the reddening can also be caused by dusty gas associated with an intervening galaxy. While the existence of red quasars is not contested, the fraction of such quasars missing from the existing optically selected samples is highly uncertain, with estimates ranging from 10% to 50%.

Systematic searches of red quasars are necessary to (i) quantify the time spent by quasars in the obscured phase, (ii) establish link between the galaxy evolution and black hole growth, (iii) distinguish between various models of quasar outflows, (iv) estimate the quasar contribution to UV to gamma-ray backgrounds and, finally, (v) uncover the population of dusty ($A_V > 1$) intervening absorbers missed in optical surveys. This last point is crucial to unravel the evolution of cold atomic and molecular gas in galaxies and its links with the global star-formation activity.

The pilot SALT program to identify IR selected quasars presented in this thesis, paves the way for carrying out an ambitious program using SALT and various other optical telescopes to build the first, large, purely infrared-selected sample of radio-loud quasars (RLQs) at $z > 1.5$, that is well-suited for both: (i) studying the above mentioned AGN related issues at the main epoch of galaxy formation and AGN evolution, and (ii) follow-up in radio, which is also unaffected by the dust extinction, to search for intervening H I 21-cm and OH absorption lines using MeerKAT radio telescope (i.e. the MeerKAT Absorption Line Survey (MALS)) to constrain the evolution of cold ISM in galaxies at $z < 1.5$. Personally, the experience gained through the CASA based data reduction of datasets from GMRT and VLA will be valuable for developing pipeline for MeerKAT data analysis and carrying out early science with MeerKAT, and eventually make substantial contributions to MALS, and building a comprehensive picture of ISM.

Bibliography

- Allman, B., Klein, A., Nugent, K., Opat, G., 1993, 'Lloyd's mirage: a variant of lloyd's mirror', *European journal of physics*, 14 (6), 272.
- Argyle, B., Argyle, R., 2012. The resolution of a telescope. In: *Observing and Measuring Visual Double Stars*. Springer, pp. 105–115.
- Avison, A., George, S. J., 2012, 'A graphical tool for demonstrating the techniques of radio interferometry', *European Journal of Physics*, 34 (1), 7.
- Braun, R., Walterbos, R. A., 1992, 'Physical properties of neutral gas in m31 and the galaxy', *The Astrophysical Journal*, 386, 120–138.
- Carilli, C., Blain, A., 2002, 'Centimeter searches for molecular line emission from high-redshift galaxies', *The Astrophysical Journal*, 569 (2), 605.
- Combes, F., Pineau des Forêts, G., 1999, 'H₂ in space', In: *H₂ in Space*, Vol. 1.
- Condon, J., Cotton, W., Greisen, E., Yin, Q., Perley, R., Taylor, G., Broderick, J., 1998, 'The nrao vla sky survey', *The Astronomical Journal*, 115 (5), 1693.
- Crutcher, R., 1979, 'Nonthermal oh main lines and the abundance of oh in interstellar dust clouds', *The Astrophysical Journal*, 234, 881–890.
- Curran, S., Webb, J., 2006, 'The detectability of hi 21-cm absorption in damped lyman- α systems', *Monthly Notices of the Royal Astronomical Society*, 371 (1), 356–362.
- Darling, J., 2004, 'A laboratory for constraining cosmic evolution of the fine-structure constant: conjugate 18 centimeter oh lines toward pks 1413+ 135 at $z=0.24671$ ', *The Astrophysical Journal*, 612 (1), 58.

- Darling, J., Giovanelli, R., 2002, 'A search for oh megamasers at $z > 0.1$. iii. the complete survey', *The Astrophysical Journal*, 124 (1), 100.
- Djorgovski, S., Drake, A., Mahabal, A., Graham, M., Donalek, C., Williams, R., Beshore, E., Larson, S., Prieto, J., Catelan, M., et al., 2011, 'The catalina real-time transient survey (crtts)', *arXiv preprint arXiv:1102.5004*.
- Draine, B. T., 2010, 'Physics of the interstellar and intergalactic medium', *Princeton University Press*.
- Drake, A., Gaensicke, B. T., Djorgovski, S., Wils, P., Mahabal, A., Graham, M., Yang, T.-C., Williams, R., Catelan, M., Prieto, J., et al., 2014, 'Cataclysmic variables from the catalina real-time transient survey', *Monthly Notices of the Royal Astronomical Society*, 441 (2), 1186–1200.
- Field, G. B., 1958, 'Excitation of the hydrogen 21-cm line', *Proceedings of the IRE*, 46 (1), 240–250.
- Griffiths, D. J., 1995. Introduction to quantum mechanics.
- Gupta, N., Salter, C., Saikia, D., Ghosh, T., Jeyakumar, S., 2006, 'Probing radio source environments via hi and oh absorption', *Monthly Notices of the Royal Astronomical Society*, 373 (3), 972–992.
- Gupta, N., Srianand, R., Bowen, D., York, D., Wadadekar, Y., 2010, 'Gmrt mini-survey to search for 21-cm absorption in quasar–galaxy pairs at $z = 0.1$ ', *Monthly Notices of the Royal Astronomical Society*, 408 (2), 849–864.
- Gupta, N., Srianand, R., Noterdaeme, P., Petitjean, P., Muzahid, S., 2013, '21-cm absorption from galaxies at $z \sim 0.3$ '.
URL <http://arxiv.org/abs/1308.4141>
- Gupta, N., Srianand, R., Petitjean, P., Bergeron, J., Noterdaeme, P., Muzahid, S., 2012, 'Search for cold gas in strong mg ii absorbers at $0.5 < z < 1.5$: nature and evolution of 21-cm absorbers', *Astronomy & Astrophysics*, 544, A21.
- Ianjamasimanana, R., 2014. Interstellar medium properties and star formation in nearby galaxies. Ph.D. thesis, University of Cape Town.
- Jones, M. H., Lambourne, R. J., Adams, D. J., 2004, 'An introduction to galaxies and cosmology', *Cambridge University Press*.
- Kanekar, N., Chengalur, J. N., Ghosh, T., 2004, 'Conjugate 18 cm oh satellite lines at a cosmological distance', *Physical review letters*, 93 (5), 051302.
- Kulkarni, S. R., Heiles, C., 1988. Neutral hydrogen and the diffuse interstellar medium. In: Galactic and extragalactic radio astronomy. Springer, pp. 95–153.

- Kurtz, M. J., Mink, D. J., 1998, 'Rvsao 2.0: Digital redshifts and radial velocities', *Publications of the Astronomical Society of the Pacific*, 110 (750), 934–977.
- Leung, C.-M., Liszt, H., 1976, 'Radiation transport and non-lte analysis of interstellar molecular lines. i-carbon monoxide', *The Astrophysical Journal*, 208, 732–746.
- Liszt, H., 2001, 'The spin temperature of warm interstellar hi', *Astronomy & Astrophysics*, 371 (2), 698–707.
- Liszt, H., Lucas, R., 1999, '86 and 140 ghz radiocontinuum maps of the cassiopeia a snr', *Astronomy and Astrophysics*, 347, 258–265.
- McCready, L., Pawsey, J., Payne-Scott, R., 1947, 'Solar radiation at radio frequencies and its relation to sunspots', In: *Proceedings of the Royal Society of London A: Mathematical, Physical and Engineering Sciences*, Vol. 190, The Royal Society, pp. 357–375.
- Omont, A., Petitjean, P., Guilleaume, S., McMahon, R. G., Solomon, P., Pecontal, E., 1996, 'Molecular gas and dust around a radio-quiet quasar at redshift 4.7', *Nature*, 382, 428–431.
- Osterbrock, D. E., Ferland, G. J., 2006, 'Astrophysics of gaseous nebulae and active galactic nuclei', *University science books*.
- Payne, H., Terzian, Y., Salpeter, E., 1982, 'Neutral hydrogen observations in the direction of extended background radio sources', *The Astrophysical Journal Supplement Series*, 48, 199–218.
- Pradhan, A. K., Nahar, S. N., 2011, 'Atomic astrophysics and spectroscopy', *Cambridge University Press*.
- Roy, N., Kanekar, N., Braun, R., Chengalur, J. N., 2013, 'The temperature of the diffuse hi in the milky way— i. high resolution hi-21 cm absorption studies', *Monthly Notices of the Royal Astronomical Society*, 436, 2352–2365.
- Rybicki, G. B., Lightman, A. P., 2008, 'Radiative processes in astrophysics', *John Wiley & Sons*.
- Sadler, E. M., Hunstead, R., 2002, 'The sydney university molonglo sky survey (sumss) and optical redshift surveys of the southern sky', In: *The Universe at Low Radio Frequencies*, Vol. 199, p. 11.
- Shu, F. H., 1991, 'Physics of Astrophysics, Vol. I'.
- Smith, M. P., Nordsieck, K. H., Burgh, E. B., Percival, J. W., Williams, T. B., O'Donohue, D., O'Connor, J., Schier, J. A., 2006, 'The prime focus imaging spectrograph for the southern african large telescope: structural and mechanical design and commissioning', In: *SPIE Astronomical Telescopes+ Instrumentation*, International Society for Optics and Photonics, pp. 62692A–62692A.
- Taylor, G. B., Carilli, C. L., Perley, R. A., 1999, 'Synthesis imaging in radio astronomy ii', In: *Synthesis Imaging in Radio Astronomy II*, Vol. 180.

- Thompson, A. R., Clark, B., Wade, C., Napier, P. J., 1980, ‘The very large array’, *The Astrophysical Journal Supplement Series*, 44, 151–167.
- Weinreb, S., Barrett, A., Meeks, M., Henry, J., 1963, ‘Radio observations of oh in the interstellar medium’, *Nature*, 200 (4909), 829–831.
- White, R. L., Becker, R. H., Helfand, D. J., Gregg, M. D., 1997, ‘A catalog of 1.4 ghz radio sources from the first survey’, *The Astrophysical Journal*, 475 (2), 479.
- Wright, E. L., Eisenhardt, P. R., Mainzer, A. K., Ressler, M. E., Cutri, R. M., Jarrett, T., Kirkpatrick, J. D., Padgett, D., McMillan, R. S., Skrutskie, M., et al., 2010, ‘The wide-field infrared survey explorer (wise): mission description and initial on-orbit performance’, *The Astronomical Journal*, 140 (6), 1868.
- Zwaan, M., Liske, J., Péroux, C., Murphy, M., Bouché, N., Curran, S., Biggs, A., 2015, ‘New h i 21-cm absorbers at low and intermediate redshifts’, *Monthly Notices of the Royal Astronomical Society*, 453 (2), 1268–1280.